

December 2015

Investigation of Electrolyte Wetting in Lithium Ion Batteries: Effects of Electrode Pore Structures and Solution

Yangping Sheng

University of Wisconsin-Milwaukee

Follow this and additional works at: <https://dc.uwm.edu/etd>



Part of the [Materials Science and Engineering Commons](#), and the [Oil, Gas, and Energy Commons](#)

Recommended Citation

Sheng, Yangping, "Investigation of Electrolyte Wetting in Lithium Ion Batteries: Effects of Electrode Pore Structures and Solution" (2015). *Theses and Dissertations*. 1080.
<https://dc.uwm.edu/etd/1080>

This Dissertation is brought to you for free and open access by UWM Digital Commons. It has been accepted for inclusion in Theses and Dissertations by an authorized administrator of UWM Digital Commons. For more information, please contact open-access@uwm.edu.

INVESTIGATION OF ELECTROLYTE WETTING IN LITHIUM ION
BATTERIES: EFFECTS OF ELECTRODE PORE STRUCTURES AND
SOLUTION

by

Yangping Sheng

A Dissertation Submitted in

Partial Fulfillment of the

Requirements for the Degree of

Doctor of Philosophy

in Engineering

at

The University of Wisconsin-Milwaukee

December 2015

ABSTRACT

INVESTIGATION OF ELECTROLYTE WETTING IN LITHIUM ION BATTERIES: EFFECTS OF ELECTRODE PORE STRUCTURES AND SOLUTION

by

Yangping Sheng

The University of Wisconsin-Milwaukee, 2015
Under the Supervision of Professor Benjamin C. Church

Beside natural source energy carriers such as petroleum, coal and natural gas, the lithium ion battery is a promising man-made energy carrier for the future. This is a similar process evolved from horse-powered era to engine driven age. There are still a lot of challenges ahead like low energy density, low rate performance, aging problems, high cost and safety etc.

In lithium ion batteries, investigation about manufacturing process is as important as the development of material. The manufacturing of lithium ion battery, including production process (slurry making, coating, drying etc.), and post-production (slitting, calendering etc.) is also complicated and critical to the overall performance of the battery. It includes matching the capacity of anode and cathode materials, trial-and-error investigation of thickness, porosity, active material and additive loading, detailed microscopic models to understand, optimize, and design these systems by changing one or a few parameters at a time. In the manufacturing, one of the most important principles is to ensure good wetting properties between porous solid electrodes and liquid electrolyte. Besides the material surface properties, it is the process of electrolyte transporting to fill the pores in the electrode after injection is less noticed in

academic, where only 2-3 drops of electrolyte are needed for lab coin cell level. In industry, the importance of electrolyte transport is well known and it is considered as part of electrolyte wetting (or initial wetting in some situations). In consideration of practical usage term, electrolyte wetting is adopted to use in this dissertation for electrolyte transporting process, although the surface chemistry about wetting is not covered.

An in-depth investigation about electrolyte wetting is still missing, although it has significant effects in manufacturing. The electrolyte wetting is determined by properties of electrolyte and electrode microstructure. Currently, only viscosity and surface tension of electrolyte is used to reflect performance of electrolyte wetting. There are very few reports about quantitative measurement about electrolyte wetting. Moreover, there are only simple qualitative observations, good, poor, and fair, were reported on the wettability of microporous separators. Therefore, development of a quantitative analysis method is critical to help understand the mechanism of how electrolyte wetting is affected by material properties and manufacturing processes.

In this dissertation, a quantitative test method is developed to analyze the electrolyte wetting performance. Wetting rate, measured by wetting balance method, is used to quantitatively measure the speed of electrolyte wetting. The feasibility of the wetting rate is demonstrated by repeated test of wetting rate between electrolytes and electrodes. Various electrolytes from single solvents to complicated industrial level electrolytes are measured with baseline electrodes. Electrodes with different composition, active materials and manufacturing process, separator sheets with different materials and additives are also measured with baseline electrolyte. The wetting behaviors for different materials and manufacturing processes could be used to help improve the optimization of production process.

It is very necessary to reveal the mechanism underlying electrolyte wetting, especially the effects of electrode pore microstructure. The Electrodes, which are composed of active material, binder and carbon black, are formed by production process (rheological processing, coating, drying), and post-production process (calendering and slicing etc.). The pore structure is also complicated by the broad size range of pores from nanometer to tens micrometer. In this dissertation, a pore network concept, as revealed in the MIP test (mercury intrusion porosimetry), is employed to characterize the electrode pore structure. It is composed by the random pore cavity and connected part of pores, which are further described by the percentage of total pore volume and the threshold and critical pore diameter.

The effect of calendering process on electrolyte wetting, as a demonstration for typical post-production process, has been revealed by the wetting balance analysis. A quantitative analysis of the pore structure under the pore network concept is used to investigate the evolution of pore structure with the increase of calendering force. Based on the pore structure, the hypothesis of combined effects of capillary and converging-diverging flow in electrolyte wetting is proposed to understand the mechanism. A further demonstration of the effect of production process by adding excessive carbon black is accomplished. The hypothesis is valid to explain the electrolyte wetting behavior with increasing amount of carbon black. The pore structure differences between electrodes with various amount of carbon black are shown by the scanning electron microscope.

© Copyright by Yangping Sheng, 2015
All Rights Reserved

TABLE OF CONTENTS

List of Figures	ix
List of Tables	xii
Acknowledgements.....	xiii
CHAPTER 1 Introduction.....	1
1.1 Energy density and energy efficiency	3
1.2 Operation of Lithium ion battery	11
1.3 Electrode microstructure.....	19
1.4 Lithium ion battery manufacturing.....	25
1.5 Systemic manufacturing of lithium ion battery.....	30
1.6 Wettability.....	31
References.....	36
CHAPTER 2 Electrolyte wetting in anode and cathode	41
2.1 Introduction	41
2.2 Materials and Methods	43
2.3 Results and Discussion	45
2.4 Conclusion	55
References.....	57
CHAPTER 3 Effects of Calendering on wettability	59
3.1 Introduction	59
3.2 Materials and Methods	61

3.3	Results and Discussion	63
3.4	Conclusion	79
	References	80
CHAPTER 4 Electrolyte wetting of anode electrode with pore structures changed by binder/carbon black ratio		83
4.1	Introduction	83
4.2	Materials and methods.....	86
4.3	Results and discussion.....	87
4.4	Evolution of pore microstructure in the electrodes.....	94
4.5	Conclusion	101
	References	103
CHAPTER 5 Effect of electrolyte solution on the electrolyte wetting		106
5.1	Introduction	106
5.2	Experiment.....	108
5.3	Measurement of surface tension	108
5.4	Results and discussion.....	110
5.5	Effect of EA additive on the wetting rate	114
5.6	Conclusion	118
	References.....	119
CHAPTER 6 Summary.....		121
6.1	Establish electrolyte wetting test for anode and cathode electrode films.....	122
6.2	Electrolyte wetting of graphite anode with pore structure modified by calendering	123

6.3	Electrolyte wetting of anode electrode with different pore structures controlled by changing binder/carbon black ratio	124
6.4	Effect of electrolyte solutions on the electrolyte wetting.....	125
6.5	Novelty of the research.....	126
6.6	Future works.....	127
	Curriculum Vitae.....	130

LIST OF FIGURES

Figure 1-1 Comprehensive power density and energy density comparison of the most important energy carriers.....	4
Figure 1-2 Energy density develop for portable rechargeable batteries and trends.....	6
Figure 1-3 US DOE energy storage R&D roadmap for 2015 and beyond.	8
Figure 1-4 The typical energy flow of conventional internal combustion engine vehicle.	9
Figure 1-5 Energy efficiency analysis for Electric Vehicles from different pathways	10
Figure 1-6 Comparative well to wheel efficiency analysis for CNGV and EV.	11
Figure 1-7 Lithium ion battery operation	12
Figure 1-8 Electrode potential diagram for lithium ion battery. a) ideal battery, b) the conventional graphite/LiCoO ₂ battery, c) LTO/LFP battery.	13
Figure 1-9 Change of the qualitative energy diagram of Li _x CoO ₂ as a function of the Li content. From left to right, x=1, x=0.5, x=0.....	14
Figure 1-10 The Faradaic reaction $O + ne^- \rightarrow R$, in concentrate solutions.	16
Figure 1-11 A series of Li-ion battery discharge curves for a electrode with increasing discharge current.	19
Figure 1-12 (a) Sketch of electrode cross-section showing the diffusion length, L' , and electrode thickness, L . (b) The coordinate system of the electrode $\{v_1, v_2, v_3\}$ and of a particle $\{v_1', v_2', v_3'\}$	21
Figure 1-13 Porous electrode theory with three different scale levels. $c(x,t)$ is the bulk concentration, $\phi(x,t)$ is the electrostatic potential, $q(x,t)$ is mean charge density, $w(x,t)$ is the excess salt concentration per area, λ_D is the Debye screening length, h_p is the pore diameter.	23
Figure 1-14 relationship between battery voltage and electrode potential	27
Figure 1-15 A configuration of a typical lithium ion battery pack (Image courtesy of A123 Systems)	28
Figure 1-16 A summary of battery manufacturing process	29
Figure 1-17 A typical split charging formation process	33
Figure 1-18 Schematic Definition about wetting.....	35
Figure 2-1 Schematic diagram for wetting balance test set-up.	43
Figure 2-2 a) a typical m-t curve from wetting balance test, b) analysis about electrolyte transport process part of m-t curve by transferring time to root time, and dividing mass by sample cross section area and solution density. The resulting slope from linear curve fitting is the transport rate, K	47

Figure 2-3 Transport rates for anode and cathode samples. Hollow circles are the wetting rate of electrolyte in anode; solid triangles are the transport rate of cathode. Dashed lines are the average wetting rate for each foil type.	49
Figure 2-4 Cumulative intrusion curves for anode and cathode electrodes.	50
Figure 2-5 Normalized cumulative intrusion curve for anode and cathode. Secondary vertical axial is the slope of the intrusion curve.	53
Figure 2-6 Cross-sectional backscattered electron (BSE) SEM images of electrodes. a), and c) for anode, b) and d) for cathode.	54
Figure 3-1 A typical mass vs time curve (m-t curve) from wetting balance test.	64
Figure 3-2 Wetting rate for electrode films calendaring under various pressure	65
Figure 3-3 Wetting rate, K , as a function of porosity and average pore radius according to the Lucas-Washburn equation (1b). Average pore radius (r) is based on the average pore diameter as measured by MIP.	67
Figure 3-4 Cross-sectional backscattered electron (BSE) SEM images of graphite anode electrodes films. a), b), c), d), e) are for 59 μ m, 55 μ m, 53 μ m, 49 μ m, 41 μ m, respectively. f) Porosity for each film as measured by MIP.	69
Figure 3-5 Slope of normalized cumulative intrusion curve for all graphite anode electrodes films.	71
Figure 3-6 Differential pore volume of normalized cumulative intrusion curve (from Figure 5) for all graphite anode electrodes films.	72
Figure 3-7 Pore diameter change with calendaring force (Primary axis), ratio of d_{cr}/d_{th} change with calendaring forces (secondary axis)	74
Figure 3-8 a), Pore size ratio of calendared films to pore size in 59 μ m baseline anode films, and film thickness change with calendaring force. b) Schematic showing the pore size and geometry change with calendaring force in graphite anode films.	76
Figure 3-9 Scheme for electrolyte transport process in the porous medium.	76
Figure 4-1 Trends of the wetting rate Vs $P*r^{0.5}$ for electrodes with different carbon black ratio.	89
Figure 4-2 Normalized intrusion and extrusion curve for electrodes with different carbon black ratio.	91
Figure 4-3 Differential pore volume of normalized intrusion curve (from Figure 4-2) for electrodes with different carbon black ratio (focusing Pore diameter in the range of 1-3 μ m).	92
Figure 4-4 Pore diameter change of pore sub-network with different amount of carbon black.	94
Figure 4-5 SEM pictures of different electrodes, a,b) 3%CB at 600X and 2000K, c,d) 5%CB, e,f) 7%CB with 500X and 1000X magnification.	96

Figure 4-6 Typical void feature in different electrode film. a, bare pore wall in 3%CB, b, microcrack between CB domain and graphite 5%CB, c, a second pore formed in the CB domain in 7%CB.	98
Figure 4-7 some other example of microcrack in 5%CB.	99
Figure 4-8 Evolution of second pore in the void in 7%CB electrode.	101
Figure 5-1 A typical curve for surface tension test	109
Figure 5-2 Wetting rate change with root surface tension divided by viscosity for different solutions.	113
Figure 5-3 wetting rate changes with increasing PC contents in ionic liquid electrolyte in LiFePO ₄ cathode, data from literature.....	113
Figure 5-4 Wetting rate for different EA addition and anode and cathode	116
Figure 5-5 Surface tension and viscosity change with different amount of Ethyl Acetate.....	116
Figure 5-6 Wetting rate change with root surface tension divided by viscosity for different EA addition	117

LIST OF TABLES

Table 1-1 Estimated Materials Content of ideal lithium ion cells	26
Table 2-1 Summary for wetting balance test, wetting rate (K) are averaged data of 15 samples for each film type.	48
Table 2-2 summary for general MIP results.	50
Table 2-3 connecting pore diameters from normalized cumulative intrusion curves.	52
Table 3-1 Data summary of results from wetting balance test for all the electrode films	64
Table 3-2 Results summary for porosity and average pore diameter from mercury intrusion porosimetry (MIP)..	66
Table 3-3 Data summary of results from wetting balance test for all the electrode films	72
Table 4-1 Summary of compositions for each sample, and ratios between components (all compared in weight).....	87
Table 4-2 Data summary of results from wetting balance test and Pore data, porosity from MIP.....	88
Table 4-3 Data summary for pore sub-network for all the electrodes	92
Table 5-1 Summary of wetting rate, viscosity and surface tension data for all the solutions.....	110
Table 5-2 Summary of wetting rate, viscosity and surface tension data for different EA addition.	114

ACKNOWLEDGEMENTS

I would like to express my deepest gratitude to my advisor, Prof. Benjamin C. Church, for his excellent guidance, supporting, patience, and providing me with an excellent atmosphere for doing research. Under his outstanding support, I feel free and energetic to explore my research interests and finally accomplish the goal.

I am also grateful to my committee members, Prof. Nidal Abu-Zahra, Prof. Junhong Chen, Dr. Jianlin Li, Prof. Chang Soo Kim, for willing to participate and review the dissertation. The committee's suggestions bring the research to higher level. I also would like to thank Dr. Chris Fell and Dr. Yong Kyu Son at Johnson Controls, Inc. for help in the electrode film preparation and the manufacturing knowledge.

I also would like to thank Dr. H. A. Owen at the Biology Department at UW-Milwaukee for technical support with SEM analyses. In the same, I have to appreciate undergraduate assistant Bryce Erwin's delicate skills in preparing test samples, which is a grantee of test accuracy. Finally, I'd like to thank my friend and lab fellow, Shengyi Li, and Aruna Pushpa Kumara Wanninayake T M for sharing the wonderful time of PhD studying. It definitely improves this dissertation, by sharing and discussing complemented knowledge and understanding of science with them.

Thanks Department of Energy and Johnson Controls, Inc. for supporting this research, which is award number DE-EE0005500.

CHAPTER 1 Introduction

Beside natural source energy carriers such as petroleum, coal and natural gas, the lithium ion battery is a promising man-made energy carrier for the future. Beyond the notorious greenhouse issues with its natural counterparts, lithium ion batteries have benefits in that no direct CO₂ emissions are generated during operation. This modern energy storage method can be incorporated into many applications ranging from personal electronics, electrified vehicles, and renewable energy systems.

Since Sony commercialized lithium ion batteries in 1991, it has been the main energy carrier for portable consumer electronics. Compared with other chemical batteries, such as lead acid and nickel cadmium, the lithium ion battery has higher operation voltage and greater energy density which both make this technology more desirable from an energy storage and use perspective. However, the demands for batteries with higher energy densities are always present since it has direct impact on critical performance measures such as device operation time.

With the application of lithium ion battery extended to a larger scale, such as grid-tied energy storage and electric vehicles, this electrochemical energy carrier will have increasing beneficial impact on human society and the natural environment. Current debate over priority of the development of hybrid vehicles and pure electric vehicles is partly related to the net mileage capabilities of lithium ion batteries which is directly tied to energy density and power performance. However, hybrid vehicle and pure electric vehicles have different requirement for lithium ion battery. In order to support application of short charging/discharging cycle in hybrid vehicle, the

power density of lithium ion battery will be the first concern. To achieve longer mileage for electric vehicle, the energy density takes more consideration.

As indicated above, the lithium ion battery performance is a comprehensive concept that varies with different application purposes. Normally, the term performance will include energy density, power density, cycle life and/or calendar life, charging/discharging rate capability, safety, etc. Material choices and manufacturing processes of lithium ion battery are two major concerns which will determine the final performance of the cells. Each category is both complex in that they each contain many additional parameters but they are also complicated in that relations between various material and/or manufacturing topics are not well understood. The challenge lies in understanding this complex and complicated system with individual component interactions that combine to define the overall performance of the cell.

In this introduction, concepts and development of energy density of lithium ion batteries are discussed in the beginning. Next, operation of lithium ion battery is explored based on its fundamental electrochemical reaction. It includes energy diagram for single lithium cells, Li^+ ion transport inside electrolyte between anode and cathode, and charge transfer across the interface of electrolyte and active material. To further understand restrictions about lithium ion batteries, electrode microstructure, a porous media system, is discussed with its multiscale properties, tortuosity characterization and Bruggemann formula for conductivity and diffusivity. Then, electrode preparation is covered to show the challenges during battery manufacturing. Finally, the electrolyte wetting, or wettability, is introduced to discuss about more possibilities for improving battery performance and reducing producing cost within current material system.

1.1 Energy density and energy efficiency

1.1.1 Energy density

Energy density is the amount of energy stored per unit mass or volume, which can be referred to gravimetric or volumetric density, respectively. A comprehensive comparison of the most important energy carriers is given in Figure 1-1. For example, the energy density of gasoline, as representative for oil in general consideration in the figure, is about 12,200 Wh/kg or 9,700Wh/L. Energy density of a battery is the product of the cell's voltage and specific capacity. The specific capacity is the total Amp-hours available, Ah/g (or Ah/L), when the battery is discharged at a certain discharge current. It can be calculated by multiplying the specific discharge current (in Amps) by discharge time (in hours).

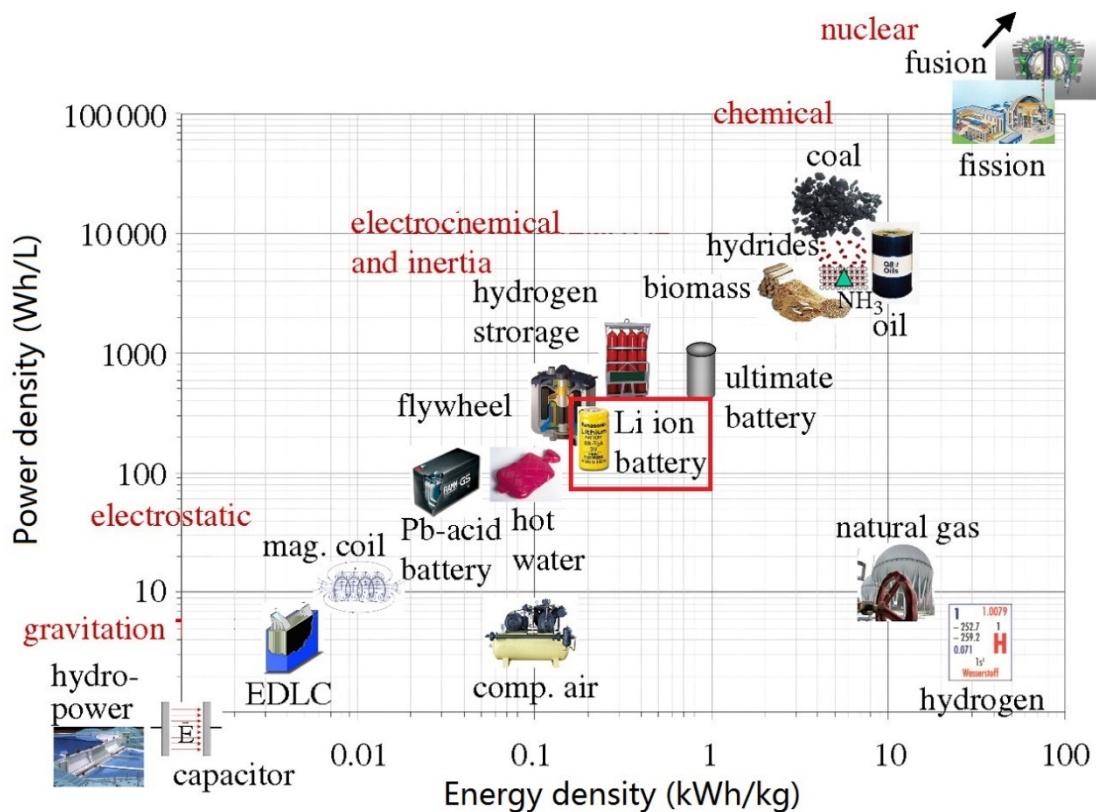


Figure 1-1 Comprehensive power density and energy density comparison of the most important energy carriers.[1]

The theoretical gravimetric energy density can be calculated by equation 1-1. It provides the theoretical limit for practical energy density. This theoretical calculation only considers the electrochemically active constituents in the battery. In an actual lithium ion battery, it is also composed of electrolyte, binder, conductive additives, separator, current collector, and packaging material (at the cell level) such that energy densities of manufactured cells are much lower than this theoretical maximum. According to equation 1-1[2], energy density can be improved by increasing the number of electrons in the redox reaction, battery operation voltage, and percentage of active material in the cell. Although only the latter two options are available for the lithium system, engineering optimization toward higher energy density is still a very attractive method.

$$ED_{grav} = \frac{nF(E_{pos}^0 - E_{neg}^0)}{EW_{reactants}} \quad (1-1)$$

where

ED_{grav} : theoretical gravimetric energy density

n : number of electrons involved in the reaction

F : Faraday's constant (96485 c/mole)

E_{pos}^0 : Voltage of positive electrode

E_{neg}^0 : Voltage of negative electrode

$EW_{reactants}$: Equivalent weight or molar mass of the active material

1.1.2 Development of energy density

Compared with other portable rechargeable batteries, lithium ion batteries have superior energy densities as shown in Figure 1-2. Since the widely accepted agreement about the importance of lithium ion battery, the pursuit of higher energy density has been a very hot subject since the technology was introduced and increases in this critical performance metric have resulted. However, there is still some disagreement about future targets for battery packs between industrial producers and academic researchers. JCESR (Joint Center for Energy Storage Research) from US Department of Energy set a goal of 400Wh/Kg by 2017. Industrial is considering 320Wh/kg is more feasible at that time. As the data shown in 2013 Tesla model S test review by Car and Driver[3], its battery pack has energy density of 141Wh/kg, according to data of 85KWh capacity and weight 600Kg (1323lb). Both target of JCESR and Industry is hard to achieve.

POWERING UP

Portable rechargeable batteries tend to hit an energy-storage-per-weight limit. Lithium-ion technology has gone through several phases and types, but is also expected to reach a ceiling soon.

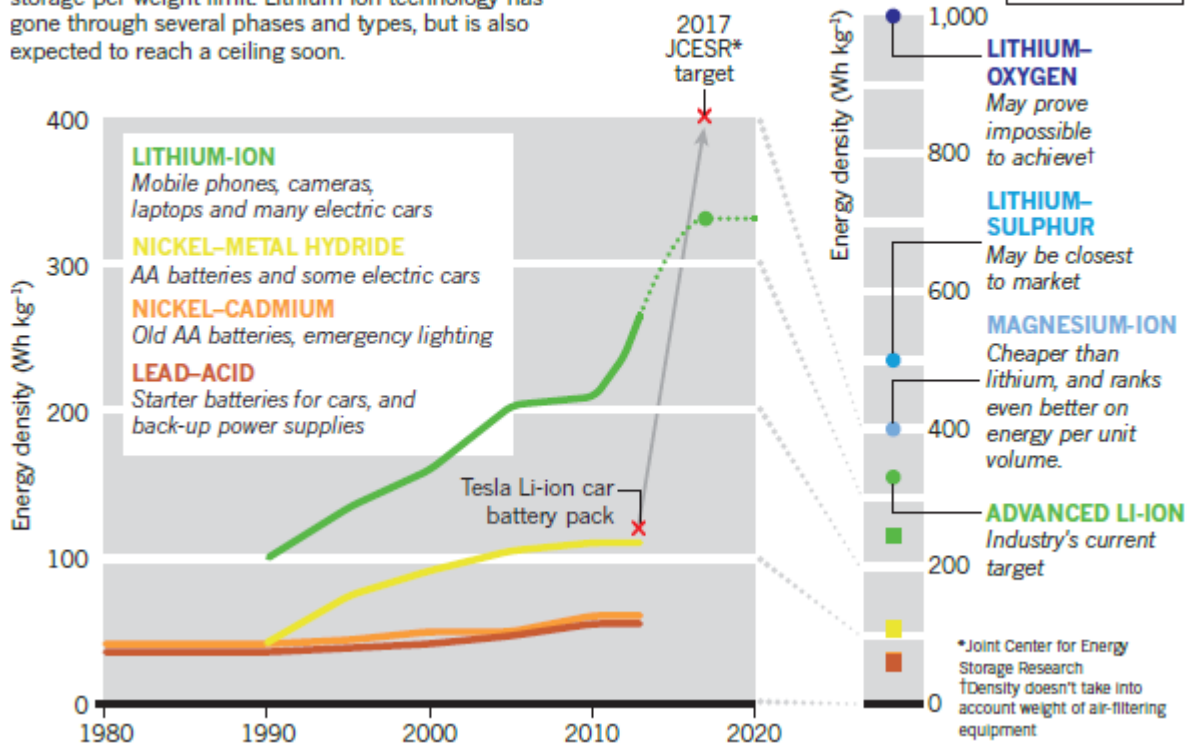


Figure 1-2 Energy density develop for portable rechargeable batteries and trends.[4]

Lithium ion battery pack, discussed in more detail in section 1.4, is composed certain amount of single cell batteries with ballpark figure varied from 200s to 7000s. The total weight of a pack is increased by package, welding, electrical controls, and coolant for battery temperature control. It is obvious that the development of the cell has significant impact to the battery pack. Compared with pouch cell available in the market, the 18650 cell, defined by its size of 18mm diameter and 65mm length, manufactured by Panasonic Inc. still has much better energy density currently. When size of single cell is increased from 18650 cell to pouch cell, the requirement for battery engineering becomes difficult.

Figure 1-3 shows a US DOE roadmap for energy storage goals that shows an increase in energy density and reduction in price per kWh capacity. In current technology, graphite and layered cathode system, the theoretical energy density is 400 Wh/kg or 1400Wh/L, however, the practical energy density is only 150Wh/kg or 250 Wh/L. In a real battery, the active material only takes 37.5% by weight, and 17.9% by volume of the entire pack. Compared with adopting novel battery materials with high voltage or high capacity, increasing weight or volume percentage of active materials is an important but easily overlooked ways to increase the net energy density of the cell. Without improvement of active material, increased energy density of a battery can also be achieved through engineering manners where high percentage of active material can be incorporated into the cell by improved cell design and manufacturing processes. However, research and publication about battery engineering is still rare compared with development of novel materials, and mostly shown in patents or simply held internally by battery manufactures.

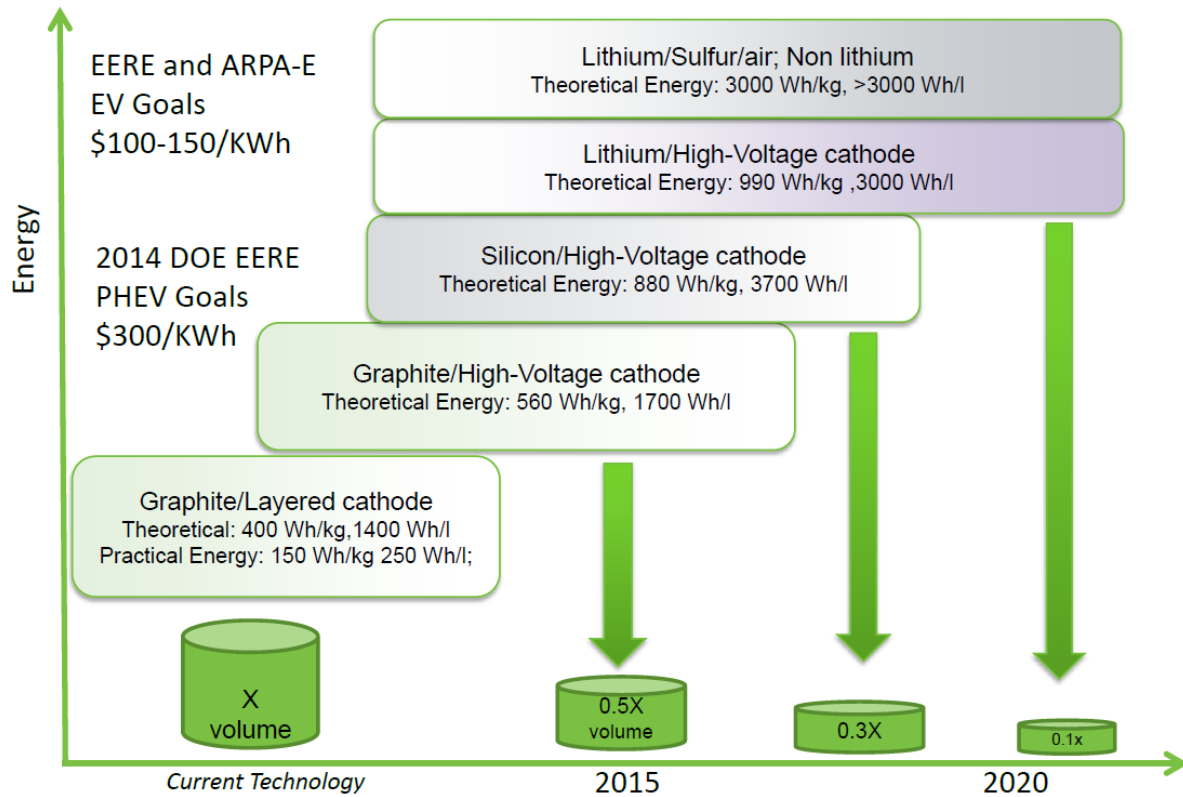


Figure 1-3 US DOE energy storage R&D roadmap for 2015 and beyond.[5]

1.1.3 Energy efficiency

According to definition given by Lawrence Berkeley National Lab, energy efficiency is using less energy to provide the same service[6]. Figure 1-4 shows the typical energy flow of a conventional Internal Combustion Engine (ICE) vehicle. Only 40% of the energy is used for vehicle operation, where only about 15% is used to move the vehicle and accessories operation, 10% is caused by air and rolling resistance, and 15% is lost by idling where engine has to keep running while car is stopped for a while. As a thermal energy is used by ICE to operation, most of energy are consumed by heating, as stated by Carnot cycle limitations[2]. However, electrical power used in electric vehicle is beyond the limitation, the electrochemical charge transfer reaction supported battery operation could have almost all the energy converted into electricity. Currently, more than 75% of

energy consumed by electric vehicle are used to run the car, with averaged 4-8 miles per kWh capacity[7].

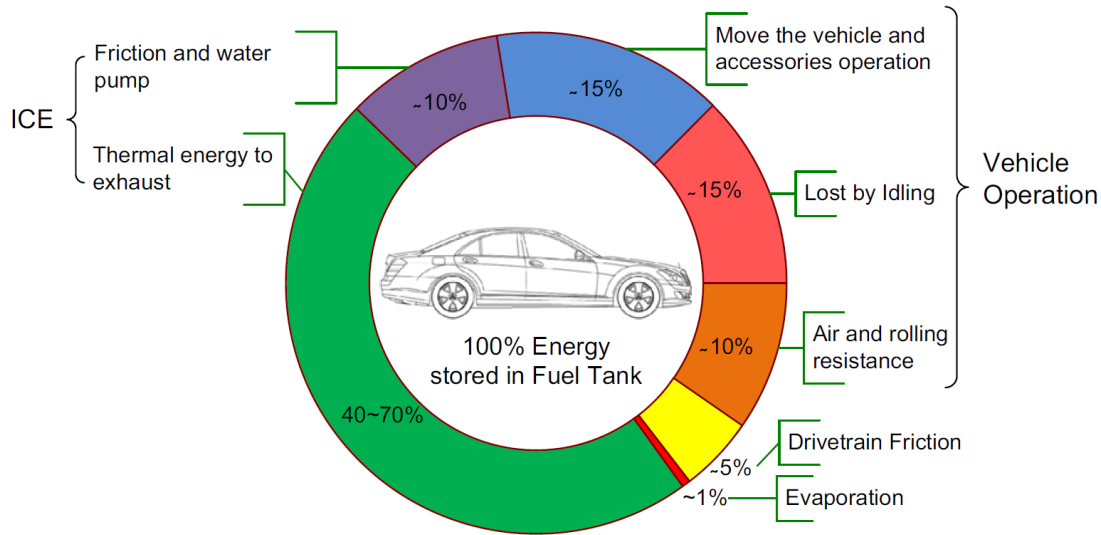


Figure 1-4 The typical energy flow of conventional internal combustion engine vehicle.[8]

The electricity can be generated in different sources: coal, natural gas, and renewables (as sun, wind or hydraulic energy etc.). To consider the effect of different electricity source on total energy efficiency for electric vehicle, well to wheels (WTW) analysis, a modified cradle-to-grave life cycle analysis, is performed[9]. The WTW analysis can be divided by upstream and downstream energy use and efficiency. The upstream accounts for energy production cost and efficiency, which is referred as well-to-tank (or pump) (WTT)[10]. The downstream is the tank-to-wheels (TTW) analysis which consider the energy use and efficiency for vehicle. A life cycle based energy efficiency analysis for electric vehicles are given in Figure 1-5 [11]. The pathway of generating electricity from renewable energy is the most efficient energy use which is above 60% in WTW efficiency. In traditional energy sources like coal and natural gas, the WTW efficiency is reduced more than half to 25%- 28%. However, it still holds advantage over the gasoline engine vehicle,

which is 14.1% of WTW efficiency. The energy efficiency for gasoline engine, about 25%, is comparatively low relative to coal-fired and gas turbine power station which is higher than 49%.

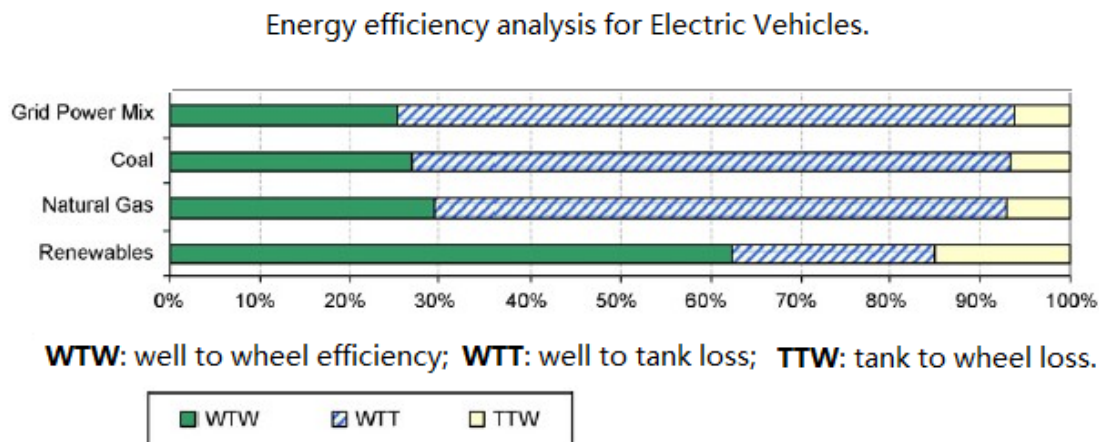


Figure 1-5 Energy efficiency analysis for Electric Vehicles from different pathways.[11]

Figure 1-6 is a comparative analysis of energy use from natural gas which is abundant and low cost, according to the research of Scott Curran et al[12]. In their study, the well to wheel efficiency for compressed natural gas vehicle (CNGV) is only 11%-12%, whereas, 22% to 35% could be achieved in EV mode where the natural gas is used to generate electricity. The battery based electric vehicle has a slight advantage in energy efficiency even compared with fuel cell powered vehicles.

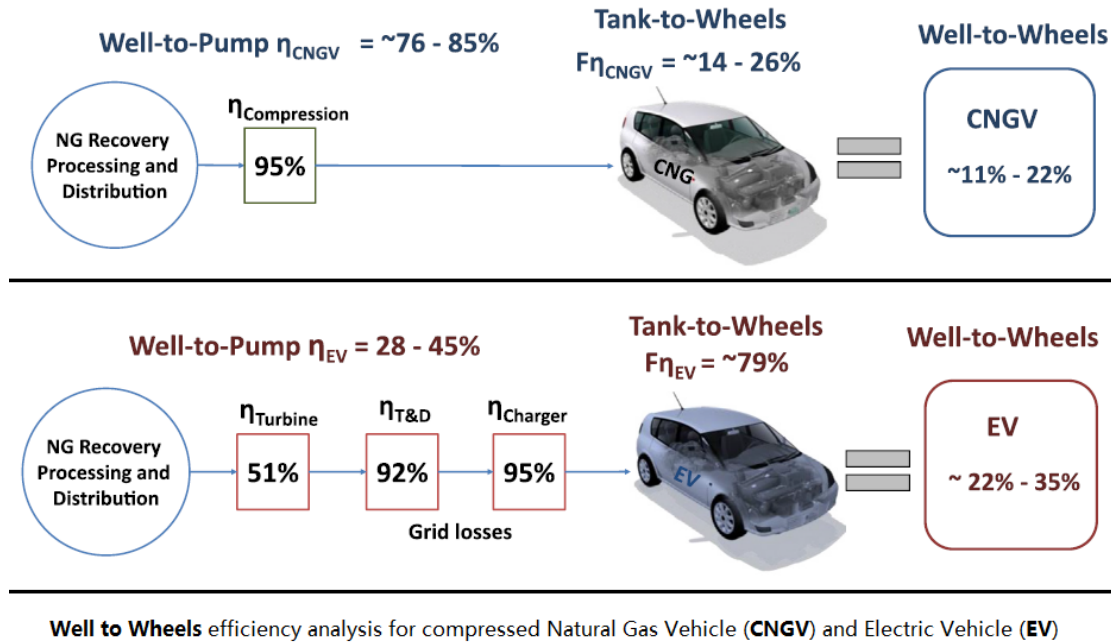


Figure 1-6 Comparative well to wheel efficiency analysis for CNGV and EV.[12]

1.2 Operation of Lithium ion battery

1.2.1 Basics of lithium ion batteries

The lithium ion battery, fundamentally, is based on redox electrochemical reaction. As indicated in Figure 1-7, lithium ion battery is a delicate designed to harness the redox reaction. It is composed by two paths of ion transport and electron conduction. During discharge, deintercalated lithium ions are released from the anode by oxidation reaction and are transported to the cathode through the electrolyte. Meanwhile, generated electrons are conducted to the current collector through an internal conductive network, then transported to the cathode by an external circuit. In the cathode, lithium ions are intercalated to the host material through a reduction reaction. It's a reverse process for charging process.

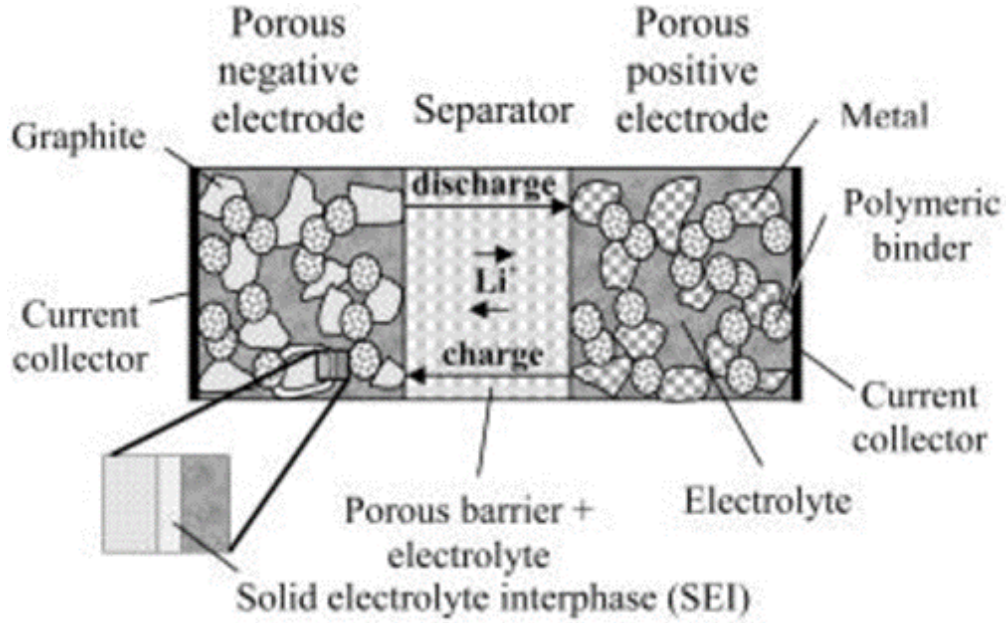


Figure 1-7 Lithium ion battery operation.[13]

1.2.2 Energy diagram for lithium cell

The open-circuit voltage of a cell is the difference between the electrochemical potential, μ_A and μ_C of the anode and cathode[14]:

$$V_{oc} = (\mu_A - \mu_C)/e \quad (1-2)$$

As shown in Figure 1-8, the middle yellow area donated potential range of electrolyte which is from LUMO (lowest unoccupied molecular orbitals) to HOMO (highest occupied molecular orbitals)[15]. It is donated as E_g which is also considered as allowed potential window of the electrolyte[16, 17]. An ideal situation should be μ_A below LUMO, and μ_C above HOMO (Figure 1-8a and 8c) to keep electrolyte stable. However, as shown in Figure 1-8b, μ_A is over LUMO, and μ_C is below HOMO in conventional graphite/LiCoO₂ battery. As a result, the electrolyte is reduced in the anode, and oxidized in the cathode, until the solid electrolyte interphase (SEI) layer is formed at each interface which block further reaction with the electrolyte[16].

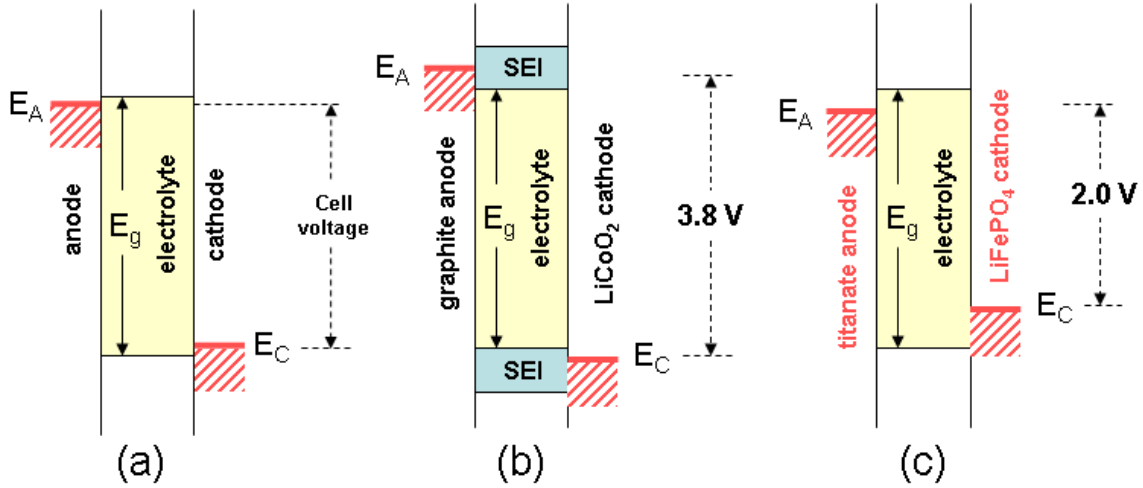


Figure 1-8 Electrode potential diagram for lithium ion battery. a) ideal battery, b) the conventional graphite/LiCoO₂ battery, c) LTO/LFP battery.[15]

For cathode material, the redox energy of transition metal should be on the top of anion-p bands to avoid oxidation of the anion[14]. The electrical conductivity of a specific cathode material can be obtained from its energy gap[18]. In Li_xCoO₂, for example, the energy of Co(IV)/Co(III) couple is near the top of O-2p bands when $x > 0.5$, as shown in Figure 1-9, $x = 1, 0.5$ [15]. The holes introduced into the Co(IV)/Co(III) couple by removal of Li⁺ are initially in Co (IV) states[19]. Further removal of Li⁺ will result in the overlap of Co(IV)/Co(III) 3d with O-2p orbit, as shown in Figure 1-9, $x = 0$, O²⁻ decompose into O₂ gas during charging with oxidation of cobalt and release of electrons from the 2p band, O₂²⁻ = O₂ + 2e⁻. [20] In practical situations, overcharge of Li_xCoO₂ beyond $x < 0.5$ should be avoided to prevent the generation of oxygen gas[21].

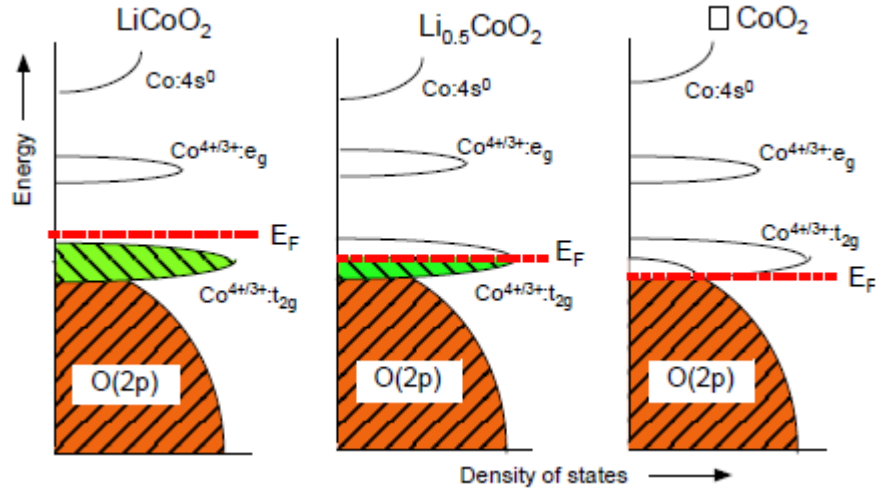


Figure 1-9 Change of the qualitative energy diagram of Li_xCoO_2 as a function of the Li content. From left to right, $x=1$, $x=0.5$, $x=0$. [15]

1.2.3 Butler-Volmer equation and salt concentration

The electrochemical charge transfer at electrode-electrolyte interface can be described by the exchange current across the surface as equation 1-3, which is also called Butler-Volmer equation [22].

$$I = I_0 \left(e^{-\alpha_c F \eta / (RT)} - e^{\alpha_a F \eta / (RT)} \right) \quad (1-3)$$

where I : current density, I_0 : exchange current density, α_a, α_c , apparent transfer coefficient for anodic and cathodic reaction, F : faradic constant, η : surface overpotential, R : universal gas constant, and T , temperature.

Overpotential is the potential difference between actual potential and the equilibrium potential. It is also used as a measurement for polarization, which is affected by charge transfer resistance in electrolyte, electrode characteristic and solution concentration.

Exchange current density is slightly varied with solution conditions. In concentrated solution condition, activity coefficient of ions in the solutions should also be considered. Equation 1-4 [23] and 1-5 [24, 25] are expressed to describe for dilute solution and concentrated solution, respectively. To further explain the reaction in the concentrated solution, a description of $O + ne^- \rightarrow R$ reaction with relative chemical potential is shown in Figure 1-10.

$$\text{Dilution solution condition: } I_o = nFk_a^\alpha k_c^{1-\alpha} C_R^\alpha C_O^{1-\alpha} \quad (1-4)$$

$$\text{Concentrated solution condition: } I_o = k_0 ne (\tilde{C}_O \tilde{C}_e^n)^{1-\alpha} \tilde{C}_R^\alpha \left[\frac{(\gamma_O \gamma_e^n)^{1-\alpha} \gamma_R^\alpha}{\gamma_\ddagger} \right] \quad (1-5)$$

k_a, k_c : rate constants for anodic and cathodic reactions

α : symmetry factor, $\alpha = \frac{X_\ddagger - X_R}{X_O - X_R}$, $\alpha_a = (1 - \alpha)n$, $\alpha_c = \alpha n$

γ_\ddagger : activity coefficient of the transition state

$\gamma_i = e^{(\mu_i^{ex} - \mu_i^0)/K_B T}$, μ_i^{ex} , excess chemical potential, μ_i^0 , chemical potential at standard status.

\tilde{C}_i : dimensionless concentration, $\tilde{C}_i = C_i / C_i^o$

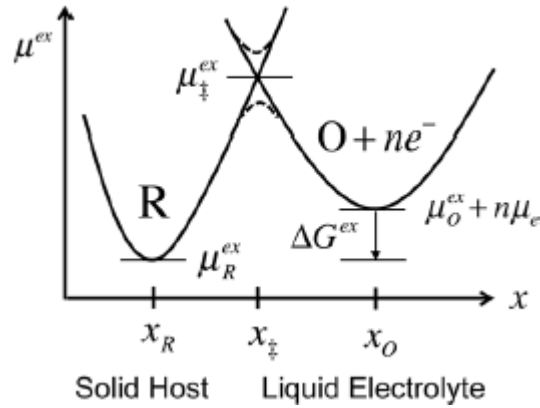


Figure 1-10 The Faradaic reaction $O + ne^- \rightarrow R$, in concentrate solutions.[24]

As shown in Butler-Volmer equation, current density is affected by exchange current density (I_o), surface overpotential (η), and temperature and nature of electrode surface (α_a, α_c). The exchange current density is affected by adjacent concentration in dilute solution condition, which is a widely used assumption currently. In concentrated solution condition, the exchange current density is also affected by activity coefficient, which can be considered as effective concentration [26]. Activity coefficient is also the ability to dissociate Li ions from solvent. It has been reported that, activity coefficient increase rapidly with concentration in moderate and high concentration situations [27]. Therefore, adjacent concentration only is not enough to understand electrode kinetics. It is very important to identify electrolyte is whether dilution or concentrated solution in the beginning of analysis.

The adjacent concentration is the concentration around active particles in the electrode. Considering the microstructure of the lithium ion battery, the electrode film is a porous structure composed of active material, binder and conductive additive and pores among solid particles. Active material, binder and conductive additives forms an electronic conductive network inside

the electrode film. An ionic conductive network is constituted by the pores which are eventually filled with an electrolyte. The adjacent concentration for active particles in lithium ion battery is the concentration of electrolyte in the surrounding pores. In previous researches, larger pores are associated with bigger particles [28], and lithium ion has tendency to accumulate around larger particles than smaller particles[29]. Therefore, the adjacent concentration is also affected by heterogeneous distribution of pores size and pore connectivity.

Electrolyte concentration in the electrode, therefore, is also not a constant and homogeneous value. Concentration gradients across the thickness of electrode film is common and determined by many other factors which come from both properties of electrolyte and electrode, and the battery operation condition[22, 26]. Salt diffusion coefficient, and ion transference number of electrolyte will build up the concentration gradient[27]. Porosity, particle size distribution, and position from current collector to separator sheet inside electrode film will also build up the concentration gradient. In addition, different charging/discharging rate will further vary the concentration gradient. According to research of Doyle and Fuentes[30], modeling concentration gradients for discharge currents at 2 C yields concentrations in excess of 2 M for the anode, starting with concentration at 1M. This can be further increased by higher current.

Another property of electrolyte is higher activity than the molarity of solutes should indicated. In LiPF₆/ PC/EC/DMC electrolyte system, the number of salt molecules per liter is only one fifth of that in water. Thus, a 1M electrolyte solution could be comparable to 5M aqueous solution[27]. In their research for this electrolyte system, the electrolyte was observed to behave as a concentrated solution even at 0.1M, which is a relative low concentration. Therefore, concentrated solution condition for electrolyte should be more applicable for most case where concentration around 1M is mostly used in practice.

1.2.4 Discharge curves

The discharge curve is one of the most significant characteristics for lithium ion battery. It may vary with different discharge conditions, for example, constant current, constant power and constant external resistance. Electrical properties that can be acquired from the discharge curve are battery voltage, current, and power with the variations of discharge time, capacity and lithium ion filling fraction (or occupancy). As shown in Figure 1-11, a series of discharge curves with increased discharging current[31]. The curves are shifting towards the left with lower lithium ion filling fraction when the current is increased. Faradaic (or surface, or activation) overpotential η_F dominates at early times and low filling fraction, while concentration overpotential η_C (due to diffusion limitation in either the solid or electrolyte phases) usually becomes rate limiting and dominates the polarization at later times and high filling, as indicated with green line in Figure 1-11. The concentration overpotential η_C , [32] which is also affected by particle size distribution, temperature and electrode/seperator porosity etc., has more impact on the battery capacity for fast charging/discharging application.

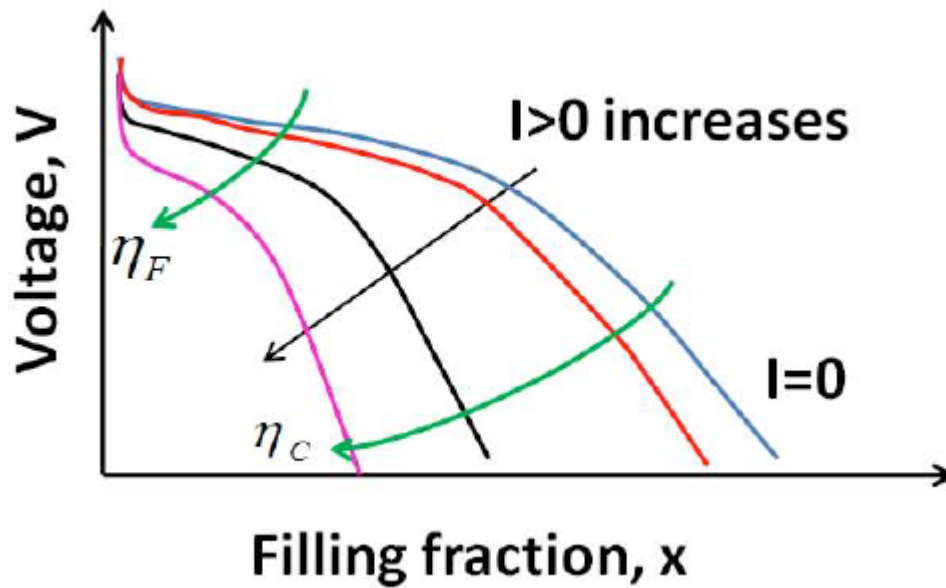


Figure 1-11 A series of Li-ion battery discharge curves for a electrode with increasing discharge current. [33]

1.3 Electrode microstructure

1.3.1 Double roles of electrode

Besides innovations of individual components, for example, active materials for anode and cathode, binder and conductive additives, optimization of electrode microstructure is the next step to improve lithium ion batteries. The electrode microstructure, can also be referred to as the electrode geometry; and is the complicated assembly of those individual components. It should be designed to optimize electronic and ionic conductivity. The network formed by the binder and conductive additive, mostly carbon black, is functioned as an electronic conductive path from the active material to the current collector. Pores among these solid particles are responsible for electrolyte storage; and form an ionic conductive path back-and-forth from anode to cathode and through the separator sheet which has the same functions of electrolyte storage and ionic path.

The double roles of electrode create a challenge for microstructure design. The electronic and ionic paths are competing either each other and varied with different applications, i.e. electrical vehicle and electrochemical storage have very different requirements. Due to the difficulties of *in-situ* measurement and 3D microstructure observation ability, understanding those two paths within local current density and ion concentration is still very challenge. For practical situations, effective value is mostly used to characterize these two properties, based on effective medium approximation. More detailed discussion about effective value is given in the following section.

1.3.2 Tortuosity and Bruggemann relation

Although understanding the real 3D microstructure of porous electrode in lithium ion battery is still challenging, tortuosity has been one of the most important parameters to characterize porous 3D microstructure. It measures the effective path length of ion and electrical transport inside porous electrode in most of macro-homogeneous model in battery operation simulation. Definition about tortuosity is also very simple, as reflected in equation 1-6 and Figure 1-12a.[34] It equals to square of the ratio of diffusion length to the real thickness.

$$\tau = \left(\frac{L'}{L}\right)^2 \quad (1-6)$$

where, τ is tortuosity, L' is the diffusion length across the electrode, and L is the electrode film thickness.

The effective diffusion coefficient can be estimated from diffusion coefficient in the electrolyte according to equation 1-7, in a relation with tortuosity and porosity. [35-38]

$$D_{eff} = \frac{\varepsilon}{\tau} D_0 \quad (1-7)$$

Where D_{eff} is effective diffusion, D_0 is the diffusion coefficient of lithium ion in the electrolyte, ε is the porosity of electrode.

In the past fifty years, empirical Bruggemann relation $\tau = \varepsilon^{-0.5}$ is used to estimate the tortuosity. The real vale about tortuosity is still very difficult to assess [34, 36]. In order to improve accuracy, equation 1-8 is a general expression for Bruggemann relation to estimated tortuosity from porosity[37].

$$\tau = \gamma \cdot \varepsilon^{-\alpha} \quad (1-8)$$

where, α is also called Bruggemann exponent, γ is the Bruggemann factor.

A quantitative analysis about tortuosity across the electrode film has been possible, with the advance of 3D observation technology, which mainly are X-ray tomographic microscopy,[39] [40, 41]and focused-ion beam scanning electron microscope (FIB/SEM) tomography[41]. These technologies enable researches to observe and quantify the 3D microstructure of the electrodes.

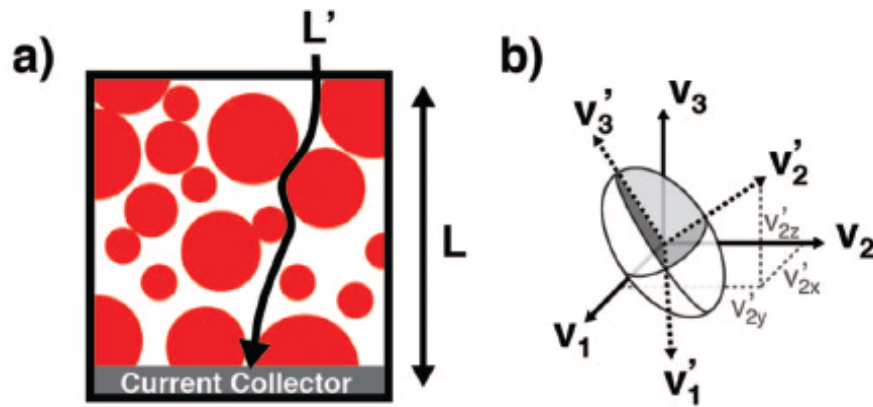


Figure 1-12 (a) Sketch of electrode cross-section showing the diffusion length, L' , and electrode thickness, L . (b) The coordinate system of the electrode $\{v_1, v_2, v_3\}$ and of a particle $\{v_1', v_2', v_3'\}$. [34]

1.3.3 Porous electrode theory

Beyond tortuosity, porous electrode theory has been used to investigate the relation of electrochemical process and electrode microstructure. Compared to the effective measurement of tortuosity, the real geometrical structure is considered in porous electrode theory. Slightly different with other geometrical investigations which deal with solid particles inside electrode, in porous electrode theory, pores among solid particles are served to describe electrolyte storage, ion transport, diffuse charge, and Faradaic reactions. A schematic representation of cathode is shown in Figure 1-13. The effect of SEI formation need to be considered in the anode situation.

According to various length scales, the porous electrode structure can be described by three levels of hierarchy, which clearly shown in Figure 1-13 with length scale decreasing from left to right. The first is the macroscopic continuum, which is characterized by some volume averaged variables, bulk concentration $c(x,t)$ and electrostatic potential $\varphi(x,t)$. As expressed, $c(x,t)$ and $\varphi(x,t)$ change with time and position. Under the macroscopic continuum is the macropores, reflected in the middle of Figure 1-13. In this scale, a lot of localized properties that are a function of pore size and pore shape, are taken into account. In-situ properties like mean charge density $q(x,t)$ and excess salt concentration $w(x,t)$ are reflected due to the change of local $c(x,t)$ and $\varphi(x,t)$. When the pore size further decreased to micropore scale, where $h_p^{mi} \ll \lambda_D$, double layer properties like nanoscale diffusion and charge distribution will be obvious. Although the porous electrode theory gives a general roadmap for exploring underlying electrochemical behavior, it still lacks practical guidance to improve overall battery performance.

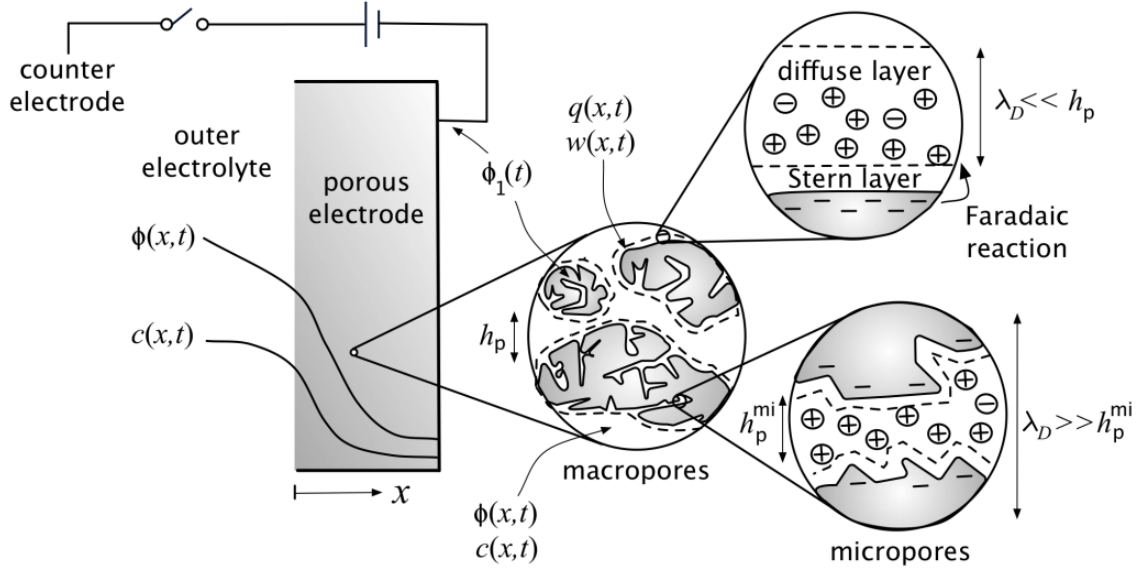


Figure 1-13 Porous electrode theory with three different scale levels. $c(x,t)$ is the bulk concentration, $\phi(x,t)$ is the electrostatic potential, $q(x,t)$ is mean charge density, $w(x,t)$ is the excess salt concentration per area, λ_D is the Debye screening length, h_p is the pore diameter.[42]

1.3.4 Multiscale concept

As stated in the porous electrode theory, the underlying electrochemical process in lithium ion battery can be divide into three length scale level. The multiscale feature for electrodes are obvious, in which the multi-porosities has size range from several nanometers to tens of micrometer. As in multiscale systems, the description of the dynamics (electrolyte flux, ion diffusion etc.) of such systems can be made at different scales. Therefore, how those dynamic processes correlated in the different scales is becoming important and necessary. Manufacturing processes have major effects on the larger macroscale properties, material properties have more effects at micro-and nano-scale.

The multiscale concept is more instructive to manufacturing where the macroscale porosity can be easily optimized. As the electrolyte is injecting into the battery assembly, lithium ions go from

macropores into micropores and nanopores with the progressing of electrolyte solution. According to capillary behavior, the electrolyte transport will be also highly affected by pore size scales. Although flow path of electrolyte inside electrode is less studied, solution propagation behavior investigation has revealed that solution transport follows certain flow paths which has more tendency to form in the larger pores. Moreover, considering ion transport from big pores to smaller pores, there will be a transition from surface diffusion regime at larger pores (due to electrostatic screening) to bulk diffusion regime for small pores. In the position outside of Debye's layer in larger pores, the remaining solvent in the bulk fluid can be considered as locally electrically neutral, because of electrostatic screening. This would cause a minimum ion permeability for a certain small pore size.

According to this multiscale concept, the dynamic processes in the macropores can be independently treated, neglecting its interactions with processes in much smaller pores. The highly connected nature of macropores makes it easy to accommodate pore network theory. The effect of pore network on electrolyte transport inside electrode films has been investigated and will be discussed in the following chapters. With proper engineering of macropores, the improvement of wetting rate could be remarkable. By introducing a set of micro-channels with a width of 40-55 μm (NMC cathode), 70 μm (LMO cathode) using a laser-based technique, W. Pfeging and J. Pröll also observed a dramatic acceleration of electrode wetting[43]. The capillary rise height in micro-channel engineered electrodes is 5 times higher in first 10 second by their measurement. With the improvement in macropores, the pouch cell shows an increase in capacity retention and cell life-time at high charging/discharging rate.

1.4 Lithium ion battery manufacturing

1.4.1 Material components for lithium ion battery

Besides the complicated porous structure, it is also of interest to consider material components for a single lithium ion battery, or lithium ion cell for more precise in the contexts of battery pack related topic. Based on data given by L. Gaines and R. Cuenza [44], Table 1-1 gives estimated material content for two ideal lithium ion battery, high energy cell and high power cell. For high energy cell, the electrode film is thicker than that of power cell in order to increase the energy density. It needs less separator sheet (1.8% for energy cell, 5% for power cell) but more electrolyte (18% for energy cell, 13.5% for power cell). The rest of cell takes 31.5% of total weight in the power cell, but it's only 10.4% in the energy cell.

Graphite, the anode active material, has theoretical energy density of 372 Ah/kg. LiCoO_2 , the cathode active material, has theoretical energy density of 275 Ah/kg. Therefore, in order to balance the capacities of anode and cathode, the cathode film is usually thicker and takes more weight percentage. As shown in table 1-1, the cathode active material weights 41.0% compared with 16.4% of active anode material in high energy cell, and 22.9% compared with 4.3% of that in high power cells. The imbalanced feature inside lithium ion cells caused the challenges in mass transport and kinetics across the electrodes. Balance the capacity is also critical to battery safety and prevent overcharging.

Table 1-1 Estimated Materials Content of ideal lithium ion cells. [45]

Material/Component	High-Energy (100Ah) Cell EV		High-Power (10 Ah) Cell HEV	
	Quantity (g)	Part (%)	Quantity (g)	Part (%)
Anode (dry)				
Active material (graphite)	563.6	16.4	14.1	4.3
Binder	69.7	2.0	3.1	1.0
Current collector (Cu)	151.9	4.4	41.6	12.8
Cathode (dry)				
Active material (LiCoO ₂)	1408.6	41.0	74.4	22.9
Carbon	46.4	1.4	3.2	1.0
Binder	92.9	2.7	6.3	1.9
Current collector (Al)	63	1.8	19.4	6.0
Electrolyte	618	18.0	44	13.5
Separator	60.5	1.8	16.4	5.0
Rest of Cell				
Tabs, end plates, terminal semblies	66.2	1.9	32.2	9.9
Core	0.9	0.0		
Container	291	8.5	70.1	21.6
Total	3432.7		324.8	

1.4.2 Battery design

Because of the different capacities of anode and cathode along with various performance requirements of different applications, battery design is important to fully utilize the active materials. Battery design is applying material components to achieve desired battery performance, and normally follows these basic principles[46]:

- 1) Balancing the electric capacity of anode and cathode during charging and discharging.
- 2) Battery voltage depends on its state of charge.

- 3) The electric capacity of battery is determined by designed voltage range, in which the battery cannot be charged over the maximum cutoff voltage or discharged below the minimum cutoff voltage.

The relation of battery voltage and electrode potential illustrated in Figure 1-14. The battery voltage is determined by the difference in potential between the cathode and the anode. It is calculated from the minimum cutoff voltage and the maximum cutoff voltage. Changing the ratio of the cathode and anode could lead to a different cutoff voltage. Therefore, there is a need to pay attention to the charge balance. It will affect the capacity, voltage and safety characteristics. The left part indicates relative capacity alignment of anode and cathode, where the black part represents the initial irreversible capacity. Commercialized graphite anodes have an irreversible capacity value of 20-30Ah/kg. LiCoO_2 cathodes have a value of 3-5Ah/kg.

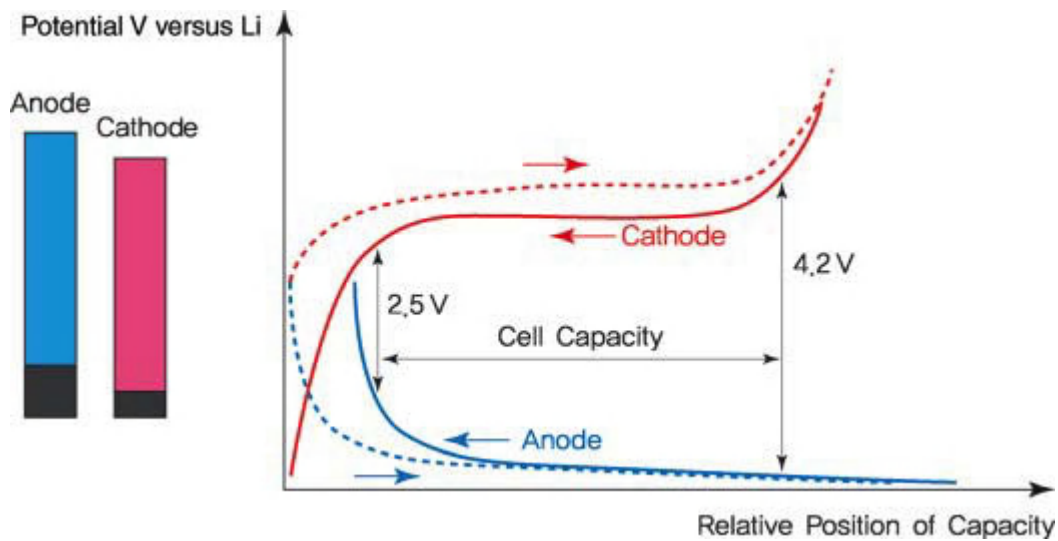


Figure 1-14 Relationship between battery voltage and electrode potential. [46]

1.4.3 Summary of battery pack manufacturing

Compared with single cells, the battery pack is not only a simple assembly of single cells. As indicated in Figure 1-15, a battery pack is composed of a lot of components to fulfill the functions of temperature control, overcharge protection, and battery manage. The battery pack manufacturing, as summarized in Figure 1-16, can be divided into three stages: a); electrode processing; b); single cell assembly; and c); battery module and pack integration. A detailed description of the whole processes can be found in reference, [46 - 49].

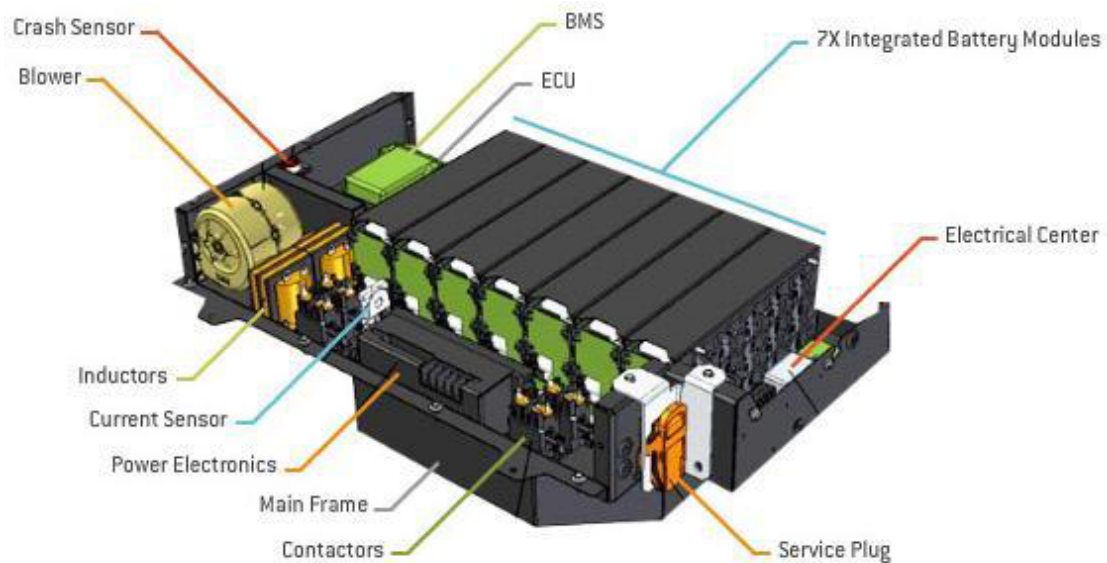


Figure 1-15 A configuration of a typical lithium ion battery pack (Image courtesy of A123 Systems). [50]

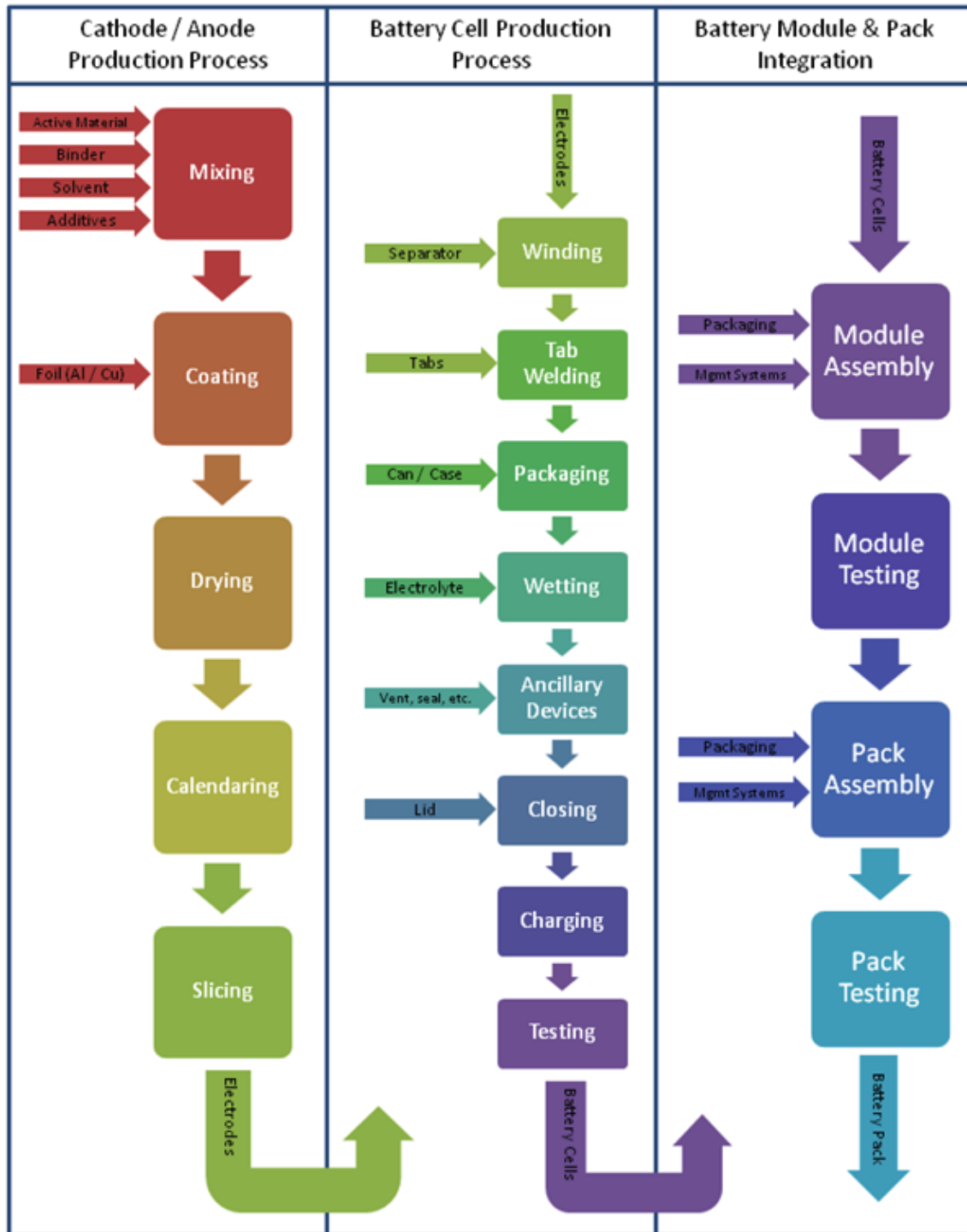


Figure 1-16 A summary of battery manufacturing process.[50]

1.5 Systemic manufacturing of lithium ion battery

The performance of a lithium ion battery pack is highly dependent on the quality of the individual cells. However, the improvement of a single cell will not necessarily result in enhancement of performance of a pack. To understand the connection between single cell and battery pack, lithium ion battery should be taken into account in three levels [51]: market level (issues related to the consumer, cost, safety, and life etc.), system level (problems related to researchers and industries, underutilization, capacity fade, thermal runaways etc.), and single cell sandwich level (understanding fundamental mechanisms related to lithium ion battery operation). Many of the problems in the other level can be solved by solving single cell sandwich level problems

In the single cell sandwich level, interactions between active materials, electrolyte, separator and inactive materials also have great influences on the electrochemical performance. Therefore, research about lithium ion batteries have to follow a systemic approach. As a highly complex system, each step in the manufacturing process is equally important. It is important to find out interactions among components and their effects on the final performance.

Systemic manufacturing approach is to focus on understanding relations between each step, and arrange each other to achieve best performance and lowest manufacturing cost for lithium ion battery. Some steps in the manufacturing process are highly related to each other and completed in sequence. Starting from the slurry mixing procedure, where active material, polymer binders, conductive additives, and solvents are mixed to form a slurry. Then a porous electrode coating is prepared by coating and drying the slurry on a metal current collector foil. The coated electrode is calendered to provide accurate control of thickness and increase the density of the electrode mass.

Later, anode, separator and cathode films are wound together to the cell assembly. After electrolyte injecting, the assembly is turned into the lithium ion battery through wetting and formation process.

In this manufacturing line, the electrolyte wetting is a connecting link between assembly and charging formation process. The wettability of electrolyte in the porous electrode film is affected by each component in the cell assembly. The following formation process is also affected by the quality of wettability. Although the potential of electrolyte wetting in systemic manufacturing of lithium ion battery is obvious, researches about the wetting and its relation to other process are still rare. A detailed discussion about wettability and its relation with formation process is in the next section.

1.6 Wettability

1.6.1 Electrolyte injection process

After cell assembly, electrolyte is added to the cell through a hole in the cap by a precision pump and then vacuum filled to ensure that the electrolyte permeates and completely fills the porosity in the separator and electrode structures[48]. The quality of electrolyte filling in the pore structure of the electrodes and separator highly affect the next formation and storage aging process. Moreover, distribution of electrolyte inside the cells has further impact on final battery performance, such as capacity, rate, cycle life and safety etc. The amount and the distribution of electrolyte within the cell volume is important for the cell's overall performance. In fact, flooding or depletion of the cell electrolyte severely impairs cell performance and may cause failures.

1.6.2 Charging formation process

The lithium ion batteries are built in an uncharged state. When the active material in the electrode films is contact with electrolyte, an electrochemical reaction would have happened to store electrical energy, with applied charge. This process is known as charging formation process which also involved with creating an electronically passive film on the anode active material, the solid electrolyte interface (SEI) layer[52]. Due to non-uniform electrolyte wetting, incomplete reaction of particles and unstable SEI film on anode surface, a loss of capacity, deteriorated cycles and poor storage performance will happen[53]. Moreover, as nanoparticles are increasingly used for high power application, the electrolyte wetting in the nanoscale porous channel between nanoparticles is becoming more and more difficult. In practical, a period of ~12-24 hours under vacuum is required to achieve adequate wetting during the cumbersome electrolyte filling process of cell assembly, and it still leaves a substantial fraction of the smallest pore volume unwetted[54].

A split formation process, as illustrated in Figure 1-17, has more advantage to meet this challenge[55]. To ensure good electrolyte wetting, a wait period of about 24 hours is conducted after the initial electrolyte injection. Then, the cell is initially charged to low state of charge (SOC) range, at rate of $C/100$ - $C/2$. After the charge is applied, the cell is stored at predetermined temperature for about one day. During or after storage, a degassing procedure may be carried out to provide a uniform distance between the electrodes. After completing the storage period, the cell is charged to high or full SOC. The cell is stabilized for another predetermined period of time, about one to seven days at room temperature. The split charging formation process is necessary for achieving higher energy density and calendar and cycle life.

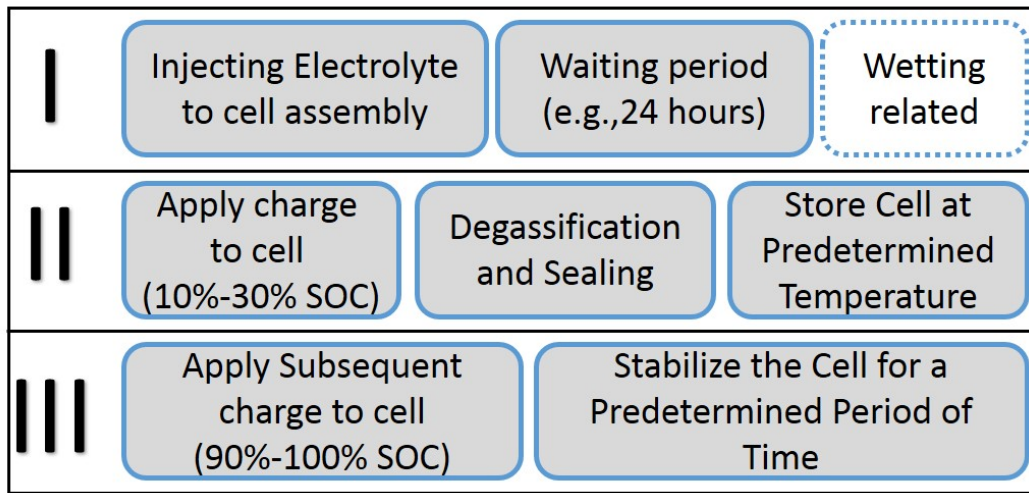


Figure 1-17 A typical split charging formation process. [55]

1.6.3 Definition about electrolyte wetting

In general, the performance of electrolyte wetting is usually considered to be determined by its surface tension and viscosity[56]. In order to improve battery performance, especially, functional designed for electrolyte composition is required, which will further affect its surface tension and viscosity[57]. Wetting agent is added when the electrolyte cannot sufficiently wet the non-polar polymer separator sheet[58]. Higher reversible capacity (354 mAh g^{-1} versus 347 mAh g^{-1}) and coulombic efficiency (91% versus 84%) in the first cycle is achieved by adding 2–5% cyclohexane wetting agent into the electrolyte system with 1M LiPF_6 and EC/DEC (1:2).[59] The improvement in performance is attributed to the improved wettability of electrolyte to the separator and electrodes.

The complexity of the electrolyte wetting is often ignored, although the importance of its effects on the battery performance is constantly reminded. After the electrolyte is injected, the wetting

process happened with the extension of solution front, until an equilibrium status is achieved. The capillary force is the underlying driving force. On the way of electrolyte filling all the pores, the porous electrodes/separator media are in unsaturated condition. This process is described as capillary flow[60], where the pressure deficit is directly connected with the surface tension and curvature existing on solution front (or the liquid-gas interfaces) within the electrodes medium[61]. Compared with saturation condition of flow in porous media which can be resolved with Darcy's law[62] or Navier-Stokes equation[63] in macroscopic, the unsaturated situation still has more microscopic complexity to deal with. The microscopic concerns of electrolyte wetting are more related to understanding the mechanism of battery operation and find out solutions for electrode optimization.

Considering the multiscale concept as discussed in electrode microstructure section, as represented in Figure 1-18, wetting can also be divided into different scales: drop spreading, one dimensional imbibition, and wicking in textures [59]. Wetting is the combined phenomenon of these three controls. The intersections between circles emphasize the connections between each controls. The shape of a boundary, the equilibrium contact angle, surface roughness are the interconnected parameters between controls, which will directly affect the wetting properties.

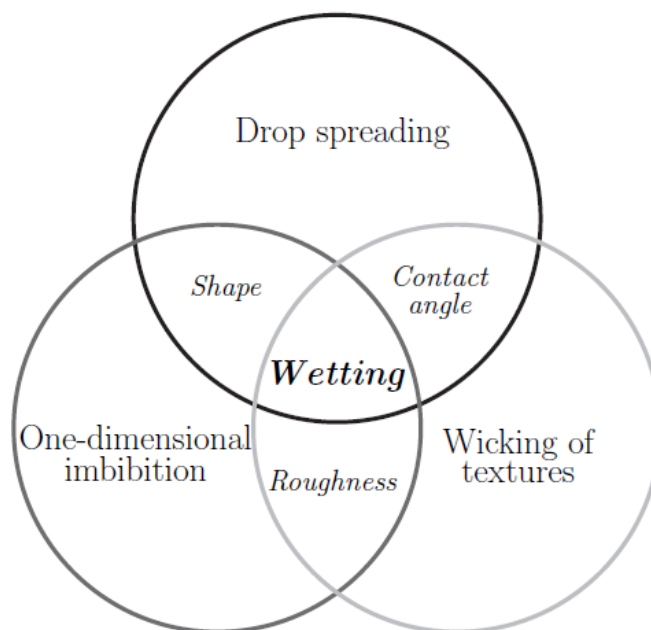


Figure 1-18 Schematic Definition about wetting.[64]

Wicking is the spontaneous absorption of liquid into a porous medium by the action of the capillary pressure. The driving capillary suction force that pulls a liquid into the porous medium arise as a result of wetting of its solid matrix by the invading liquid. The imbibition is the spreading of liquid in one dimension channels[65]. It is a ubiquitous natural phenomenon. It has been widely investigated in other applications like oil recovery, textile and paper treatment, detergency and filtration etc.[66-69]. However, the imbibition nature of electrolyte wetting is not understood. Compared with the complicated multiscale pore structure of electrode, solution nature of electrolyte is general consider as a single phase solution. The contact angle with active material is considered to be less than 30 degrees.

References

1. Zuttel, A., et al., (2010) Hydrogen: the future energy carrier. *Philos Trans A Math Phys Eng Sci.* 368(1923): p. 3329-42.
2. Spotnitz, R., *Lithium ion batteries, the basics*, in *CEP.* 2013, American Institute of Chemical Engineers (AIChE). p. 39-43.
3. Csere, C. *2013 Tesla Model S, Futurepreneur Elon Musk builds a good car, not just a good electric.* 2012 [cited 2015 04-29]; Available from: <http://www.caranddriver.com/reviews/2013-tesla-model-s-test-review>.
4. Noorden, R.V., (2014) The rechargeable revolution: A better battery. *Nature.* 507: p. 26-28.
5. *2011 Annual Merit Review and Peer evaluation meeting energy storage R&D*, in *Vehicle technologies program*, D. Howell, Editor. 2011, U.S. Department of energy, office of energy efficiency and renewable energy.
6. *What is energy efficiency?* [Office website] [cited 2015 03-18]; Available from: <http://eetd.lbl.gov/ee/ee-1.html>.
7. Research, M.I. *High Impedance Battery Research.* 2012; Available from: <http://www.meridian-int-res.com/Energy/Battery.htm>.
8. Tie, S.F. and C.W. Tan, (2013) A review of energy sources and energy management system in electric vehicles. *Renewable and Sustainable Energy Reviews.* 20: p. 82-102.
9. Commission, T.L.f.t.C.E., (February 2007) Full fuel cycle assessment, Well to Tank energy inputs, emissions and water impacts.
10. *Well-to-Tank Energy Use and Greenhouse Gas Emissions of Advanced Fuel/Vehicle Systems-North American Analysis.* June 2001.
11. Campanari, S., G. Manzolini, and F. Garcia de la Iglesia, (2009) Energy analysis of electric vehicles using batteries or fuel cells through well-to-wheel driving cycle simulations. *Journal of Power Sources.* 186(2): p. 464-477.
12. Curran, S.J., et al., (2014) Well-to-wheel analysis of direct and indirect use of natural gas in passenger vehicles. *Energy.* 75: p. 194-203.
13. Christensen, J. and J. Newman, (2004) A mathematical model for the lithium-ion negative electrode solid electrolyte interphase. *Journal of The Electrochemical Society.* 151(11): p. A1977-A1988.
14. Goodenough, J.B. and K.S. Park, (2013) The Li-ion rechargeable battery: a perspective. *J Am Chem Soc.* 135(4): p. 1167-76.

15. CM Julien, A.M., K Zaghib, H Groult, (2014) Comparative Issues of Cathode Materials for Li-Ion Batteries. *inorganics*. 2(1): p. 132-154.
16. Manthiram, A., (2011) Materials challenges and opportunities of lithium ion batteries. *The Journal of Physical Chemistry Letters*. 2(3): p. 176-184.
17. Goodenough, J.B. and Y. Kim, (2009) Challenges for rechargeable Li batteries. *Chemistry of Materials*. 22(3): p. 587-603.
18. Kim, J.-H., et al., (2004) Phase Transitions in $\text{Li}_{1-\delta}\text{NiO} \cdot 5\text{Mn}_{1-\delta}\text{O}_4$ during Cycling at 5 V. *Electrochemical and solid-state letters*. 7(7): p. A216-A220.
19. Laubach, S., et al., (2009) Changes in the crystal and electronic structure of LiCoO_2 and LiNiO_2 upon Li intercalation and de-intercalation. *Physical Chemistry Chemical Physics*. 11(17): p. 3278-3289.
20. Venkatraman, S., Y. Shin, and A. Manthiram, (2003) Phase Relationships and Structural and Chemical Stabilities of Charged $\text{Li}_{1-x}\text{CoO}_{2-\delta}$ and $\text{Li}_{1-x}\text{NiO} \cdot 85\text{CoO} \cdot 15\text{O}_{2-\delta}$ Cathodes. *Electrochemical and solid-state letters*. 6(1): p. A9-A12.
21. Choi, J., et al., (2006) Proton insertion into oxide cathodes during chemical delithiation. *Electrochemical and solid-state letters*. 9(5): p. A241-A244.
22. Newman, J. and K.E. Thomas-Alyea, *Electrochemical systems*. 2012: John Wiley & Sons.
23. Doyle, M., T.F. Fuller, and J. Newman, (1993) Modeling of galvanostatic charge and discharge of the lithium/polymer/insertion cell. *Journal of the Electrochemical Society*. 140(6): p. 1526-1533.
24. Bazant, M.Z., (2013) Theory of Chemical Kinetics and Charge Transfer based on Nonequilibrium Thermodynamics. *Accounts of chemical research*. 56(5): p. 1144-1160.
25. Li, Y., et al., (2014) Current-induced transition from particle-by-particle to concurrent intercalation in phase-separating battery electrodes. *Nat Mater*. 13(12): p. 1149-56.
26. Pletcher, D. and R.S.o. Chemistry, *A First Course in Electrode Processes*. 2009: Royal Society of Chemistry.
27. Valøen, L.O. and J.N. Reimers, (2005) Transport Properties of LiPF_6 -Based Li-Ion Battery Electrolytes. *Journal of The Electrochemical Society*. 152(5): p. A882.
28. Reddy, T., *Handbook of batteries*. 2002: McGraw-Hill Pub.
29. Buqa, H., et al., (2005) High rate capability of graphite negative electrodes for lithium-ion batteries. *Journal of the Electrochemical Society*. 152(2): p. A474-A481.
30. Doyle, M. and Y. Fuentes, (2003) Computer simulations of a lithium-ion polymer battery and implications for higher capacity next-generation battery designs. *Journal of the Electrochemical Society*. 150(6): p. A706-A713.

31. Bazant, M. Z. 10.626 Electrochemical Energy Systems;Massachusetts Institute of Technology, MIT OpenCourseWare, <http://ocw.mit.edu>; license, Creative Commons BY-NC-SA, 2011.
32. García, R.E., et al., (2005) Microstructural Modeling and Design of Rechargeable Lithium-Ion Batteries. *Journal of The Electrochemical Society*. 152(1): p. A255.
33. Bazant, M. Z. 10.626 Electrochemical Energy Systems;Massachusetts Institute of Technology, MIT OpenCourseWare, <http://ocw.mit.edu>; license, Creative Commons BY-NC-SA, 2011.
34. Ebner, M. and V. Wood, (2014) Tool for Tortuosity Estimation in Lithium Ion Battery Porous Electrodes. *Journal of the Electrochemical Society*. 162(2): p. A3064-A3070.
35. Chung, D.-W., et al., (2013) Validity of the Bruggeman relation for porous electrodes. *Modelling and Simulation in Materials Science and Engineering*. 21(7): p. 074009.
36. Thorat, I.V., et al., (2009) Quantifying tortuosity in porous Li-ion battery materials. *Journal of Power Sources*. 188(2): p. 592-600.
37. Vijayaraghavan, B., et al., (2012) An Analytical Method to Determine Tortuosity in Rechargeable Battery Electrodes. *Journal of The Electrochemical Society*. 159(5): p. A548.
38. Shen, L. and Z. Chen, (2007) Critical review of the impact of tortuosity on diffusion. *Chemical Engineering Science*. 62(14): p. 3748-3755.
39. Kehrwald, D., et al., (2011) Local tortuosity inhomogeneities in a lithium battery composite electrode. *Journal of The Electrochemical Society*. 158(12): p. A1393-A1399.
40. Ebner, M., et al., (2013) X-Ray Tomography of Porous, Transition Metal Oxide Based Lithium Ion Battery Electrodes. *Advanced Energy Materials*. 3(7): p. 845-850.
41. Zielke, L., et al., (2015) Three-Phase Multiscale Modeling of a LiCoO₂ Cathode: Combining the Advantages of FIB-SEM Imaging and X-Ray Tomography. *Advanced Energy Materials*. 5(5): p. n/a-n/a.
42. Biesheuvel, P.M., Y. Fu, and M.Z. Bazant, (2011) Diffuse charge and Faradaic reactions in porous electrodes. *Physical Review E*. 83(6).
43. Pfleging, W. and J. Pröll, (2014) A new approach for rapid electrolyte wetting in tape cast electrodes for lithium-ion batteries. *Journal of Materials Chemistry A*. 2(36): p. 14918-14926.
44. IJESD, A., (2000) Costs of lithium-ion batteries for vehicles.
45. Daniel, C., (2008) Materials and processing for lithium-ion batteries. *Jom*. 60(9): p. 43-48.
46. Park, J.-K., *Principles and applications of lithium secondary batteries*. 2012: John Wiley & Sons.
47. Li, J., C. Daniel, and D. Wood, (2011) Materials processing for lithium-ion batteries. *Journal of Power Sources*. 196(5): p. 2452-2460.

48. Yoshio, M., R.J. Brodd, and A. Kozawa, *Lithium-Ion Batteries*. Vol. 1. 2009: Springer.
49. DANIEL, C., (2015) Lithium Ion Batteries and Their Manufacturing Challenges. *FRONTIERS OF ENGINEERING*. p. 45-50.
50. Anderson, D.L., *An evaluation of current and future costs for lithium-ion batteries for use in electrified vehicle powertrains*. 2009, Duke University.
51. Ramadesigan, V., et al., (2012) Modeling and simulation of lithium-ion batteries from a systems engineering perspective. *Journal of The Electrochemical Society*. 159(3): p. R31-R45.
52. Pinson, M.B. and M.Z. Bazant, (2013) Theory of SEI formation in rechargeable batteries: capacity fade, accelerated aging and lifetime prediction. *Journal of The Electrochemical Society*. 160(2): p. A243-A250.
53. Lu, P., et al., (2014) Chemistry, Impedance, and Morphology Evolution in Solid Electrolyte Interphase Films during Formation in Lithium Ion Batteries. *The Journal of Physical Chemistry C*. 118(2): p. 896-903.
54. Wood, D.L., J. Li, and C. Daniel, (2015) Prospects for reducing the processing cost of lithium ion batteries. *Journal of Power Sources*. 275: p. 234-242.
55. Yoon, S.-Y. and R. Iocco, *Split Charge Forming Process for Battery*. 2009, Google Patents.
56. Wu, M.-S., et al., (2004) Assessment of the wettability of porous electrodes for lithium-ion batteries. *Journal of applied electrochemistry*. 34(8): p. 797-805.
57. Zhang, S.S., (2006) A review on electrolyte additives for lithium-ion batteries. *Journal of Power Sources*. 162(2): p. 1379-1394.
58. Zhang, S.S., (2007) A review on the separators of liquid electrolyte Li-ion batteries. *Journal of Power Sources*. 164(1): p. 351-364.
59. Wang, X., et al., (2005) New Additives to Improve the First-Cycle Charge–Discharge Performance of a Graphite Anode for Lithium-Ion Cells. *Journal of The Electrochemical Society*. 152(10): p. A1996-A2001.
60. Miller, E. and R. Miller, (1956) Physical theory for capillary flow phenomena. *Journal of Applied Physics*. 27(4): p. 324-332.
61. Xiong, Y., (2014) Flow of water in porous media with saturation overshoot: A review. *Journal of Hydrology*. 510: p. 353-362.
62. Bear, J., *Dynamics of fluids in porous media*. 2013: Courier Corporation.
63. Allaire, G., et al., (2013) Ion transport in porous media: derivation of the macroscopic equations using upscaling and properties of the effective coefficients. *Computational Geosciences*. 17(3): p. 479-495.

64. Courbin, L., et al., (2009) Dynamics of wetting: from inertial spreading to viscous imbibition. *Journal of Physics: Condensed Matter*. 21(46): p. 464127.
65. Reyssat, M., et al., (2009) Imbibition in layered systems of packed beads. *EPL (Europhysics Letters)*. 86(5): p. 56002.
66. Courbin, L., et al., (2007) Imbibition by polygonal spreading on microdecorated surfaces. *Nature materials*. 6(9): p. 661-664.
67. Ishino, C., et al., (2007) Wicking within forests of micropillars. *EPL (Europhysics Letters)*. 79(5): p. 56005.
68. Martinez, A.W., S.T. Phillips, and G.M. Whitesides, (2008) Three-dimensional microfluidic devices fabricated in layered paper and tape. *Proceedings of the National Academy of Sciences*. 105(50): p. 19606-19611.
69. Fenton, E.M., et al., (2008) Multiplex lateral-flow test strips fabricated by two-dimensional shaping. *ACS applied materials & interfaces*. 1(1): p. 124-129.

CHAPTER 2 Electrolyte wetting in anode and cathode

2.1 Introduction

Lithium ion batteries have been widely used in consumer electronic devices and are advancing into high performance applications such as transportation [1-3]. The lithium ion battery is mainly composed of porous electrode films (anode and cathode), separator sheets, and electrolyte. The liquid electrolyte is the transport medium in which the charged ions can flow between anode and cathode in the battery [4, 5]. The porous electrodes, both anode and cathode, provide space to accommodate liquid electrolyte, and the electrochemical process for charge and discharge [6]. To achieve better utilization of electrode capacity, improved electrolyte wetting (or transport) in the porous electrode is needed to increase the contact between electrolyte and active particle surface [7]. The pore size for porous electrodes is varied from tens of nanometer to several micrometers. The vast difference in pores size makes the injection of electrolyte into electrode films an intricate process. Electrolyte wetting properties become much more important when batteries are scaled from coin cell to pouch cell in industry manufacturing [8].

The electrolyte wetting in the electrode film is affected by properties of both electrolyte and electrode microstructure. There is little research about the effect the electrolyte, and even less about effects of electrode microstructure. Based on capillary flow model, Wu et al. investigated the wetting behavior of lithium cobalt oxide (LiCoO_2) and mesocarbon microbead (MCMB) electrodes in different liquid electrolytes [9]. Stefan et al. [10] investigated the wetting of separator sheets (Celgard, Separion) and electrodes (LiCoO_2 , $\text{Li}_4\text{Ti}_5\text{O}_{12}$, graphite) by ionic liquids, and Dahbi et al. [11] reported on interfacial properties of graphite electrodes and Celgard separators by liquid electrolytes. Kuhnelt et al. [12] studied wetting properties of porous electrodes in

electrolytes based on organic solvents and ionic liquids. Their research proved that, according to Lucas-Washburn equation, viscosity and surface tension are two important parameters of electrolyte solutions used to characterize wetting rate of electrolyte in the electrode films. The change of salt concentration and electrolyte additives will result in the change of surface tension and viscosity, which will impact the electrolyte wetting rate. However, due to the complex nature of porosity, pore shape and pore size distribution, the effects of electrode microstructure are still unclear.

The link between electrode microstructure and electrolyte wetting is important phenomena to understand. Battery performance will be dictated by the ability of Li ions to diffuse in the electrolyte throughout porous electrodes [13]. Understanding the transport behavior of these porous electrodes is critically important for understanding battery performance and designing electrode microstructure [14,15]. Electrolyte transport properties become increasingly more important when batteries are scaled from coin cells used in research to pouch cells used in larger-scale applications. Currently, energy and power density of pouch cell is limited by the transportation of ions in the electrolyte [16-18]. In addition, improved electrolyte wetting in electrodes will reduce manufacturing cost by improving the filling, charging and aging processes [19]. Therefore, it is of great interest to better understand the electrolyte transport process in electrodes.

In this research, the wetting balance test was used to reveal the electrolyte transport performance in two typical porous electrodes: graphite with a flaky particle morphology and NMC with agglomerated spherical particle morphology. One standard electrolyte solution was used for all tests. The transport rate was calculated from the modified Lucas-Washburn equation [9, 20]. It was found that the electrolyte wetting rate in graphite electrode film was faster than in the NMC films.

A set of 15 tests were done to explore statistic properties, as all the films will have some variability in thickness ($<3\text{ }\mu\text{m}$) from one location to another. Transport was also more stable in graphite film than in NMC film as revealed by the standard deviation in test results. Cross sectional scanning electron microscopy (SEM) imaging was used to analyze the pore morphology and particle / pore size distribution. Finally, mercury intrusion porosimetry, which thus far has been used in other studies for only basic porosity measurements [9, 12], was employed to reveal the structure of the porous electrodes including the critical pore size and threshold pore size of the pore networks. The wetting properties of electrodes are discussed by their microstructure.

2.2 Materials and Methods

The electrode films and electrolyte solution were supplied by Johnson Controls, Inc. The electrode film consisted of active material (graphite or NMC), carbon black, binder and metal foil used as current collector. Anode is composed of 95wt% graphite particles with d_{50} of approximately 7-10 μm , with the remainder binder and conductive carbon black. Cathode is composed of 95wt% NMC with d_{50} of agglomerated particles at 6-9 μm , with the remainder of binder and conductive carbon black. Electrodes were coated on both sides. Loading weight variation in producing electrode films was within 3% over the length of foil. The electrolyte solution used was 3:7 (volumetric ratio) EC: EMC with 1.2M LiPF_6 .

The wetting balance tests were carried out in a custom-made set-up, as depicted in Figure 2-1. During the test, the chamber was purged with flowing high purity argon. A polymer beaker containing test liquid electrolyte was placed on a lifting stage under the suspended sample. The electrode sample size for all tests was 10x50mm. During measurement, the stage moved up with a speed of 5mm/s until the sample was immersed 5 mm into the electrolyte. Then a transport

wetting process happened from electrolyte to electrode. Weight change during the wetting process in the sample was recorded dynamically by the balance connected to a computer, and mass versus time ($m-t$) curve was formed.

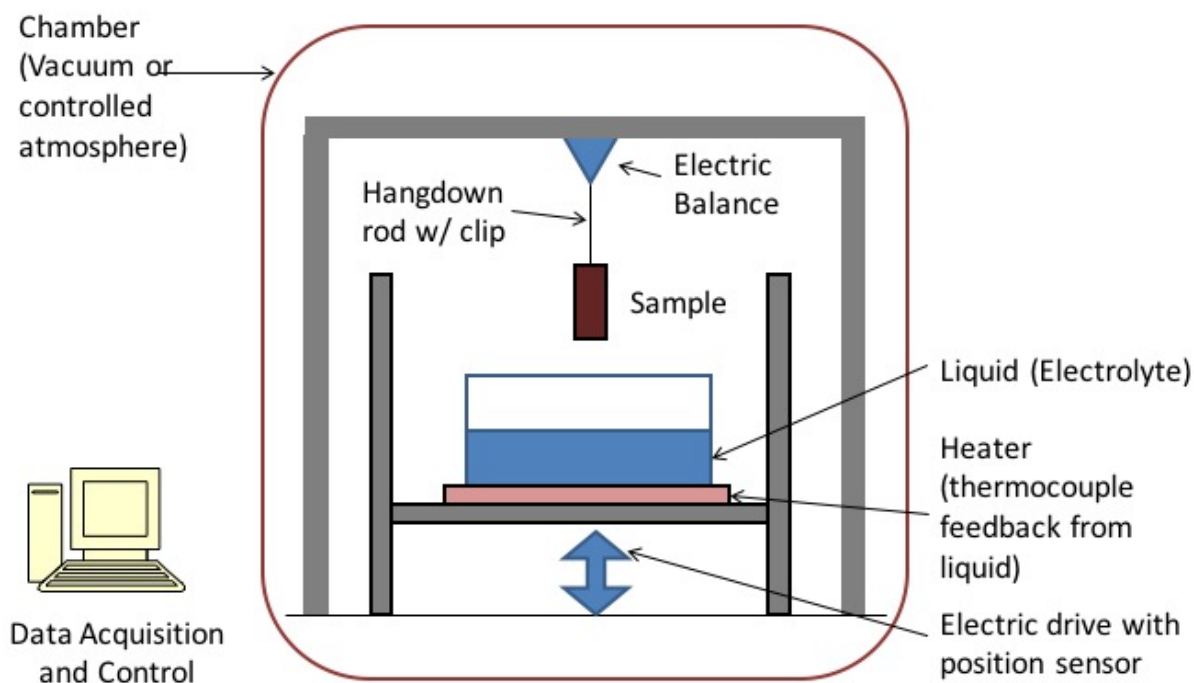


Figure 2-1 Schematic diagram for wetting balance test set-up.

Electrode films were prepared for SEM characterization by mounting vertically in a sample holder and infiltrating with a low viscosity epoxy resin solution. After 14 h of curing at room temperature, the epoxy resin molds were ground and polished with emery papers of successively finer grit size of 240, 800, 1000, 1200 and 2000 grit, followed by diamond abrasives of sizes 9, 3, and 0.25 μm . The polished samples were cleaned and air dried before imaged using a Hitachi S-4800 FE-SEM with BSE detector.

Mercury intrusion porosimetry (MIP) tests were performed on a Micromeritics AutoPore IV 9510. Electrode films were vacuum dried at 105°C overnight before each test. The maximum applied pressure of mercury was 414 MPa, equivalent to a Laplace throat diameter of 0.004 µm (4nm). The equilibration time at each of the increasing applied pressures of mercury was set to 10 s, and a sample mass of approximately 1.0 g was used. Contact angle and surface tension of mercury was assumed to be 130° and 485 mN/m, respectively.

2.3 Results and Discussion

The active material film on each electrode can be modeled as a porous medium composed of bundled capillary tubes, and the electrolyte wetting process in the electrode as a spontaneous liquid adsorption driven by capillary force [9]. This can be considered as capillary imbibitions process. Inertia and gravity influence is neglected for simplification [21]. The relation of electrolyte weight change with time in the electrode film can be described by modified Lucas-Washburn equation, equation 2-1a and 2-1b. More details about the equation can be found in literature [9, 12, 19].

$$\frac{\Delta m}{\rho_{sol} \cdot A_e} = K \sqrt{t} \quad (2-1a)$$

$$K = P \sqrt{\frac{\bar{r}_{eff} \gamma_{lv} \cos \theta}{2\eta}} \quad (2-1b)$$

where t is time, Δm : weight of electrolyte in m - t curve, ρ_{sol} : solution density, A_e : cross-section area of sample, K : wetting rate of electrolyte in porous electrode, P : electrode porosity, \bar{r}_{eff} : effective pore radius of electrode, γ_{lv} : surface tension of electrolyte solution, $\cos \theta$: contact angle of electrolyte with electrode, η : viscosity of electrolyte solution.

A typical $m-t$ curve is shown in Figure 2-2a. There is a fast weight increase in the beginning of immersing the sample due to spreading of electrolyte on the electrode surface. After immersion, slower electrolyte transport into the porous electrode occurred and this is the main region of interest where wetting rate can be assessed. Wetting was allowed to proceed for 7-8 minutes after which time the sample was withdrawn from the solution which can be seen by the rapid weight loss. After the sample is withdrawn, mass continues to decrease gradually as the solution evaporates from the porous film. The diffusion part in Figure 2-2a can be analyzed by transferring time into the square root of time and dividing the sample mass by the cross section area of the active material and the solution density, as shown in Figure 2-2b. The resulting slope from a linear curve fit is the electrolyte transport rate. Therefore, transport rate, K , for the sample shown in Figure 2-2 is $0.240\text{mm/s}^{0.5}$, with curving fitting parameter R^2 value of 0.998. This confirms that the electrolyte wetting process in electrode films can be characterized with root time behavior, which is typical behavior for capillary rise [22].

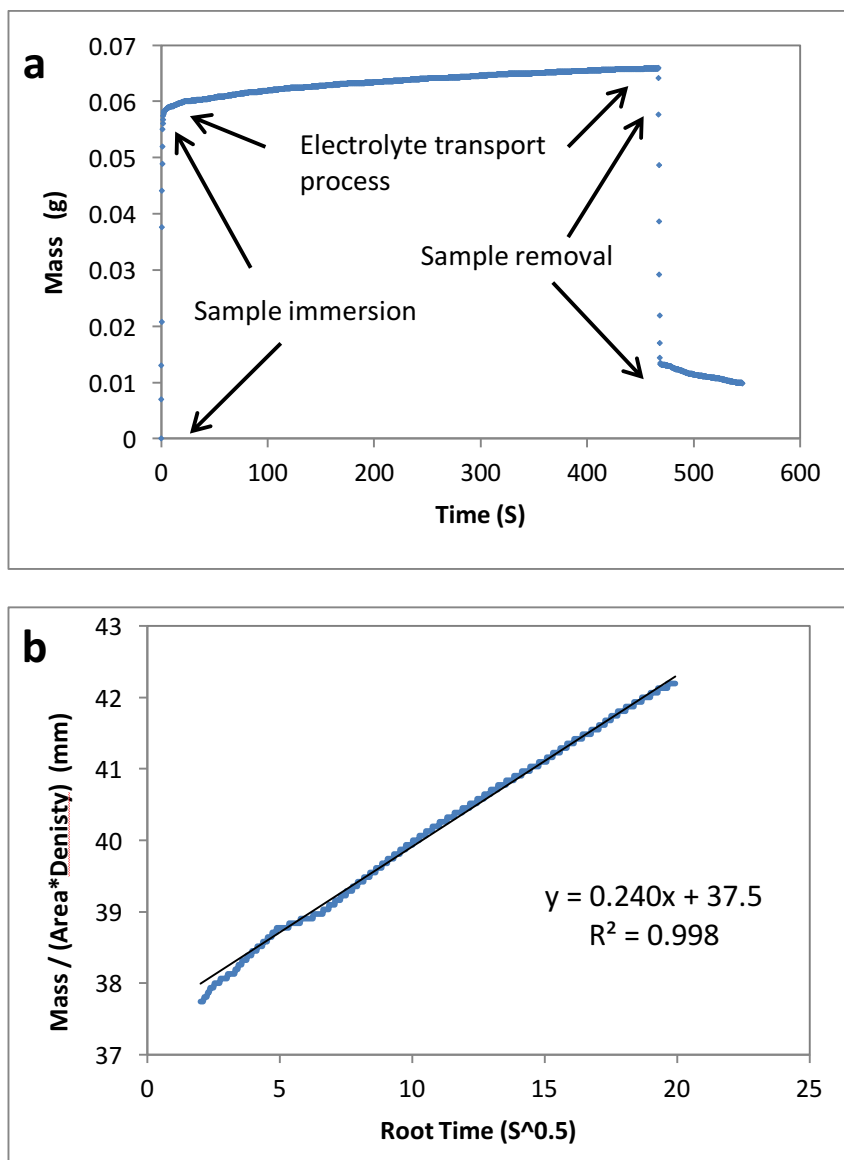


Figure 2-2 a) a typical m-t curve from wetting balance test, b) analysis about electrolyte transport process part of m-t curve by transferring time to root time, and dividing mass by sample cross section area and solution density. The resulting slope from linear curve fitting is the transport rate, K .

A total of 15 samples were tested for each graphite anode and NMC cathode to account for experimental and electrode film variations. The wetting rates for all the tests are shown in Figure 2-3. Electrolyte was found to transport faster in the anode than in the cathode. The Wetting rate

averaged $0.244 \text{ mm/s}^{0.5}$ for anode, and $0.175 \text{ mm/s}^{0.5}$ for cathode. Statistical results are summarized in Table 2-1. Results for the wetting rate match the Lucas-Washburn equation as can be seen by the high average R^2 curve fitting values (from the slope of mass versus root-time) of 0.997 and 0.992 for anode and cathode, respectively. Error% in the table is defined as standard deviation divided by average wetting rate which is also similar to coefficient of variation and this was used to describe measurement stability. The error% in anode is 6.79% which is slightly smaller than the value of 8.00% observed in cathode samples

Table 2-1 Summary for wetting balance test, wetting rate (K) are averaged data of 15 samples for each film type.

	Average Wetting Rate, $K(\text{mm/S}^{0.5})$	Standard Deviation	Average R^2	Error%	Samples (n)
Anode	0.244	0.017	0.997	6.97	15
Cathode	0.175	0.014	0.992	8.00	15

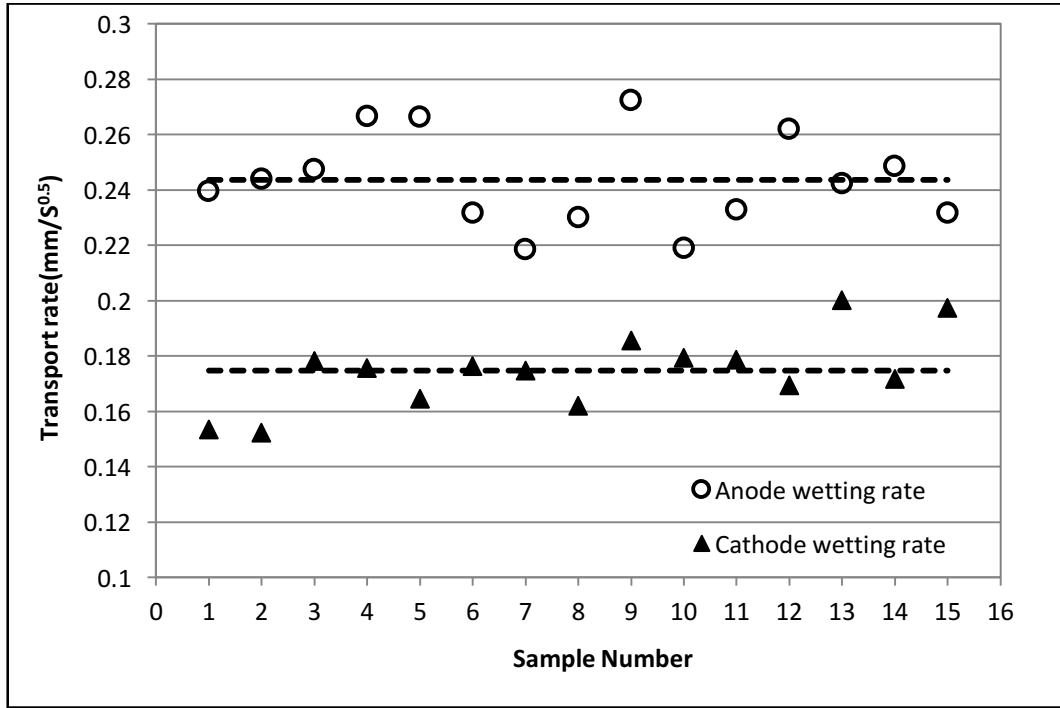


Figure 2-3 Transport rates for anode and cathode samples. Hollow circles are the wetting rate of electrolyte in anode; solid triangles are the transport rate of cathode. Dashed lines are the average wetting rate for each foil type.

In this work, the same electrolyte solution was used for all the tests. As described in equation 2-1b, the wetting rate is related to porosity, effective pore radius, and contact angle when considering the effects of electrode only. Direct measure of the contact angle for porous medium is very difficult [23]. Thus, contact angle is still an unknown effect in this research. The effects of porosity, and electrode microstructure like pore diameter, pore morphology and connectivity are investigated in more detail using mercury intrusion porosimetry.

The MIP measures pore diameters from nanometer to micrometer scale which match well with the pore range in the electrode film samples. Results of MIP for anode and cathode are shown in Figure 2-4 and summarized in Table 2-2. Porosity of the anode was 43.53% which was larger than that of cathode which was 36.36%. The median pore size for both were similar in which anode was 0.7741

μm , cathode was $0.7206 \mu\text{m}$. Average pore diameter for anode was $0.5713 \mu\text{m}$, and decreased to $0.2943 \mu\text{m}$ for cathode. From Figure 2-4, cumulative intrusion curve, the total intrusion volume for the anode (0.2244 mL/g) was bigger than that for the cathode (0.1495 mL/g).

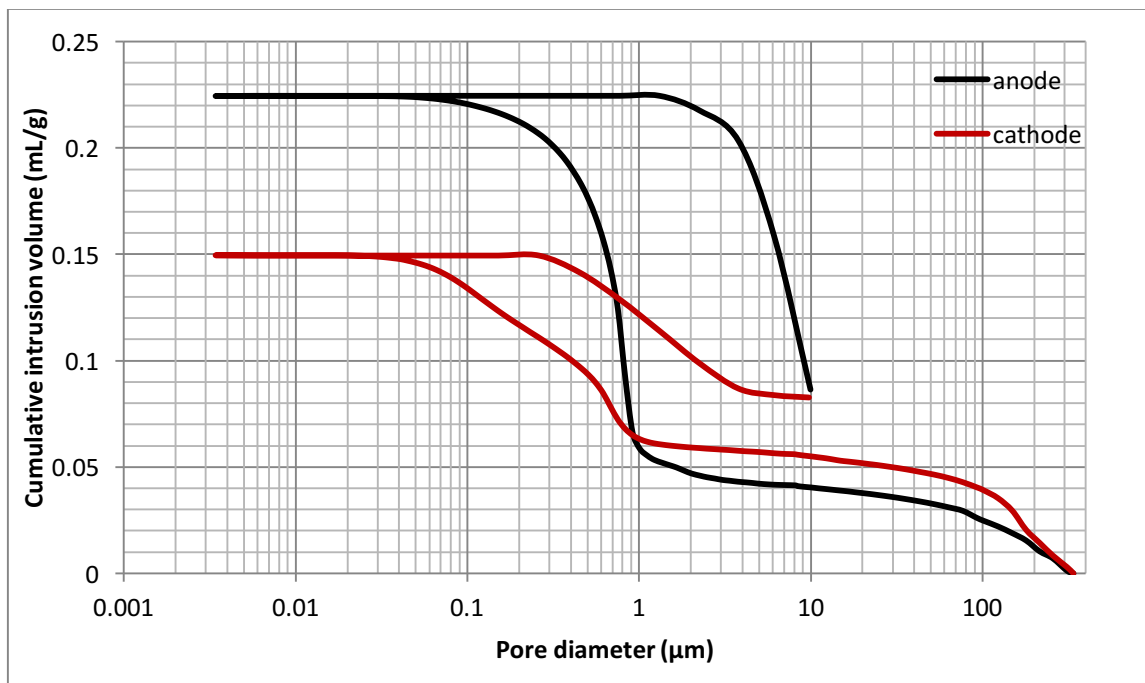


Figure 2-4 Cumulative intrusion curves for anode and cathode electrodes.

Table 2-2 summary for general MIP results.

	Porosity (%)	Total intrusion volume (mL/g)	Average Pore Diameter (μm)	Median Pore Diameter (μm)	Film Thickness (mm)
Anode	43.53	0.2244	0.5713	0.7741	0.15
Cathode	36.36	0.1495	0.2943	0.7206	0.13

Normalized cumulative intrusion curves, shown in Figure 2-5, were obtained by dividing the cumulative intrusion volume with the total intrusion volume for each sample. The intrusion process begins with pores that have the largest diameters and proceeds to pores of continually decreasing diameter [24]. The intrusion rate is much slower in the large pore region. Mercury begins to flow slowly from the exterior of the specimen to all portions of its interior, probably through long and tortuous path [24]. When a pore size smaller than a threshold pore diameter is achieved by increasing the pressure placed on the mercury, further intrusion occurs rapidly with filling of the nearby smaller pores [24, 25]. The fastest intrusion rate occurs when the pore diameter decreases to a critical pore diameter value which is also the diameter for biggest connecting pore throat. The region showing a steep increase of the intrusion volume can be related to the connected pore volume for that particular pore size. In the normalized intrusion curve, this connected porosity region is also the ratio of connecting volume to total pore volume or the percent of total porosity.

As seen in Figure 2-5, differentiated curves are used to indicate parameters like critical, threshold, and connecting pore sizes. Pore size characteristics for anode and cathode films are summarized in Table 2-3. For anode, there was a small portion, 4.0%, of *I* level connected pores in the critical size 1.825 μm , threshold size 2.275 μm . The majority of connected pores have a critical diameter of 0.829 μm , threshold diameter of 1.363 μm and accounts for 73.6% of the total pore volume. This indicates that the pores in the anode were well connected by 0.829 μm throat size. For the cathode, there were also two levels of connecting pores. The percentage of the total volume for the two levels of connecting pores was similar with values of 21.9% and 24.8% for the *I* and *II* networks, respectively. The *I* level of connected pores had a critical diameter of 0.617 μm and threshold diameter of 1.36 μm . The *II* level connected pore was much smaller with critical diameter only 0.08 μm , and threshold pore diameter 0.257 μm . Existence of connecting pores for both anode

and cathode indicate that the connecting pores play a significant role for electrolyte transport in the active material layers. Compared with Washburn's bundled capillary tube model, the transport in the electrode is more complicated. Pores in the electrode film are a network of pore cavity connected by pore throat. This is verified by SEM characterization, as shown in Figure 2-6. Effective pore radius (\bar{r}_{eff}) is a simplified pore diameter of a porous medium and is varied to meet the experiment results using the Lucas-Washburn equation [26]. The parameter lacks a precise physical definition which makes it difficult to relate it to practical applications, especially where complicated porous structures exist.

Table 2-3 Connecting pore diameters from normalized cumulative intrusion curves.

	Pore Networks	Critical pore diameter (um)	threshold pore diameter (um)	Percentage of total Pore volume
Anode	<i>I</i>	1.825	2.275	4%
	<i>II</i>	0.829	1.363	73.60%
Cathode	<i>I</i>	0.617	1.36	21.90%
	<i>II</i>	0.08	0.257	24.80%

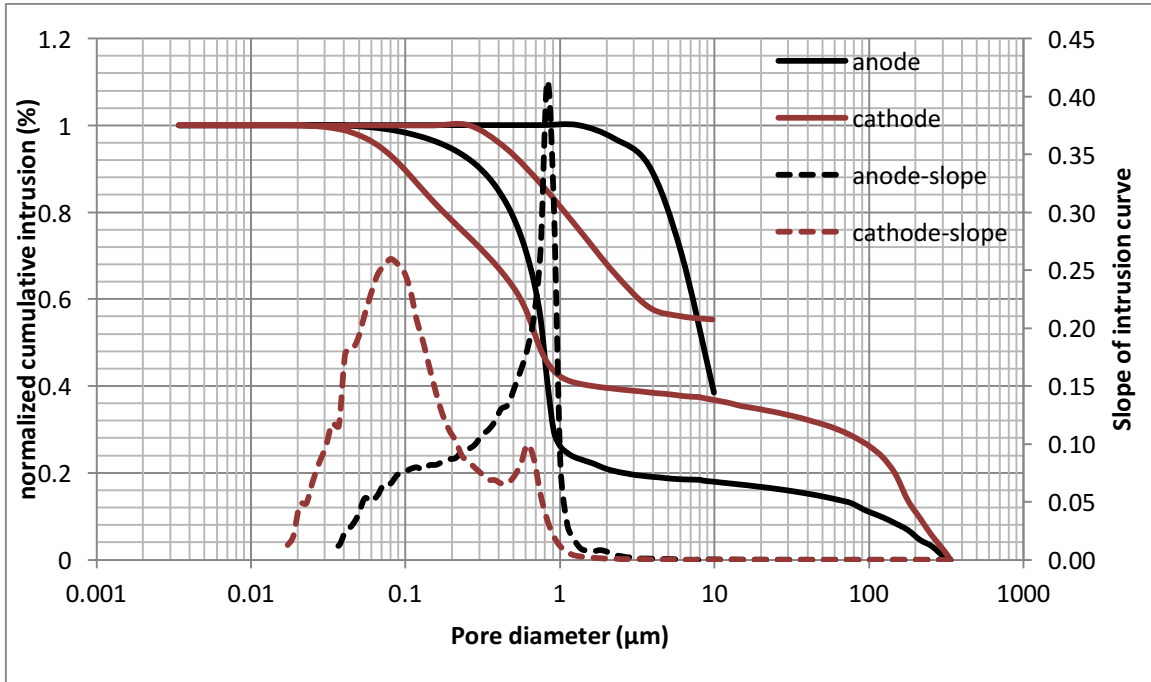


Figure 2-5 Normalized cumulative intrusion curve for anode and cathode. Secondary vertical axial is the slope of the intrusion curve.

Cross-sectional BSE-SEM image in Figure 2-6 show the representative pore structure in the electrode films. Figures 2-6a and 6c are images for anode in which the middle white region is copper foil. The graphite particle is flaky and is roughly aligned in a parallel fashion. In Figure 6a, the dark black regions are pores filled by epoxy resin. There are irregular pore cavities among three or more particles. The biggest diameter for these irregular pore cavities is in the range of 8-10 μm . The larger pore cavities are found around larger graphite particles. The distance between two nearby parallel particles is narrow. It can be seen in Figure 6c that most distance between two particles is less than 1 μm . This supports the MIP results which indicate the majority of connected pores have a critical diameter of 0.825 μm threshold diameter of 1.363 μm , and account for 73.6% of the total volume. Therefore, the electrode microstructure is composed of connected pore networks in which pore cavities are connected by pore throats that restrict transport into the cavities.

Further research should be done to explain the effects of pore network in electrolyte transport and in lithium ion battery performance.

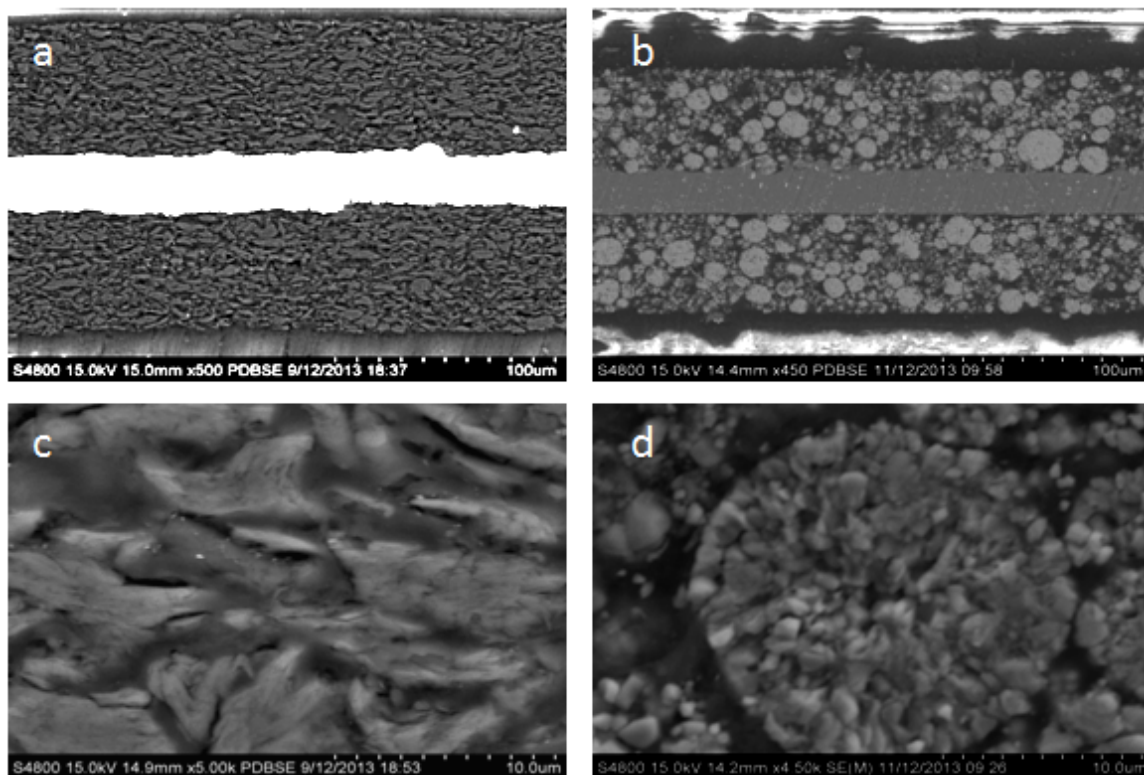


Figure 2-6 Cross-sectional backscattered electron (BSE) SEM images of electrodes. a), and c) for anode, b) and d) for cathode.

Cross sectional images for cathode electrodes are shown in Figure 2-6b and 6d. The middle gray region of Figure 2-6b is the aluminum foil used as the current collector. Brighter spherical particles are the NMC agglomerated particles with particle size in the range of 6-10 μm . Some agglomerated particles were peeled off during polishing in preparing the SEM samples. Space between spherical particles was larger than 1 μm , as revealed in magnified Figure 2-6d. This correlates with the MIP measurements, pores with sizes bigger than 1 μm account for almost 40% of the total pore volume. The pore network I is the connection of agglomerated particles with neighboring particles (inter-

particle pores). It is reasonable to think the pore network *II* with a size of 0.08 μm is inside agglomerated sphere due to its dense particle assembly (intra-particle pores). These intra-particle pores in the cathode would contribute to the overall porosity measured by MIP but may not contribute significantly to the electrolyte transport as measured with the wetting balance test. Thus, electrolyte wetting in the NMC cathode can be divided into two parts, one is transporting between agglomerated particles, and the other is diffusing inside agglomerated particles.

2.4 Conclusion

The electrolyte wetting process in lithium-ion battery anode and cathode films were characterized using the wetting balance method. Electrolyte was found to transport faster in anodes than cathodes, with average wetting rates of 0.244 $\text{mm/s}^{0.5}$ (+/- 6.79%) and 0.175 $\text{mm/s}^{0.5}$ (+/- 8.00%) respectively. Mercury intrusion porosimetry tests showed the anode films had higher overall porosity and larger pore sizes relative to the cathode films. The MIP tests also showed that both films had a major connected pore network of a similar size range of roughly 0.8 to 1.3 μm although this network was slightly larger and accounted for a much higher percentage of total porosity for the anode film relative to the cathode film. SEM and MIP results showed that the cathode had both inter- and intra-particle porosity with the intra-particle pores accounting for a significant fraction (24.8%) of the total porosity while the anode film did not have this small-scale intra-particle pore structure. The higher overall porosity, larger pore size, and higher volume percentage of large connected pores likely account for the faster wetting of the anode films relative to the cathode films.

A simplified expression of the effective pore radius (\bar{r}_{eff}) in the Lucas-Washburn equation does not have a practical basis when the porous structure is complicated as is the case with electrode

films. Based on the combined results from MIP and SEM characterization, the electrode microstructure is composed of connected pore networks in which pore cavities are connected by pore throats of restricted size relative to the larger pore cavities. This pore-network model is different from other electrode microstructure models based on properties like pore size distribution and morphology. MIP testing was shown to provide additional information related to wetting performance beyond the parameters of porosity and average pore size that have been used by other researchers. These findings are helpful for future research about electrolyte transport in the porous electrode films and show the additional insight that can be gained from relating wetting balance tests to MIP and SEM characterization methods. Further research should be done to explain the effects of the pore network on electrolyte transport and to relate wetting rates with lithium ion battery performance.

References

1. Scrosati, Bruno, and Jürgen Garche. Lithium batteries: Status, prospects and future. *Journal of Power Sources* 195.9 (2010): 2419-2430.
2. The Boston Consulting Group, Batteries for Electric Vehicles: Challenges, Opportunities, and the Outlook to 2020, January, 2010
3. Tarascon, J-M., and Michel Armand. Issues and challenges facing rechargeable lithium batteries. *Nature* 414.6861 (2001): 359-367.
4. Ramadesigan, Venkatasailanathan, et al. Modeling and simulation of lithium-ion batteries from a systems engineering perspective. *Journal of The Electrochemical Society* 159.3 (2012): R31-R45.
5. Daniel, Claus. Materials and processing for lithium-ion batteries. *JOM* 60.9 (2008): 43-48.
6. Park, Jung-Ki, ed. Principles and applications of lithium secondary batteries. *John Wiley & Sons*, 2012.
7. Vu, Anh, Yuqiang Qian, and Andreas Stein. Porous Electrode Materials for Lithium - Ion Batteries—How to Prepare Them and What Makes Them Special. *Advanced Energy Materials* 2.9 (2012): 1056-1085.
8. Civan, F. 2001. Scale effect on porosity and permeability — Kinetics, model, and correlation. *AIChE Journal*, 47(2), pp. 271 – 287
9. Wu MS, Liao TL, Wang YY, Wan CC (2004) Assessment of the wettability of porous electrodes for lithium-ion batteries. *J Appl Electrochem* 34:797–805
10. Stefan CS, Lemordant D, Claude-Montigny B, Violleau D (2009) Are ionic liquids based on pyrrolidinium imide able to wet separators and electrodes used for Li-ion batteries? *J Power Sources* 189:1174–1178
11. Dahbi M, Violleau D, Ghamouss F, Jacquemin J, Tran-Van F, Lemordant D, Anouti M (2012) Interfacial properties of LiTFSI and LiPF₆-based electrolytes in binary and ternary mixtures of alkylcarbonates on graphite electrodes and Celgard separator. *Ind Eng Chem Res* 51:5240–5245
12. Kühnel, Ruben-Simon, et al. "Evaluation of the wetting time of porous electrodes in electrolytic solutions containing ionic liquid." *Journal of Applied Electrochemistry* 43.7 (2013): 697-704.
13. Gordon, Michael, and Galen Suppes. "Li - ion battery performance in a convection cell configuration." *AIChE Journal* 59.5 (2013): 1774-1779.
14. Park, Myounggu, et al. A review of conduction phenomena in Li-ion batteries. *Journal of Power Sources* 195.24 (2010): 7904-7929.

15. Ebner, Martin, et al. Tortuosity Anisotropy in Lithium-Ion Battery Electrodes. *Advanced Energy Materials* 4.5 (2014).
16. Cannarella, John, and Craig B. Arnold. Ion transport restriction in mechanically strained separator membranes. *Journal of Power Sources* 226 (2013): 149-155.
17. Nyman, Andreas, Mårten Behm, and Göran Lindbergh. "Electrochemical characterisation and modelling of the mass transport phenomena in LiPF₆-EC-EMC electrolyte." *Electrochimica Acta* 53.22 (2008): 6356-6365.
18. Ramadesigan, Venkatasailanathan, et al. "Optimal porosity distribution for minimized ohmic drop across a porous electrode." *Journal of The Electrochemical Society* 157.12 (2010): A1328-A1334.
19. Pfleging, W., R. Kohler, and J. Pröll. "Laser generated microstructures in tape cast electrodes for rapid electrolyte wetting: new technical approach for cost efficient battery manufacturing." *SPIE LASE*. International Society for Optics and Photonics, 2014.
20. Washburn, Edward W. "The dynamics of capillary flow." *Physical review* 17.3 (1921): 273.
21. Xiao, Yan, Fuzheng Yang, and Ranga Pitchumani. "A generalized analysis of capillary flows in channels." *Journal of colloid and interface science* 298.2 (2006): 880-888.
22. Alava, Mikko, Martin Dubé, and Martin Rost. "Imbibition in disordered media." *Advances in Physics* 53.2 (2004): 83-175.
23. Lavi, Becky, Abraham Marmur, and Joerg Bachmann. "Porous media characterization by the two-liquid method: effect of dynamic contact angle and inertia." *Langmuir* 24.5 (2008): 1918-1923.
24. Aligizaki, Kalliopi K. *Pore structure of cement-based materials: testing, interpretation and requirements*. CRC Press, 2005.
25. Kaufmann, Josef, Roman Loser, and Andreas Leemann. "Analysis of cement-bonded materials by multi-cycle mercury intrusion and nitrogen sorption." *Journal of colloid and interface science* 336.2 (2009): 730-737.
26. Cai, Jianchao, and Boming Yu. "A discussion of the effect of tortuosity on the capillary imbibition in porous media." *Transport in porous media* 89.2 (2011): 251-263. R.J. Brodd, C. Helou ; *Journal of Power Sources*, 231 (2013) 293-300

CHAPTER 3 EFFECTS OF CALENDERING ON WETTABILITY

3.1 Introduction

Demands for increased performance and lower costs for lithium ion batteries have been increasing. This can be achieved through the development of novel materials [1], battery architectures [2], and manufacturing techniques [3, 4]. Advances in battery performance have been primarily driven by the development of new cell materials, chemistries, and electrolytes [5], though theoretical limits for gravimetric or volumetric capacities have been identified [6-8]. Moreover, when a battery is examined at the system level in industry, issues like underutilization, capacity fade, thermal runaways, and low energy density will be obvious [2, 9]. More detailed understanding of how materials and resulting structures within the cell react to the manufacturing process can provide greater insight into relating processing to battery performance [10, 11].

Electrolyte injection occurs after cell assembly. Electrolyte is added to the cell by a precision pump and then vacuum filled to ensure that the electrolyte permeates and completely fills the pores in the separator and electrode structures [9, 12]. Wettability between the porous electrode film and electrolyte becomes important in this process since poor wettability can lead to incomplete filling or extended manufacturing times. Any un-wetted active material will cause an underutilization of electrode capacity and increased electrolyte resistance [13]. Wettability is usually improved by modifying the electrolyte with a wetting additive [14]. However, there is very little quantitative data about wettability in literature, and only simple qualitative observations, good, poor, and fair, were reported on the wettability of microporous separators [15]. Thus, a quantitative measurement for wettability can improve the understanding of wetting behavior, which can have potential performance or economic impacts.

As has been reported, wettability of electrodes can be tested by a wetting balance method [16, 17]. Wettability encompasses aspects of both the liquid electrolyte and the porous electrode materials. The primary electrolyte factors are viscosity and surface tension [16]. The influence of the porous electrode on the wetting rate is more complicated and has been investigated less [18]. It has been widely accepted that electrode microstructure resulting from the manufacturing process directly impacts energy, power, lifetime, and reliability of lithium ion batteries [2, 9, 19]. Due to the limited cell volume, electrodes also function as electrolyte reservoirs [9]. To obtain a high capacity retention at high current application, both the electronic and ionic conductivity of the electrodes must be optimal [10, 20]. A good ionic contact of all electrode particles as well as a sufficiently high lithium ion transport rate in the electrode pores are controlled by the amount of electrolyte that is retained in the electrodes as well as by the size and shape of electrode pores (tortuosity) [21,22]. Moreover, there are electrode thickness limitations related to the increased diffusive and ohmic losses from Li-ion transport through the electrolyte [23-25]. Therefore, understanding and controlling the wetting rate of electrolyte in electrode films is critical to developing high performance batteries and controlling reducing manufacturing cost by improving the filling, charging and aging processes.

In industry, calendaring has been considered to be a critical step in the production of high performance anodes [26]. Porosity and thickness of the electrode film will decrease with increasing calendaring. Calendaring would also be expected to change the pore structure of the electrode which would thereby impact the wetting behavior of the film. The wetting balance test was used to investigate the wetting behavior of an anode film as a function of degree of calendaring and related to structural parameters as characterized with electron microscopy and mercury

porosimetry. Relations between the development of the porous structure and the resulting wetting performance are discussed.

3.2 Materials and Methods

Anode electrodes containing graphite, acetylene black, and a binder, cross-linkable at elevated temperatures, were coated on a copper substrate. The anode slurry, coating and calendaring processes were prepared in a dry-room condition with an average dewpoint of -38°C . The electrodes were coated to a specified loading weight of approximately $4\text{-}5\text{mg}/\text{cm}^2$ with varying densities dependent on the electrode thickness. The electrolyte solution used was 3:7 (volumetric ratio) solution of EC: EMC with 1.2M LiPF_6 (all these chemicals come from BASF). A graphite anode film with an as-coated thickness of $59\text{ }\mu\text{m}$ was used as the baseline electrode film (thickness includes the $18\text{ }\mu\text{m}$ copper foil substrate). It was then calendared to produce electrode films with thickness of 55, 53, 49, and $41\text{ }\mu\text{m}$.

The wetting balance test was performed using a gravimetric technique to track sample mass during the liquid infiltration process with a custom-made immersion test system. The electrode sample was suspended under an analytical balance and a container of liquid was lifted to partially immerse the sample to a set depth. The balance recorded the weight change of the electrode sample as a function of time. The wetting balance test was carried out to measure the weight change of electrolyte inside of the electrode film, and the result was shown in a mass versus time curve (m - t curve). All testing was performed in an argon-purged environment. A modified Lucas-Washburn equation, as shown in equation 3-1, was used to quantitatively analyze the relation of sample mass change with time.

$$\frac{\Delta m}{\rho_{sol} \cdot A_e} = K\sqrt{t} \quad (3-1a)$$

$$K = P \sqrt{\frac{\bar{r}_{eff} \gamma_{lv} \cos \theta}{2\eta}} \quad (3-1b)$$

where t is time, Δm : sample weight in m - t curve, ρ_{sol} : solution density, A_e : cross-section area of sample, K : wetting rate of electrolyte in porous electrode, P : electrode porosity, \bar{r}_{eff} : effective pore radius of electrode, γ_{lv} : surface tension of electrolyte solution, $\cos \theta$: contact angle of the electrolyte with the electrode, and η : viscosity of the electrolyte solution. The wetting rate K can be obtained from a linear curve fit of a mass change versus the square root of time. The active material film on the electrodes can be modeled as a porous medium composed of bundled capillary tubes, and the electrolyte transport process in the electrode as a spontaneous liquid adsorption driven by capillary force [16]. This can be considered as a capillary imbibition process. Inertia and gravity influences are neglected for simplification [27]. More details about the modified Lucas-Washburn equation can be found in literature [16, 17, 28].

Electrode films were prepared for SEM characterization by mounting them vertically in a sample holder and infiltrating with a low viscosity epoxy resin solution. After 14 h of curing at room temperature, the epoxy resin molds were ground and polished with emery papers of successively finer grit size of 240, 800, 1000, 1200 and 2000 grit, followed by diamond abrasives of sizes 9, 3, and 0.25 μm . The polished samples were cleaned and air dried before imaged using a Hitachi S-4800 FE-SEM with backscattered electron (BSE) detector. Mercury intrusion porosimetry (MIP) tests were performed on a Micromeritics AutoPore IV 9510. The MIP measures pore diameters from nanometer to micrometer scale which matches well with the pore range in the electrode film samples. Electrode films were vacuum dried at 105 $^{\circ}\text{C}$ overnight before each test. The maximum

applied pressure of mercury was 414 MPa, equivalent to a Laplace throat diameter of 0.004 μm (4 nm). The equilibration time at each of the increasing applied pressures of mercury was set to 10 s, and a sample mass of approximately 1.0 g was used. Contact angle and surface tension of mercury was assumed to be 130° and 485 mN/m, respectively, for porosimetry calculations.

3.3 Results and Discussion

A total of 6 samples were tested for each electrode film condition to account for experimental and electrode film variations. An example of a single wetting balance test is shown in Figure 3-1 where sample mass is shown as a function of time. After an initial transient caused by the insertion of the sample into the liquid and the subsequent meniscus formation, the mass gain follows the root-time relation as described by equation 1a. Wetting rates as measured for each sample condition are shown in Table 3-1 and Figure 3-2. Wettability improved steadily with calendaring from the initial thickness of 59 μm to 53 μm and then decreased with additional calendaring beyond 53 μm . Averaged curving fitting parameters (R^2) from the determination of the wetting rate (K) were in the range from 0.9296 to 0.9936. This confirms that the electrolyte transport process in electrode films can be characterized with root time behavior, which is the expected behavior for capillary rise [29]. Error% as listed in Table 3-1 is defined as the standard deviation divided by the average wetting rate which is similar to a coefficient of variation and can be used to describe measurement stability. The error% for 59 μm film is 15.71%, and it is 15.59% for 55 μm films. The error% reaches lowest value in 53 μm which is 6.08%. When film is further compressed to 49 μm and 41 μm , the error% jump to 34.88% and 28.99% separately.

Table 3-1 Data summary of results from wetting balance test for all the electrode films.

Graphite anode film thickness (μm)	Average wetting rate ($\text{mm/s}^{0.5}$)	Stdev	Error (%)	Tested numbers	Averaged R^2
59 (as-coated)	0.375	0.059	15.71	6	0.9764
55	0.472	0.074	15.59	6	0.9863
53	0.589	0.036	6.08	6	0.9936
49	0.292	0.102	34.88	6	0.9296
41	0.206	0.060	28.99	6	0.9616

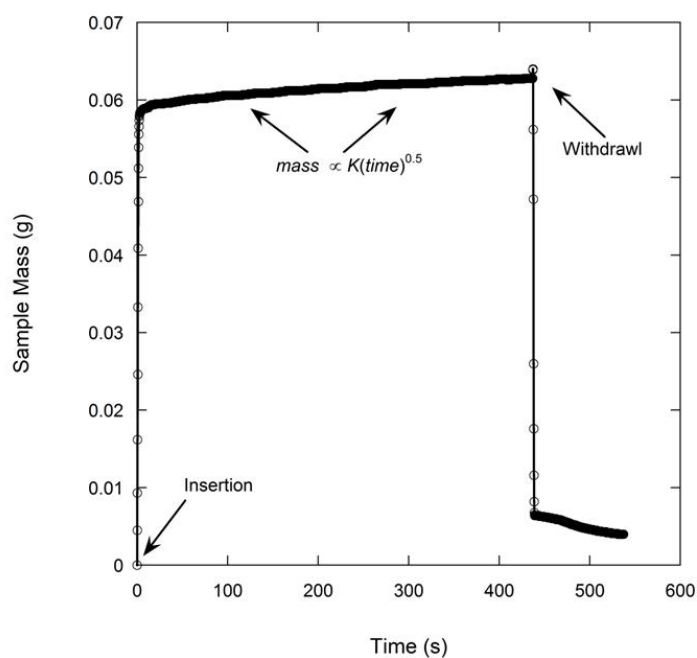


Figure 3-1 A typical mass vs time curve ($m-t$ curve) from wetting balance test.

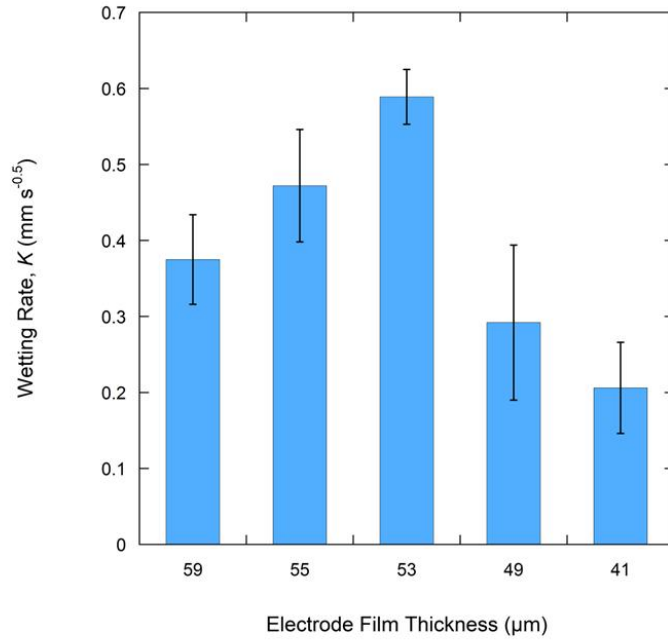


Figure 3-2 Wetting rate for electrode films calendaring under various pressure.

As described in equation 3-1b, the wetting rate is related to electrode properties including porosity and effective pore radius, electrolyte properties including viscosity and surface tension, and the combined electrode-electrolyte property of contact angle. In this work, the same electrolyte solution was used for all tests and same electrode film compositions were used, meaning that the graphite particles, binder, and conductive additives were constant. Thus, electrolyte effects are not a variable and the contact angle can be considered the same for all the tests. The wetting rate is only influenced by electrode porosity and the effective pore radius (\bar{r}_{eff}). According to the Washburn equation, the effective pore radius (\bar{r}_{eff}) is a simplified parameter describing the pore geometry of a porous medium and is varied to meet experiment results [30]. This parameter lacks a precise physical definition which makes it difficult to relate to practical applications, particularly where complicated pore structures exist. The average pore diameter as measured by MIP was used

to replace the more complex effective pore radius (\bar{r}_{eff}) value. Results of porosity and average pore diameter from mercury intrusion porosimetry are summarized in Table 3-2. Based on equation 1b, the product of porosity and the root of the effective pore radius would have a linear relation with the wetting rate. As shown in Figure 3-3, this relation is fairly linear for the anode samples calendared to various thicknesses. The linear curve fitting parameter (R^2) of this trend was 0.7242 and the largest deviations from the linear behavior were found with the 59 and 53 μm samples. These particular samples were the as-coated sample and the sample with the highest observed wetting rate, respectively.

Table 3-2 Results summary for porosity and average pore diameter from mercury intrusion porosimetry (MIP). *Wetting rates are from Table 3-1 and are repeated here for convenience.

Graphite anode film thickness (μm)	Porosity (%)	Average pore diameter(μm)	$p*r^{0.5}$	Average wetting rate ($\text{mm/s}^{0.5}$)*
59 (as-coated)	47.63	0.779	0.297	0.375
55	47.63	0.993	0.336	0.472
53	44.99	0.899	0.302	0.589
49	40.80	0.538	0.212	0.292
41	37.43	0.327	0.151	0.206

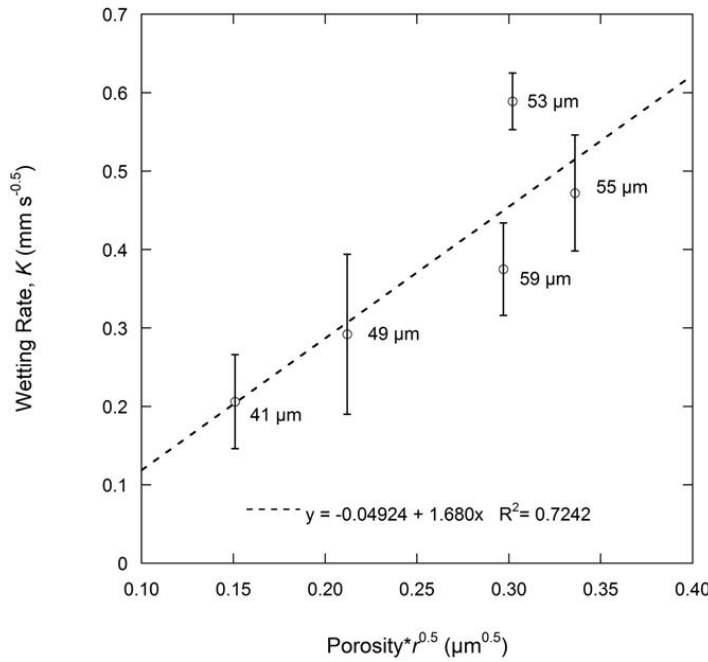


Figure 3-3 Wetting rate, K , as a function of porosity and average pore radius according to the Lucas-Washburn equation (1b). Average pore radius (r) is based on the average pore diameter as measured by MIP.

Electrode microstructure was observed with cross-sectional BSE-SEM imaging as shown in Figure 3-4. The backscattered images show the copper metal current collectors as bright white. Imaging of the graphite particles with the epoxy mounting material shows little contrast though several important features can be observed. The graphite particles are flaky and roughly aligned in a parallel fashion. The alignment increase with increasing calendaring. There are irregular pore cavities among three or more particles which can be found in all films. These cavities may function as electrolyte reservoirs inside the electrode films. Due to the limited overall cell volume required to produce cells with high volumetric properties, both electrodes and separators need to function as electrolyte reservoirs to have sufficient lithium ion transport rates [9]. The larger pore cavities tend to be found around larger graphite particles. The distance between two nearby parallel particles is narrow and forms channels between the larger cavities. The pore structure consists of

inter-connected throats (ducts) and cavities (nodes). Transport of electrolyte in these pore networks may include a converging-diverging feature [31]. Electrolyte converges in the cavities first, and then diverges into nearby throats. Therefore, the wetting rate of electrolyte is affected mainly by the inter-connection between throats and cavities, which is highly affected by the calendaring process. Additional manufacturing parameters beyond calendaring can also be used to manipulate the pore structure of the electrode films. Use of graphite particles of different morphologies (e.g. flake, round, peanut, etc) or manipulation of particle size distributions could be used to design or tailor these pore networks.

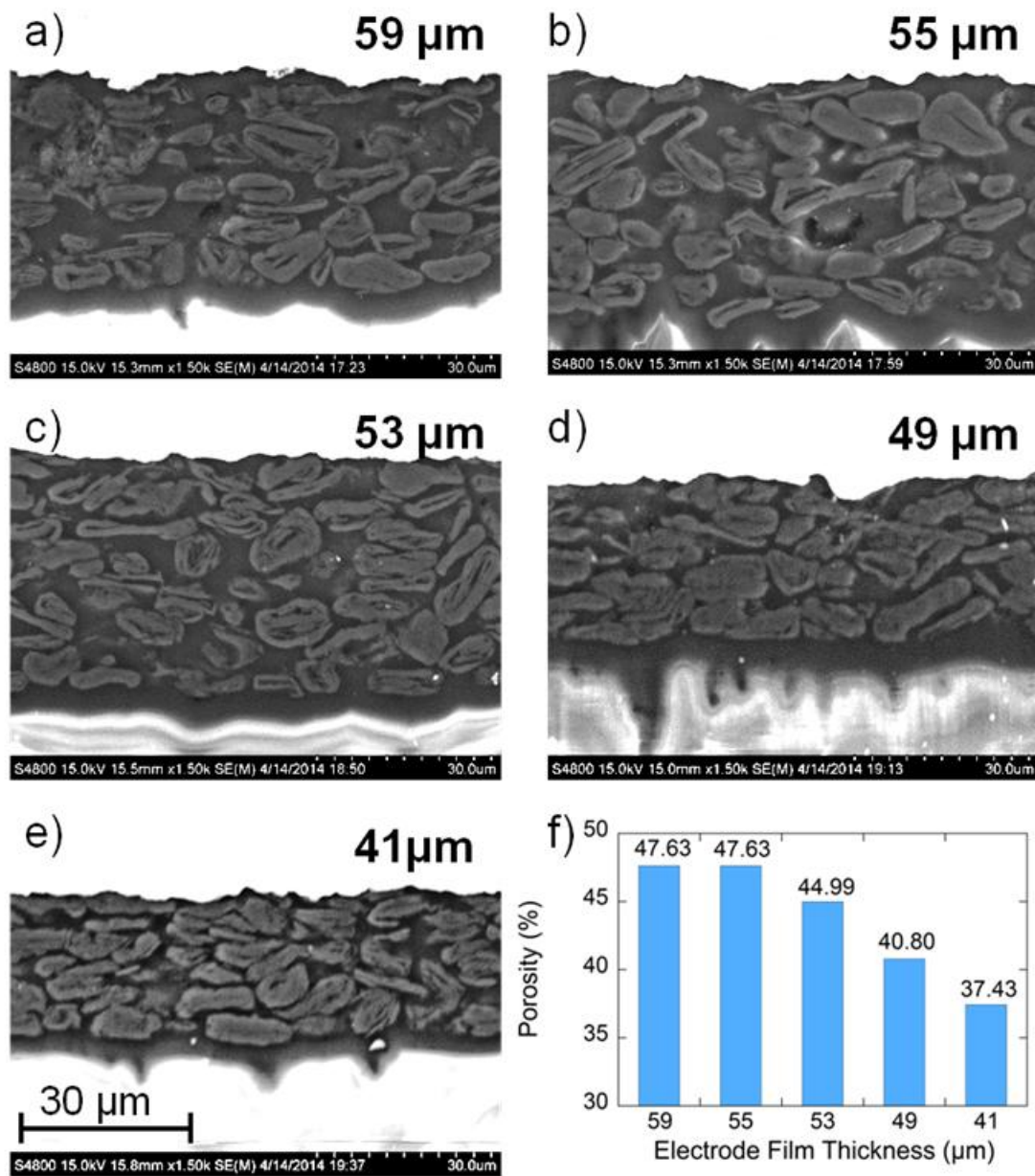


Figure 3-4 Cross-sectional backscattered electron (BSE) SEM images of graphite anode electrodes films. a), b), c), d), e) are for 59μm, 55μm, 53μm, 49μm, 41μm, respectively. f) Porosity for each film as measured by MIP.

Normalized cumulative intrusion curves from MIP tests, shown in Figure 3-5, were obtained by dividing the cumulative intrusion volume with the total intrusion volume for each respective sample. The intrusion process begins with mercury filling pores that have the largest diameters and proceeds to pores of continually decreasing diameter with increasing applied pressure [32].

The intrusion rate is much slower in the large pore region. When a pore size smaller than a threshold pore diameter (d_{th}) is achieved by increasing the applied pressure, further intrusion occurs rapidly by filling the nearby smaller pores [32, 33]. The fastest intrusion rate occurs when the pore diameter decreases to a critical pore diameter (d_{cr}) value which is also the diameter for the smallest connecting pore throat. The region showing a steep increase of the intrusion volume can be related to a connected pore network at that particular pore size. In the normalized intrusion curve, this connected porosity region is also the ratio of connected pore volume to total pore volume or the percent of total porosity. As seen in Figure 3-6, differentiated curves are used to indicate these parameters of critical, threshold, and connecting pore sizes. For the differentiated curves, intrusion events are identified by peaks that cover certain pore sizes. The threshold diameter (d_{th}) is found at the initial start of a peak (reading from high pore size to low) and the critical diameter (d_{cr}) as the pore diameter at the apex of the peak. Detailed pore size information from the normalized intrusion curves are summarized in Table 3-3. Each peak in the differentiated curve is characterized by its relative d_{cr} , and d_{th} . Those values then describe intrusion events occurring over specific pore sizes. Additional random pore filling also occurs which accounts for the remainder of the total pore volume.

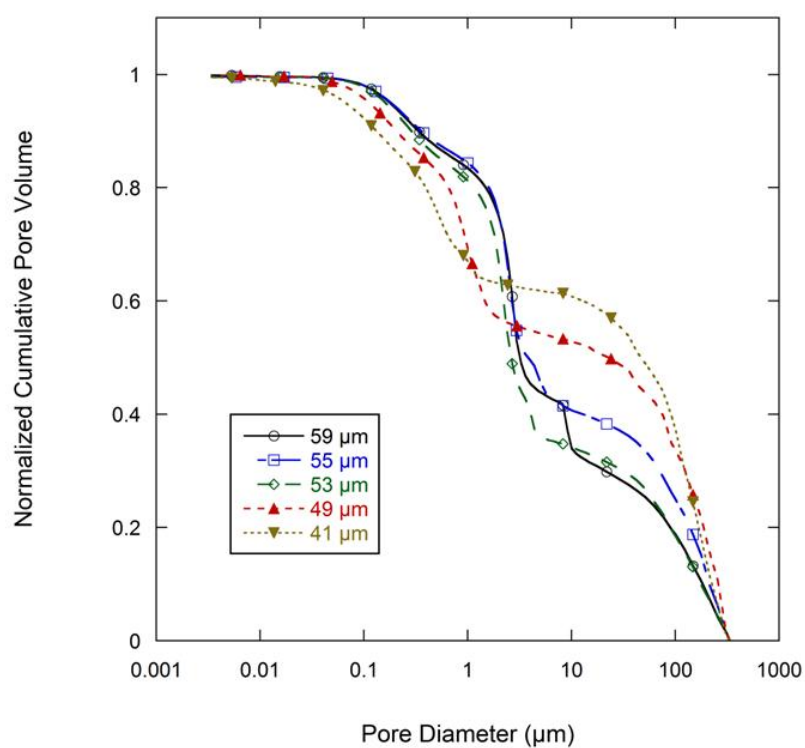


Figure 3-5 Slope of normalized cumulative intrusion curve for all graphite anode electrodes films.

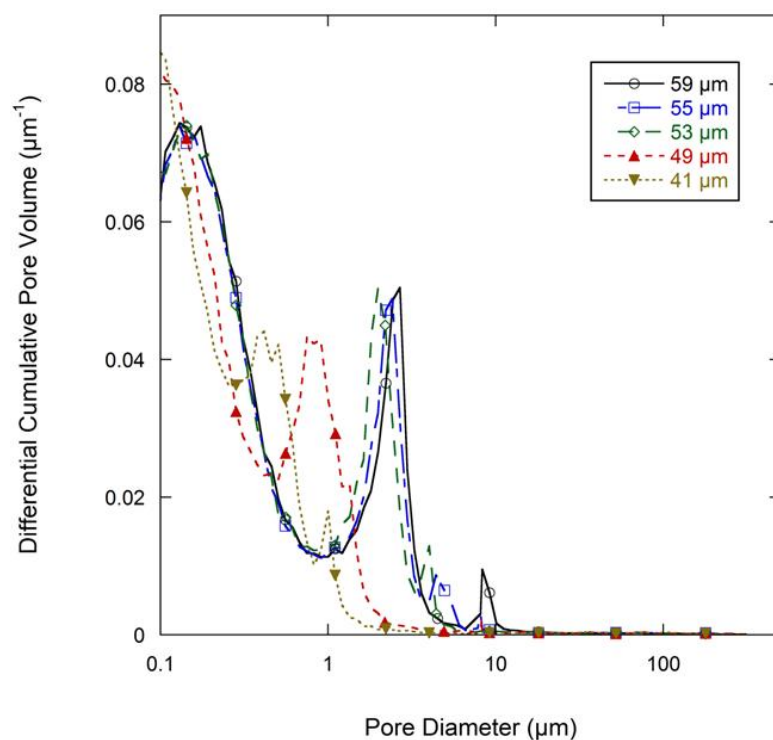


Figure 3-6 Differential pore volume of normalized cumulative intrusion curve (from Figure 5) for all graphite anode electrodes films.

Table 3-3 Data summary of results from wetting balance test for all the electrode films.

Anode films	59μm		55μm			53μm		49μm				41μm		
Pore networks	<i>I</i>	<i>II</i>	<i>I</i>		<i>II</i>	<i>I</i>	<i>II</i>	<i>I</i>		<i>II</i>		<i>I</i>	<i>II</i>	
Peaks	st ₁	nd ₂	st ₁	nd ₂	rd ₃	st ₁	nd ₂	st ₁	nd ₂	rd ₃	th ₄	st ₁	nd ₂	rd ₃
<i>d_{cr}</i> (μm)	8.31	2.68	8.31	4.40	2.42	4.02	1.99	8.21	1.34	0.91	0.75	1.00	0.51	0.42
<i>d_{th}</i> (μm)	10.10	4.01	8.33	6.65	3.61	4.90	3.30	8.31	2.18	1.21	0.82	1.34	0.83	0.46
Vol %	8.0	41.0	0.4	6.7	32.5	7.5	38.1	0.4	9.3	18.0		5.0	16.0	
Total Vol % (networks <i>II</i> and <i>I</i> combined)	49.0		39.6			45.6		27.7				21.0		

As summarized in Table 3-3, there are two main levels of pore networks in the electrode films, denoted as network *I* and network *II*. Starting with the as-coated 59 μm film, network *I* accounts for 8.0% of the total pore volume, with a critical pore size (d_{cr}) of 8.31 μm and threshold diameter (d_{th}) of 10.10 μm . Network *II* accounts for 41.0% of the total pore volume, with d_{cr} of 2.68 μm , and d_{th} of 4.01 μm . With additional calendaring, the networks are continually compressed to have smaller d_{cr} and d_{th} . The d_{th} and d_{cr} appear to develop independently. The largest pore sizes (8 μm range) are nearly eliminated upon initial calendaring with only 0.4 vol% porosity remaining in that size range for Network *I*.

The change of the pore structures as a function of calendaring is shown in Figure 3-7. In Network *I*, the threshold diameter decreased rapidly from the as-coated thickness of 59 μm to 49 μm and then leveled off with further calendaring down to 41 μm . The trend for the critical diameter was similar except in the range of 55 μm to 53 μm , in which d_{cr} has only a slight decrease from 4.40 μm to 4.02 μm . In Network *II*, both d_{cr} and d_{th} decrease slowly from the as-coated thickness down to 53 μm . The most dramatic change in the size of the network *II* occurs between 53 and 49 microns after which the network *II* size remains somewhat stable. The ratio of d_{cr}/d_{th} , which can be consider as the uniformity of the ducts, is shown in the secondary axis of the Figure 3-7 and shows no discernible trend as a function of calendaring.

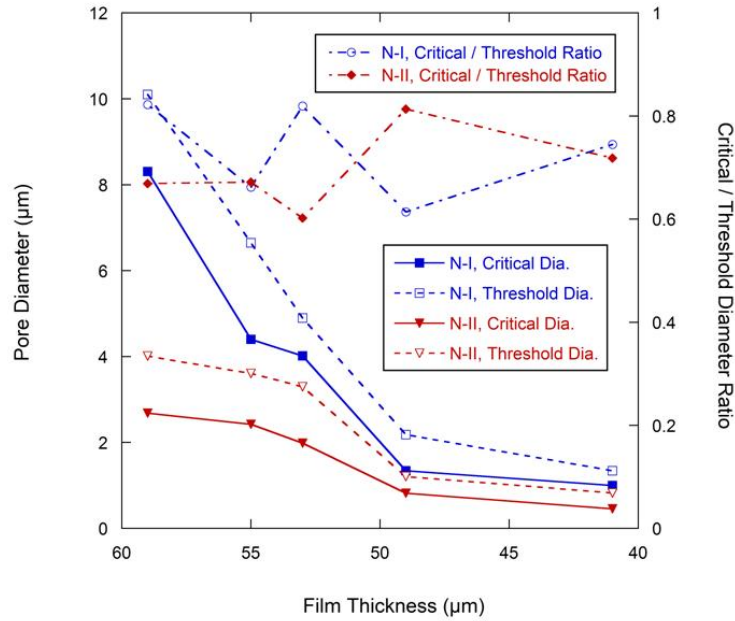


Figure 3-7 Pore diameter change with calendaring force (Primary axis), ratio of d_{cr}/d_{th} change with calendaring forces (secondary axis).

The pore size data were normalized to the as-coated 59μm film thickness, as shown in Figure 3-8a, and plotted along with the film thickness ratio from calendaring. The overall pore size ratio decreased more rapidly than the film thickness ratio. The critical diameter (d_{cr}) for Network *I* had rapid decreases between the as-coated condition and the film calendared to 55 μm and again between the 53 and 49 μm films. Other regions for the critical diameter in Network *I* followed similar trends as the film thickness ratio. The threshold diameter (d_{th}) for Network *I* decreased at a rapid rate from the as-coated thickness to the 49 μm level after which it generally followed the film thickness ratio. Network *II* showed a different behavior than Network *I* with a rapid decrease of the d_{cr} between the 55 and 49 μm thicknesses. Both pore networks tended to track with the film thickness ratio at calendaring thicknesses below 49 μm.

There are two types of movement of elliptical graphite particles when the calendaring force is applied, as shown in Figure 3-8b. One is compressive movement where the graphite particles will move closer to the particles above and below as they become more aligned to the calendaring direction. The other is a slipping movement where the nearby graphite particles will move parallel to each other which may reduce alignment. During calendaring, both movements will happen. This would result in a complex development of pore structure which may account for the lack of a discernible trend in d_{cr}/d_{th} as shown in Figure 3-7. The electrolyte transport inside the porous electrode film can be considered as two parts, converging-diverging in the junction of cavities and capillary flow in the throat [31, 34]. The latter can be quantified according to the Lucas-Washburn equation. Converging and diverging are generally affected by the cavity size and threshold diameter. A schematic diagram of one directional electrolyte transport process is shown in Figure 3-9. Figure 3-9a is a simplified description of the pore network, α and β are two kinds of cavities in two dimensions which are created by 4 and 3 nearby graphite particles, respectively. The α cavity is connected by 4 throats, and β cavity is connected by 3 throats. When electrolyte is inputted through the left side, it will fill cavity α first by transporting through the throat, as shown in Figure 3-9b. This is the converging process during the electrolyte filling. After filling the cavity, electrolyte may transport along the throats in the other three directions equally. This is the diverging process. To simplify the situation, only one direction is considered here. As indicated in Figure 3-9c, after filling the cavity β , electrolyte may also transport along throats in other directions. The electrode pore structure can be described as a series of α - α , β - β , or α - β connected pores where larger fractions of the α - α type will tend to increase connectivity between the cavities.

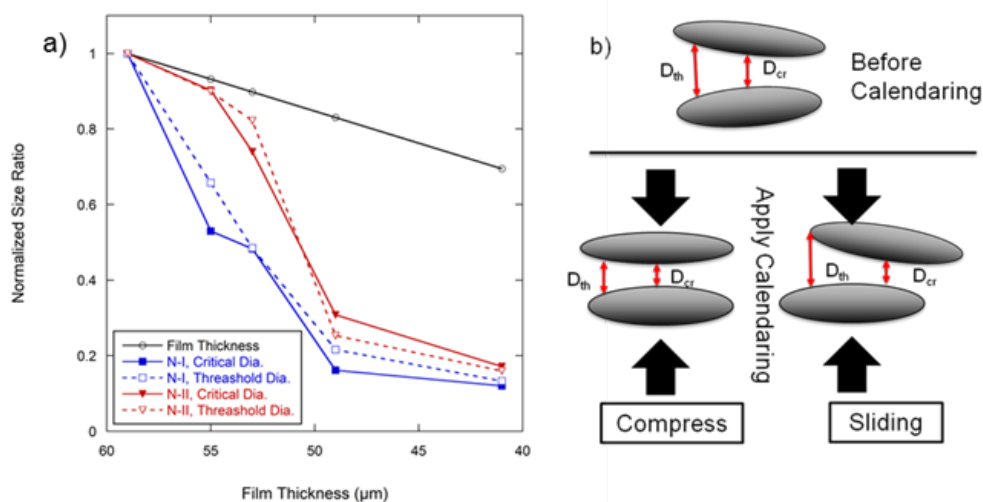


Figure 3-8 a) Pore size ratio of calendared films to pore size in 59 μm baseline anode films, and film thickness change with calendaring force. b) Schematic showing the pore size and geometry change with calendaring force in graphite anode films.

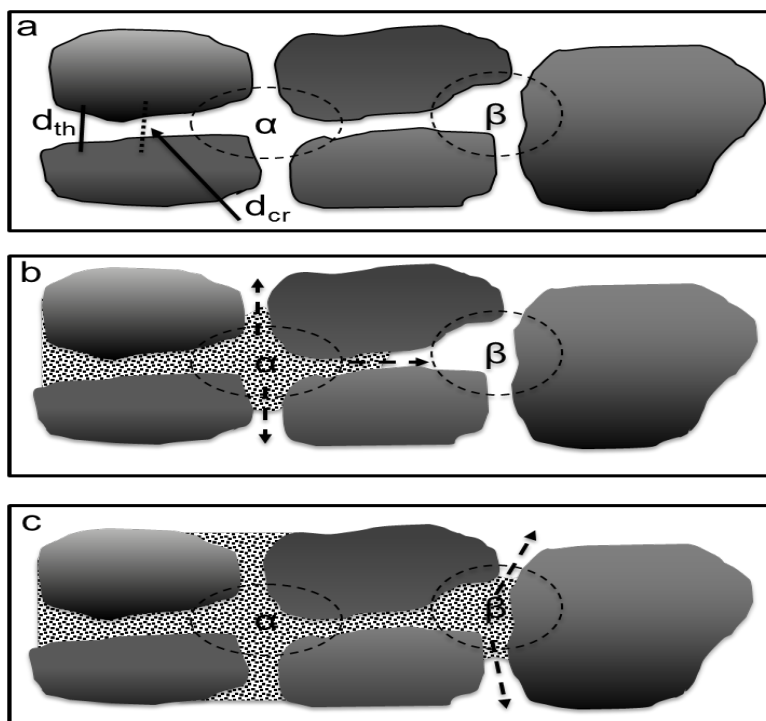


Figure 3-9 Scheme for electrolyte transport process in the porous medium.

Both the SEM images and the MIP results show that the cavity size inside the electrode film decreases with calendaring from 59 μm to 41 μm . The smaller cavity sizes would decrease the total

amount of electrolyte converging into the cavities and act to increase the wetting rate. The SEM images also show that the inter-particle spacing is decreasing as a function of calendaring. In terms of wetting, the inter-particle spacing is related to both the threshold diameter and the critical diameter. The combined impact of converging (based on cavity size) and diverging (based on d_{cr} and d_{th}) effects will determine the overall wetting rates of the film. As the film is initially calendared, the converging effects are acting to increase wetting rates (via smaller cavities) while the diverging effects are complicated by the combined effects of d_{cr} , d_{th} and the volume fraction of the pore networks. When the threshold diameter rate of decrease is larger than that of critical diameter rate, the pore throat is opened away from the cavities and the wetting rate in the throat will increase. When the threshold diameter rate of decrease is slower than that of the critical diameter, the pore throat opens towards the cavities which lowers the wetting rate. Networks with a larger volume fraction will tend to dominate networks of lower volume fraction.

The pore size, normalized to the 59 μm baseline film thickness in Figure 3-8a, is a good indicator for the change of relative pore diameters and can help explain the converging-diverging properties and overall wetting behavior of the film. From 59 to 55 μm in Network *I*, the slope of threshold diameter is smaller than the critical diameter so the diverging process is increased. In Network *II* for the same film thicknesses, the slope is the same for both diameters so no diverging improvement occurred in that network. As a sum, the total wetting rate should increase with the modest overall increase in pore divergence, which matches our wetting balance test result. From 55 to 53 μm , the slope of the threshold diameter is steeper than the critical diameter in Network *I* so the diverging process has a slight decrease. In Network *II* for the same film thickness range, the slope of threshold diameter is smaller than the critical diameter so the diverging effect is increasing. The impact of Network *I* in this case is lower than Network *II* because the volume percent of

Network *I* (7.5%) is much lower than that for Network *II* (38.1%). The slight decrease of divergence in Network *I* is overshadowed by increased divergence in Network *II*. The combined effects of Networks *I* and *II* again provide for an increase in wetting rate in spite of the decrease in overall film porosity. In the wetting balance result, wetting rate reaches a maximum value at the 53 μm film thickness. From 53 to 49 μm , the slope of threshold diameter change is steeper than the critical diameter in Network *II* so divergence is reduced. In Network *I*, the slope of the threshold diameter is smaller than the critical diameter so the diverging process is increased. Considering the volume fraction of each network, 9.3% for Network *I*, and 18.0% for Network *II*, the total diverging process should be reduced as the larger pore volume of Network *II* will dominate. This matches with the observed reduction in wetting rates between the 53 and 49 μm films. From 49 to 41 μm , the pore size ratio slopes for the critical and threshold diameters are almost the same as the film thickness decrease ratio. In this region, the pore network becomes more uniform with less cavity/throat structure and the wetting rates become increasingly dependent on capillary forces dictated by the inter-particle spacing.

The effects of converging-diverging features may not be obvious from SEM characterization or reliance on simple porosity comparisons. The wetting behavior of the as-coated and lightly calendared films appears to be based on the cavity structure and the evolving pore networks where the convergence / divergence mechanism dominates. Beyond a certain level of calendaring, the convergence / divergence mechanism is less obvious and the wetting becomes dominated by the capillary forces inside the pore network. This may account for the initial increase in observed wetting rates with light calendaring followed by a decrease in wetting rates at larger amounts of calendaring. Initial calendaring modifies the convergence / divergence in a way that improves electrolyte wetting even with a decrease in overall porosity of the film. Excessive calendaring

results in a pore structure dominated by capillary forces where lower porosity and smaller pore diameter limits the wettability of the film.

3.4 Conclusion

The wettability of graphite anode films as a function of the calendaring process was investigated and related to the development of the pore structure in the electrode films. Modest calendaring was shown to improve the wetting rate of anode films due to the alignment of particles and the increase in divergence within the pore networks. Calendaring beyond an ideal level decreased wetting rates due to reductions in porosity and average pore diameter. A combination of convergence-divergence flow and capillary flow mechanisms determine the wetting rate of the film. Convergence-divergence dominates in the as-coated and lightly calendared conditions while capillary flow dominates at higher levels of calendaring. Wetting rates generally follow the Washburn predictions as a function of pore size and porosity levels though deviations from ideal behavior were observed that indicate that the effective pore diameter used in that equation may be inadequate in describing the pore network of the electrode film.

References

1. Tarascon, J-M., and Michel Armand. (2001). Issues and challenges facing rechargeable lithium batteries. *Nature*, 414, 359-367.
2. García, R. Edwin, and Yet-Ming Chiang. (2007). Spatially resolved modeling of microstructurally complex battery architectures. *Journal of The Electrochemical Society*, 154, A856-A864.
3. Vu, Anh, Yuqiang Qian, and Andreas Stein. (2012). Porous Electrode Materials for Lithium - Ion Batteries—How to Prepare Them and What Makes Them Special. *Advanced Energy Materials*, 2, 1056-1085.
4. Ramadesigan, Venkatasailanathan, et al. (2012). Modeling and simulation of lithium-ion batteries from a systems engineering perspective. *Journal of The Electrochemical Society*, 159(3), R31-R45.
5. Scrosati, Bruno, and Jürgen Garche. (2010). Lithium batteries: Status, prospects and future. *Journal of Power Sources*, 195(9), 2419-2430.
6. Dillon, Shen J., and Ke Sun. (2012). Microstructural design considerations for Li-ion battery systems. *Current Opinion in Solid State and Materials Science*, 16(4), 153-162.
7. Hautier, Geoffroy, et al. (2011). Novel mixed polyanions lithium-ion battery cathode materials predicted by high-throughput ab initio computations. *Journal of Materials Chemistry*, 21(43), 17147-17153.
8. Mueller, Tim, et al. (2011). Evaluation of favorite-structured cathode materials for lithium-ion batteries using high-throughput computing. *Chemistry of materials*, 23(17), 3854-3862.
9. Yoshio, M., R. J. Brodd, and Akiya Kozawa. (2009). *Lithium-Ion Batteries: Science and Technologies*. Springer.
10. Guy, D., et al. (2006). Critical role of polymeric binders on the electronic transport properties of composites electrode. *Journal of The Electrochemical Society*, 153(4), A679-A688.
11. Thorat, Indrajeet V., et al. (2011). Understanding rate-limiting mechanisms in LiFePO₄ cathodes for Li-ion batteries. *Journal of The Electrochemical Society*, 158(11), A1185-A1193.
12. Park, Jung-Ki, ed. (2012). *Principles and applications of lithium secondary batteries*. John Wiley & Sons.
13. Bae, Chang-jun, et al. (2013). Design of Battery Electrodes with Dual - Scale Porosity to Minimize Tortuosity and Maximize Performance. *Advanced Materials*, 25(9), 1254-1258.
14. Zhang, Sheng Shui. (2006). A review on electrolyte additives for lithium-ion batteries. *Journal of Power Sources*, 162(2), 1379-1394.
15. Song, J. Y., Y. Y. Wang, and C. C. Wan. (2000). Conductivity study of porous plasticized polymer electrolytes based on poly (vinylidene fluoride) a comparison with polypropylene separators. *Journal of The Electrochemical Society*, 147(9), 3219-3225.

16. Wu, Mao-Sung, et al. (2004). Assessment of the wettability of porous electrodes for lithium-ion batteries. *Journal of applied electrochemistry*, 34(8), 797-805.
17. Kühnel, Ruben-Simon, et al. (2013). Evaluation of the wetting time of porous electrodes in electrolytic solutions containing ionic liquid. *Journal of Applied Electrochemistry*, 43(7), 697-704.
18. Ebner, Martin, et al. (2014). Tortuosity Anisotropy in Lithium-Ion Battery Electrodes. *Advanced Energy Materials*, 4(5).
19. Wang, Ming, et al. (2012). The effect of local current density on electrode design for lithium-ion batteries. *Journal of Power Sources*, 207, 127-133.
20. Jannesari, H., M. D. Emami, and C. Ziegler. (2011). Effect of electrolyte transport properties and variations in the morphological parameters on the variation of side reaction rate across the anode electrode and the aging of lithium ion batteries. *Journal of Power Sources*, 196(22), 9654-9664.
21. Lee, Shung-Ik, Yun-Sung Kim, and Hai-Soo Chun. (2002). Modeling on lithium insertion of porous carbon electrodes. *Electrochimica acta*, 47(7), 1055-1067.
22. Sawai, Keijiro, and Tsutomu Ohzuku. (2003). Factors affecting rate capability of graphite electrodes for lithium-ion batteries. *Journal of the Electrochemical Society*, 150(6), A674-A678.
23. Nelson, P. A., K. G. Bloom, and D. W. I Dees. (2011) Modeling the performance and cost of lithium-ion batteries for electric-drive vehicles. No. ANL-11/32. *Argonne National Laboratory (ANL), Argonne, IL (United States)*.
24. Klett, Matilda, et al. (2012). Quantifying mass transport during polarization in a Li Ion battery electrolyte by in situ ⁷Li NMR imaging. *Journal of the American Chemical Society*, 134(36), 14654-14657.
25. Arora, Pankaj, Marc Doyle, and Ralph E. White. (1999). Mathematical Modeling of the Lithium Deposition Overcharge Reaction in Lithium - Ion Batteries Using Carbon - Based Negative Electrodes. *Journal of The Electrochemical Society*, 146(10), 3543-3553.
26. Shim, Joongpyo, and Kathryn A. Striebel. (2003). Effect of electrode density on cycle performance and irreversible capacity loss for natural graphite anode in lithium-ion batteries. *Journal of power sources*, 119, 934-937.
27. Xiao, Yan, Fuzheng Yang, and Ranga Pitchumani. (2006). A generalized analysis of capillary flows in channels. *Journal of colloid and interface science*, 298(2), 880-888.
28. Washburn, Edward W. (1921). The dynamics of capillary flow. *Physical review*, 17(3), 273.
29. Alava, Mikko, Martin Dubé, and Martin Rost. (2004). Imbibition in disordered media. *Advances in Physics*, 53(2), 83-175.
30. Cai, Jianchao, and Boming Yu. (2011). A discussion of the effect of tortuosity on the capillary imbibition in porous media. *Transport in porous media*, 89(2), 251-263.
31. Durst, F., R. Haas, and W. Interthal. (1987). The nature of flows through porous media. *Journal of Non-Newtonian Fluid Mechanics*, 22(2), 169-189.

32. Aligizaki, Kalliopi K. (2005). *Pore structure of cement-based materials: testing, interpretation and requirements*. CRC Press.
33. Kaufmann, Josef, Roman Loser, and Andreas Leemann. (2009). Analysis of cement-bonded materials by multi-cycle mercury intrusion and nitrogen sorption. *Journal of colloid and interface science*, 336(2), 730-737.
34. Sochi, Taha. (2010). Flow of non-newtonian fluids in porous media. *Journal of Polymer Science Part B: Polymer Physics*, 48(23), 2437-2767.

CHAPTER 4 Electrolyte wetting of anode electrode with pore structures changed by binder/carbon black ratio

4.1 Introduction

It has been clear that the development of battery manufacturing process is as important as the pursuit of new electrode material. [1] The electrodes and separator sheet can be considered as dedicated porous structures with pore size range from near nanometer to tens of micrometer. The ionic transport happens in these pores and supports the faradic electrochemical reaction for electrochemical charging and discharging [2, 3]. The pore microstructure of the electrode film can be highly modified through the electrode preparation processes [4, 5], which include slurry making, coating, drying and some postproduction processes (slit, calendering, rolling etc.). In the manufacturing of lithium ion battery, electrolyte wetting occurs during the electrolyte injection, formation and aging processes [6], which are after electrode preparation and cell assembly. Compared with its important influence in lithium ion battery, the investigation about the electrolyte wetting has been well developed. Effects of post-production method (calendering) on the electrolyte wetting have been demonstrated[7]. The evolution of pore structure during the calendering process could be used to modify the electrolyte wetting. From another point of view, it indicates the possibility of optimizing the wetting performance by controlling the production processes, which can not only modify but also determine the formation of novel pore structures.

The pore structure of electrode film is initially determined by the composition of its components, such as active materials (graphite, NMC, LTO, LiFePO₄ etc.), binder (PVDF, CMC, PAA etc.), conductive additives (carbon black, carbon nanotube and graphene etc.), and slurry solvent (mainly NMP and water). The binder is used to adhere the active material and conductive additive to ensure

a porous medium network with good electrical conductivity and mechanical strength during the battery charging and discharging [8]. The optimization of the rheological process [9, 10], which is the interaction of these components in the slurry-making step [11], is critical to the battery manufacturing. This can be achieved mainly in two ways: increasing the dispersion of solid particles [12] and varying the viscosity of the slurry [11]. The interaction between polymer binder and solids, which could alter the fluid viscosity, is vital to achieve proper rheological performance. Moreover, the goal of the rheological process is to ensure good uniformity of the slurry and homogenous distribution of conductive additive on the surface of active material [13]. Currently, a large majority of conductive additives in application are different kinds of carbon black [14-16]. It exists as aggregate, which is composed by very small primary particles, and has strong tendency to form agglomerates. To achieve uniform slurry, it is necessary to avoid the initial carbon agglomerates in the preparation process [13, 17, 18]. Therefore, the carbon black could highly affect the rheological process and then the resulting pore structures.

To further investigate on the effect of production process on the electrolyte wetting, it is necessary to uncover the evolution of pore structure in the processes and the influence of pore structure on electrolyte wetting. Moreover, the mechanism of the pore structure evolution is very helpful to understand the electrochemical performance of lithium ion batteries[19, 20]. In this research, by increasing the carbon black amount, the effect resulting pore structure change on the wetting rate is investigated in the graphite/CMC+SBR aqueous system. The mixture of carboxymethyl cellulose (CMC) and styrene butadiene rubber (SBR) has been considered as the important environmental benign binder for next generation electrode manufacturing [21]. CMC is a linear polymeric derivative of cellulose, which is composed by β -linked glucopyranose residues with

varying levels of carboxymethyl ($-\text{CH}_2\text{COO}-$) substitution [22]. It has been widely used as thickener, binder and stabilizer in various industries [23, 24]. Although a binding network could be formed during the CMC polymerization, it is a brittle binder lacking elastic properties [25]. Therefore, elastomeric SBR is added to increase the flexibility of the electrode and adhesion between film and current collector [12, 21]. The CMC has more tendencies to be adsorbed on the surface of graphite than the SBR [26]. Due to the interaction between the solid particle and polymer, such as bridging, depleting attraction and electrostatic repulsion, a variety of pore structure could be formed [13, 27, 28]. Although depletion of binder in the bottom of electrode film could happen during the drying [12, 29], it is need to be noted that the structure determine processes, such as adsorption of polymer binder on the particle surface and formation of polymer-particle network, mostly happens in the slurry stage[13].

To maximize the pore structure change and therefore make the differences in the electrolyte wetting behavior detectable, excess amount of carbon black was added to the slurry. Based on the quantitative analysis of wetting rate, the effect of these small around-nanosize pores between and in the aggregates on he electrolyte wetting will be explored using wetting balance test. The pore structures of resulting electrodes film are investigated using mercury intrusion test and electron microscopy. The pore network theory will be used to analyze the resulting pore structure. The combined mechanism of capillary flow and converging-diverging process, which was discovered in previous research, will also be examined. Based on the morphology analysis from SEM images, the impact of excessive carbon black on the pore structure will be discussed considering the rheological interaction between binder and solid particles in the slurry.

4.2 Materials and methods

The materials used in the research are provided by courtesy of Johnson Controls, Inc. The anode electrode film was prepared by coating aqueous slurry on the copper foil by tape casting with doctoral blade. An aqueous solution of CMC and SBR mixture was stirred in an acoustic mixer first and then graphite powder were added to the solution. Later, carbon black was added and the excess amount of water was added to keep the target solid percentage. After coating, the film is room temperature dried. Three graphite anodes were prepared; the detailed composition can be referred in Table 4-1. The binder (CMC/SBR, 1:1) ratio was kept at 3wt%, and the ratio of carbon black was increased from 3wt% to 5wt% and 7wt%. The active graphite powder ratio was changed accordingly from 94wt%, 92wt% to 90wt%. During the coating, all the solution part of slurry was kept at 40wt%, and final film thickness was fixed at 29 μm for all the electrodes.

The electrolyte solution used for electrolyte wetting test was 3:7 (volumetric ratio) solution of EC: EMC with 1.2M LiPF_6 (all these chemicals come from BASF). The wetting rate is measured by wetting balance test under environment with high purity flowing argon. More details about the test can be found in previous chapter. SEM characterization was performed with Hitachi S-4800 FE-SEM. Mercury intrusion porosimetry tests were performed on a Micromeritics AutoPore IV9510.

Table 4-1 Summary of compositions for each sample, and ratios between components (all compared in weight)

Sample	Graphite	Binder	CB	Graphite/CB	Graphite/Binder	CB/Binder
3%CB	94%	3%	3%	31.3	31.3	1.0
5%CB	92%	3%	5%	18.4	30.7	1.7
7%CB	90%	3%	7%	12.9	30.0	2.3

4.3 Results and discussion

A total of 6 samples were tested for each electrode film condition to account for experimental and electrode film variations. The wetting balance and mercury intrusion results are summarized in Table 4-2. The Averaged curving fitting parameters (R^2) from the determination of the wetting rate were in the range of 0.884 to 0.917, which confirms the validity of the wetting balance test method. The wetting rate for 3%CB is $0.109\text{mm/s}^{0.5}$, with standard deviation 0.0270. Increasing the carbon black ratio to 5%, the wetting rate for 5%CB is decreased to $0.075\text{mm/s}^{0.5}$, with standard deviation 0.0088. It is surprised to find that, when adding carbon black further to 7%, the wetting rate for 7%CB is further increased to $0.127\text{mm/s}^{0.5}$, with standard deviation 0.0313. The excess amount of carbon black will definitely bring in more agglomerate, which is composed by aggregates, to the final pore microstructure. If these aggregates are acting as a blocker for electrolyte wetting, the wetting rate should keep decreasing with increasing amount of carbon black. The rebound of wetting rate for 7%CB indicate the function of carbon black in the electrolyte is not only a blocker. Error% as listed in Table 4-2 is defined as the Standard deviation divided by the average wetting rate. It is similar to the variation of test results and can be used to describe measurement stability. The error% is high at 24.7% for 3%CB and 7%CB, and lower at 11.76% for 5%CB. The measurement stability is not as good as the results in chapter 2, where it is 6.73% for graphite

anode. This can be due to the different coating method. Compared with pilot slot die coating in chapter 2, tape casting that has significant higher coating non-uniformity was used in this research.

Table 4-2 Data summary of results from wetting balance test and Pore data, porosity from MIP.

Samples	Average Wetting rate (mm/S ^{0.5})	Stdev	Error (%)	<i>n</i>	<i>R</i> ²	Average Pore diameter (μm)	Porosity (%)	<i>P</i> * <i>r</i> ^{0.5} (μm ^{0.5})
3%CB	0.109	0.0270	24.70	6	0.917	0.178	23.1	0.069
5%CB	0.075	0.0088	11.67	6	0.884	0.262	26.4	0.095
7%CB	0.127	0.0313	24.70	6	0.956	0.239	28.6	0.099

In a capillary flow, as described in the modified Lucas-Washburn equation, the wetting rate should be linear to $P*r^{0.5}$ (*P* for porosity, *r* for averaged pore radius) for one solution. The porosity and averaged pore diameter are measured with mercury intrusion porosimetry. The results are summarized in Table 4-2. The porosity increases with the carbon black amount, from 23.1% at 3%CB to 28.6% at 7%CB. When excess carbon black is added, it is expected to increase the total porosity due to the existence of aggregates and agglomerate. The pore diameter also increases with carbon black amount from 0.178 μm at 3%CB to 0.239 μm at 7%CB. The pores between the carbon black aggregates help increasing the average pore diameter. Due to the small pore shielding effect on the mercury intrusion, it needs to be noted that the porosity measured from MIP will be much smaller than the actual porosity when excessive carbon black is existing. To analyze the electrolyte wetting behavior, the data for wetting rate and $P*r^{0.5}$ are charted in Figure 4-1. It doesn't indicate the linear trend of a capillary flow, as shown in the Figure 4-1. In the previous research about the effect of calendaring on the electrolyte wetting, the converging and diverging effect could be

attributed to the deviation from linear behavior. Due to the non-linear relation of wetting rate to $P*r^{0.5}$, it is obvious that the converging and diverging effect is dominated in the electrolyte wetting behavior when excessive carbon black amount is added.

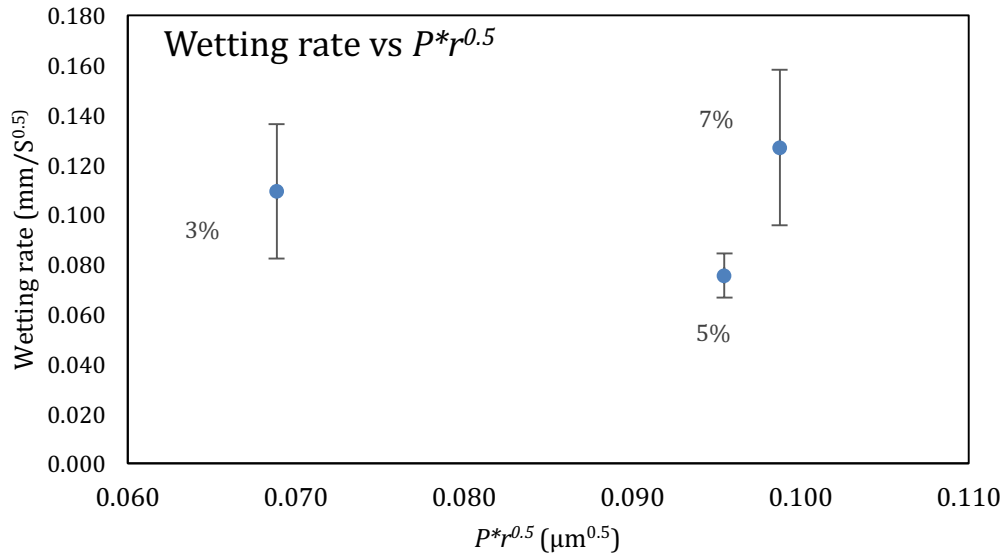


Figure 4-1 Trends of the wetting rate Vs $P*r^{0.5}$ for electrodes with different carbon black ratio.

The converging and diverging effect is highly related to pore structure of the electrode films, especially the pore cavities and pore throats. The electrolyte converges in the cavities first and then diverges into nearby pore throats, which can be related to the pore connectivity or pore networks. The pore network can be measured through the normalized intrusion curve of MIP, where the total volume is set as 1. The normalized intrusion and extrusion curves for different carbon black ratio are given in the Figure 4-2. The intrusion process begins with mercury filling pores that have the largest diameters and proceeds to pores of continually decreasing diameter with increasing the applied pressure. The intrusion rate is much slower in the large pore region. When a pore size smaller than a threshold pore diameter (d_{th}) is filled by increasing the applied pressure, further intrusion occurs rapidly by filling the nearby smaller pores [30]. The fastest intrusion rate occurs

when the pore diameter decreases to a critical pore diameter (d_{cr}), which is also the diameter for the smallest connecting pore throat[31]. The region showing a steep increase of the intrusion volume can be related to a connected pore network at that particular pore size. In the normalized intrusion curve, this connected porosity region is also the ratio of connected pore volume to total pore volume or the percentage of total porosity. In addition, the extrusion process is a reverse process of intrusion where the pressure is released. Due to the pore bottleneck effect, a part of mercury will be trapped in the pores, which is referred as the residual amount of total volume. It reflects the pore uniformity in certain levels.

As shown in the extrusion curves in the Figure 4-2, the entrapped mercury takes a majority part of total volume, which is highest for 7%CB with 74.5%, followed by 69.7% for 5%CB and smallest at 67.0% for 3%CB. The initial extrusion rates for 5%CB and 7%CB are similar and faster than that of 3%CB. Adding more carbon black results in increased pore non-uniformity in the electrode film.

The intrusion curves for pore size smaller than 0.8 μm are similar for all the samples, as shown in Figure 4-2. In the pore size range of 0.8 to 20 μm , the intrusion curves for increasing amount of carbon blacks are shifting towards right and upside, which are approaching bigger pore size and larger cumulative intrusion volume. The main part of steep increase in intrusion indicates that the connected part region for 3%CB electrode is about 43.1% of total volume. There is another small step separated from the main connected curve. This small step takes about 4.2% of total volume. It may act as a pore sub-network from the main pore networks since it's pore size is overlapping with pore size range of the main curve. And with the increase of carbon black, this pore sub-

network is shifting toward right and becoming more separating from the main curve. The percentage of this sub-network in the total pore volume is also increased to 4.5% for 5%CB, and 11.2% for 7%CB. The critical and threshold pore diameter are obtained from the differentiated curves, as shown in Figure 4-3. The threshold diameter (d_{th}) is found at the initial start of a peak (reading from high pore size to low) and the critical diameter (d_{cr}) as the pore diameter at the apex of the peak. The detailed pore size information from the normalized intrusion curves are summarized in Table 4-3. Each peak in the differentiated curve is characterized by its relative d_{cr} , and d_{th} . These values describe the intrusion events occurring over specific pore sizes. Additional random pore filling also occurs and accounts for the remainder of the total pore volume.

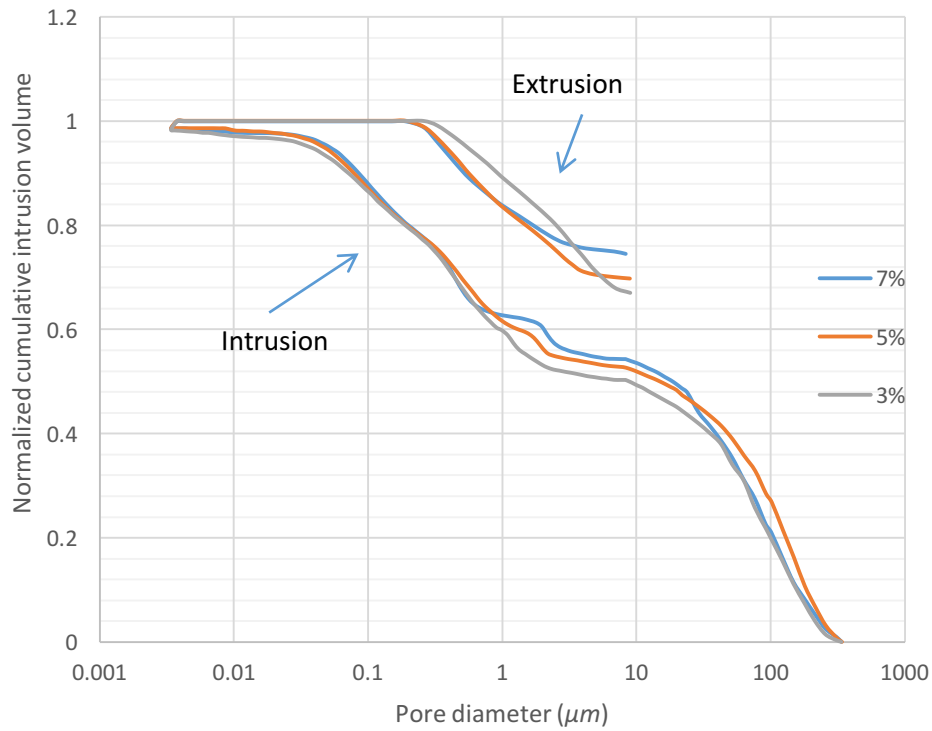


Figure 4-2 Normalized intrusion and extrusion curve for electrodes with different carbon black ratio.

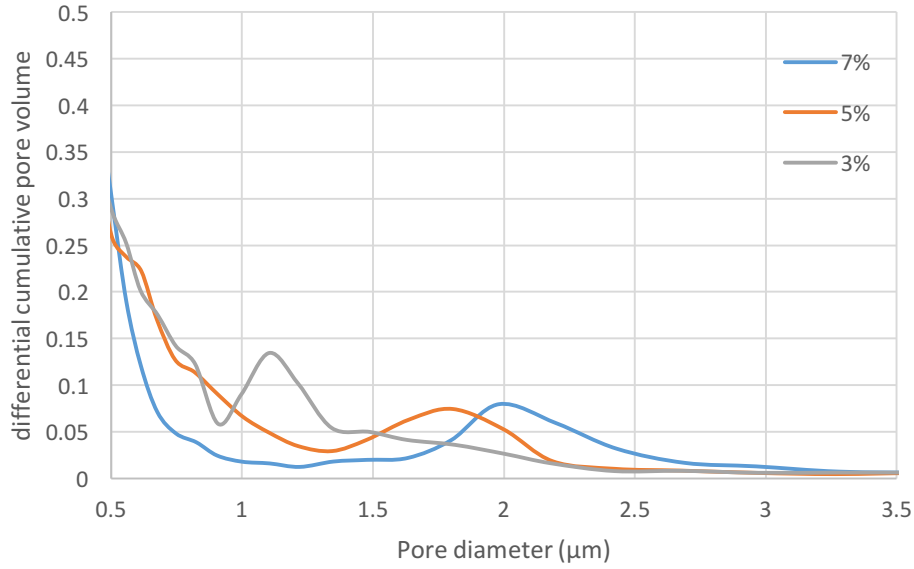


Figure 4-3, Differential pore volume of normalized intrusion curve (from Figure 4-2) for electrodes with different carbon black ratio (focusing Pore diameter in the range of 1-3 μm).

Table 4-3 Data summary for pore sub-network for all the electrodes.

Pore sizes for the pore sub-network			
Electrodes	3%CB	5%CB	7%CB
$d_{cr} (\mu m)$	1.10	1.81	1.98
$d_{th} (\mu m)$	1.34	2.19	2.69
$Vol\%$	4.2%	4.5%	11.2%

The wetting rate is greatly affected by the converging and diverging effect, as indicated in Figure 4-1. The converging effect is a process to store the electrolyte in the cavities from further transporting to other pores. The number of random pores (or less connected pores) in the range of 0.8 to 20 μm is increasing with increase of carbon black amount. An enhanced converging of electrolyte in cavities is expected. As a result, the electrolyte-wetting rate is limited by the

increasing amount of carbon black.

The diverging effect is a process when electrolyte leaving the cavity through pore throats and it is significantly affected by d_{cr} and d_{th} . The increase in diverging process in the pore throats would increase the wetting rate. The change of d_{cr} and d_{th} of different electrodes is charted in Figure 4-4. The inset of Figure 4-4 is a proportional representative change of d_{cr} and d_{th} in a pore throat for each sample, where the left side is the threshold diameter and the right side is the critical diameter. The diverging of electrolyte is expected to increase since the pore throats are getting larger from 3%CB, to 5%CB, and further to 7%CB. As a result, the wetting rate should be increased.

The wetting rate, as measured and shown in Figure 4-1, is decreasing from 3%CB to 5%CB, and then increase again and reach highest at 7%CB. As previously discussed, from 3%CB to 5%CB, the pore sub-network doesn't increase, but the percentage of pore cavity is increased. Therefore, the converging effect, which decreases the electrolyte wetting, is dominant; diverging processes, which increase the wetting rate, is not obvious. As a result, the wetting rate is dropping when the carbon black amount is increased to 5%CB. The sub-network, however, is increased from 4.5% to 11.2% at 7%CB. The diverging process becomes dominant over the converging in the cavity. As a result, the wetting rate is increased again at 7%.

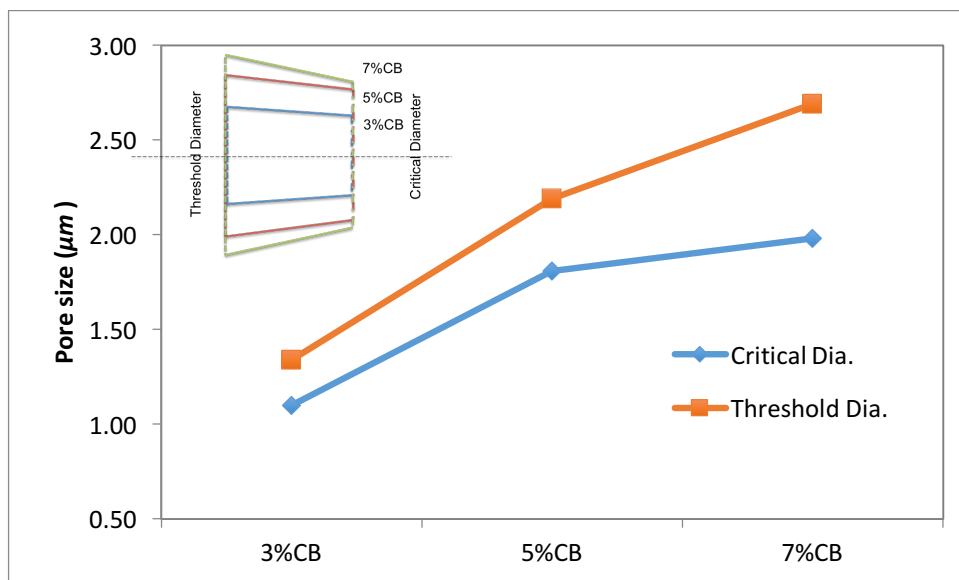


Figure 4-4 Pore diameter change of pore sub-network with different amount of carbon black.

Therefore, according to the mechanism of combined capillary and converging-diverging flow, the influence of pore microstructure evolution on the electrolyte wetting, which is analyzed by MIP, with different carbon black amount has been clarified. It has been found that the increment in pore cavity in 5%CB results in reduction in wetting rate, while the improvement of pore sub-network in 7%CB will boost it. In other aspect, the result is also supportive to previous calendering effect research where the mechanism of electrolyte wetting was tentatively discussed. However, the function of carbon black on the pore microstructure, especially the evolution of pore sub-network at 7%CB is still unclear. It will be helpful to understand some mechanical failure and non-uniformity in the electrode film coating. Investigation on the morphology of pore structures, especially the pore sub-network, will be discussed in the following section.

4.4 Evolution of pore microstructure in the electrodes

As stated in the introduction, the pore structure mainly formed during the slurry period when the

solid particle dispersion and the polymer network are established, and it is slightly changed during the drying process when the binder is redistributed by the solvent evaporation. The polymer binder is prone to interact with surface dangling bonds of particle, and form a 1 to 5 nm thick bound polymer layer through chemical bond or physical adsorption. This surface bound polymer layer is very stable and won't be dissolved by the solvent. Around the bound layer, an immobilized layer with thickness of 2-35nm could be formed. In this research, the CMC + SBR binder system is used. CMC is more competitive to adsorb on the surface of graphite than the SBR, and the adsorption of CMC will generate a good dispersion of the graphite particles in the slurry. The free CMC and SBR molecules will form a polymer network in the slurry among graphite particles. When the carbon black is added into the system, it will be dispersed by the free binder in the solvent, and be contacted with active material like graphite to form the conductive network. The drying process, based on different drying rate, can be divided into three stages, i) increasing drying rate of free surface solvent in the electrode film; ii), constant drying rate stage of the solvent between particles to be evaporated through capillary force; iii), decreasing drying rate stage of residual solvent vaped by diffusion. The binder redistribution only happens in the second constant dry rate stage, and the pore network is also mainly formed in this stage.

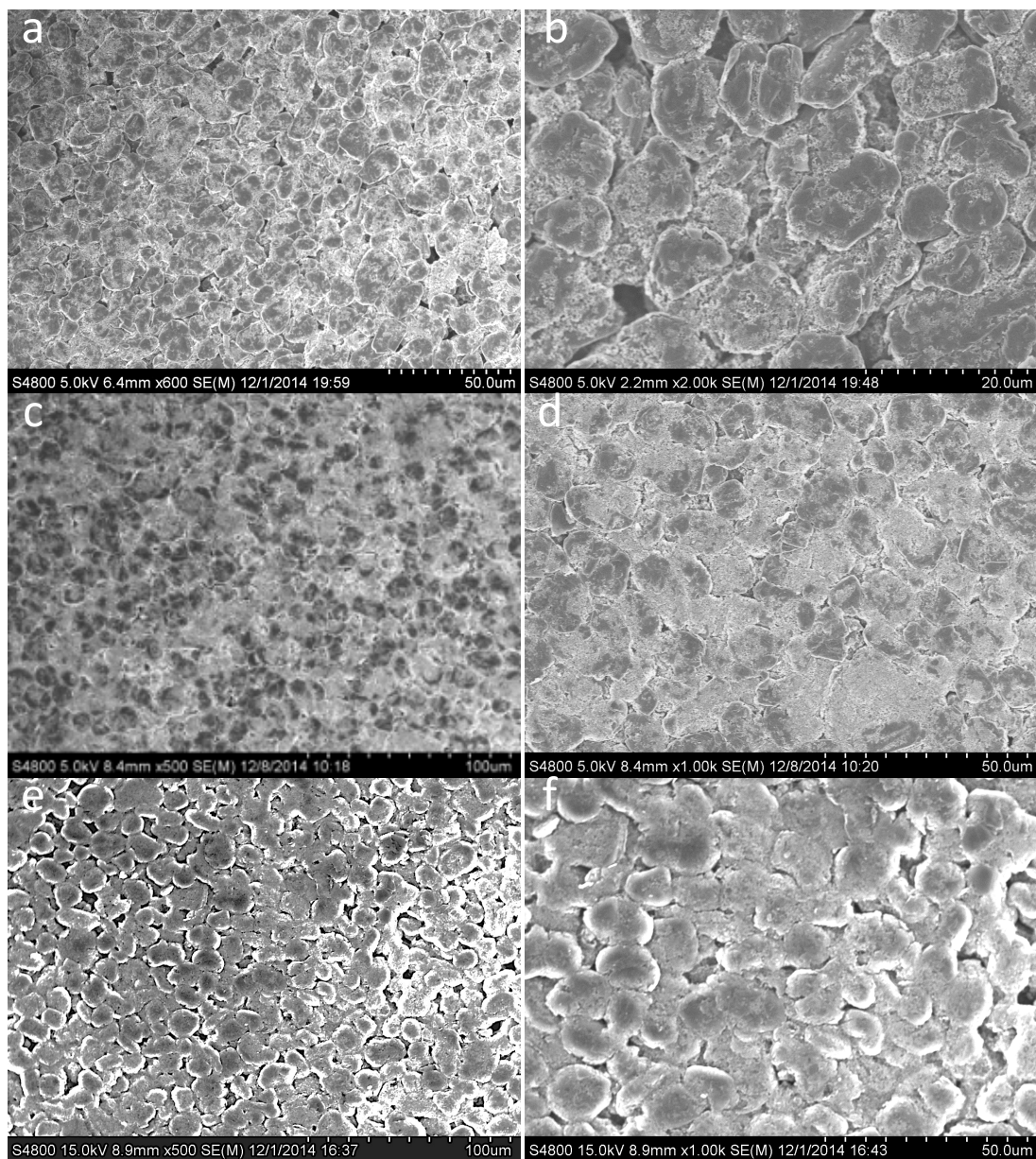


Figure 4-5 SEM pictures of different electrodes, a,b) 3%CB at 600X and 2000K, c,d) 5%CB, e,f) 7%CB with 500X and 1000X magnification.

As seen in Figure 4-5, a, c, e, the graphite particle disperses uniformly across the electrode film. With the increase of carbon black amount, the coverage on the graphite surface is also increased accordingly. And the void space between particles also become more filled by the carbon black from 3%CB to 7%CB, shown in Figure 4-5, b, d, f. Although there is more carbon black coverage

in 7%CB, the voids between graphite are still clear. In the higher magnification images, Figure 4-6, the typical features of the voids for different electrodes are shown. In 3%CB, the void is empty of carbon black. The carbon black is more filled in the void of 5%CB, and some micro-crack formed on the surface of graphite surface. The carbon black is highly agglomerated by small aggregates with a lot of small pores with size around micrometer among them. In 7%CB electrode, a second pore with diameter around 3 μm is formed in the filled carbon black domain, which is still similar and comparable to the CB domain in 5%CB. As a summary, the pore structure of different electrodes with increasing filling of carbon black in the void is evolved from micro crack in the interface and second pore in the carbon black domains.

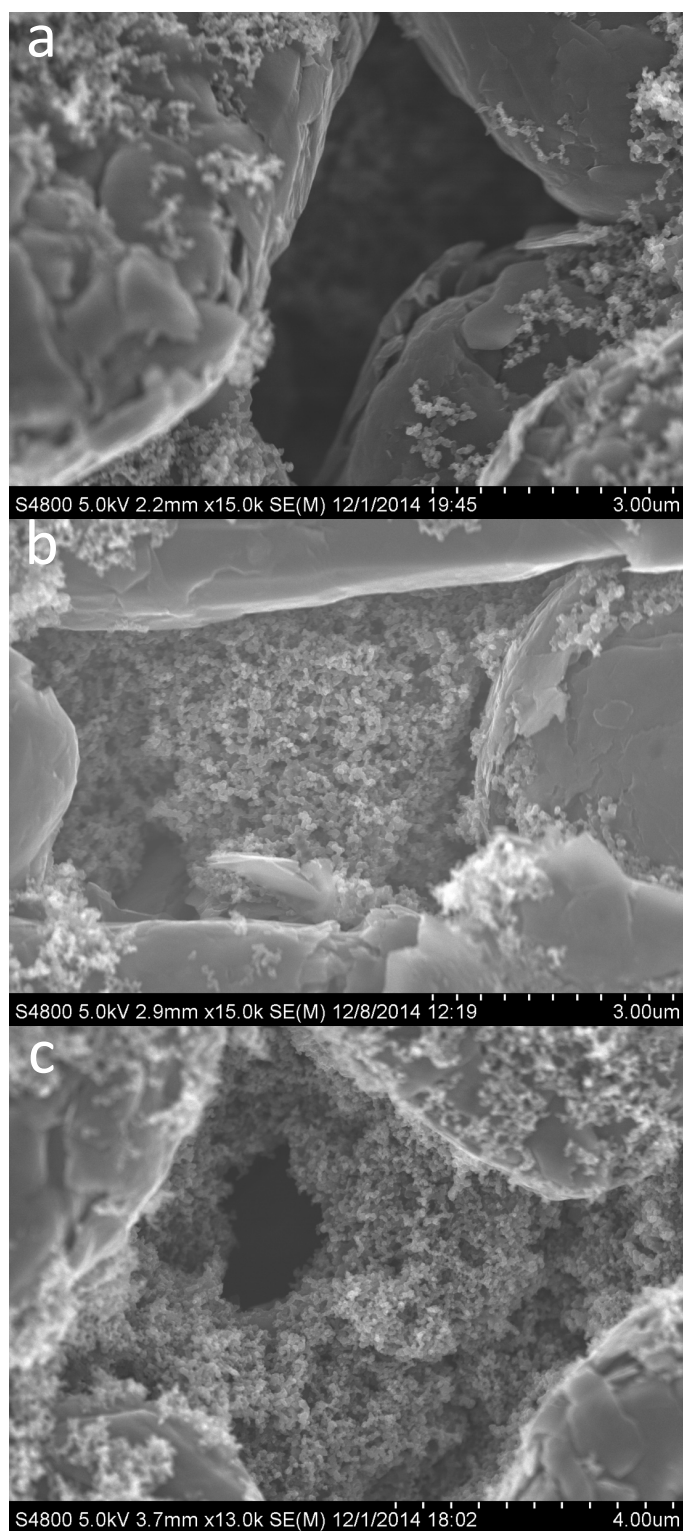


Figure 4-6 Typical void feature in different electrode film. a, bare pore wall in 3%CB, b, microcrack between CB domain and graphite 5%CB, c, a second pore formed in the CB domain in 7%CB.

More example of micro crack in 5%CB is given in Figure 4-7. The peeling off of carbon black domain from the graphite surface can be considered in two aspects. The first one is the position of the micro crack is in the interface. The second one is that some part of the micro crack is still connected, as clearly displaced in the Figure 4-7b and d. In Figure 4-7b, the carbon black is bound to the graphite in right side of the crack. And in Figure 4-7d, there is one spot in the crack that two parts of carbon black is still not connected. The crack is possible generated by the binder shrinkage during the drying process, since CMC can only sustain elongation to 5-6%. [32]

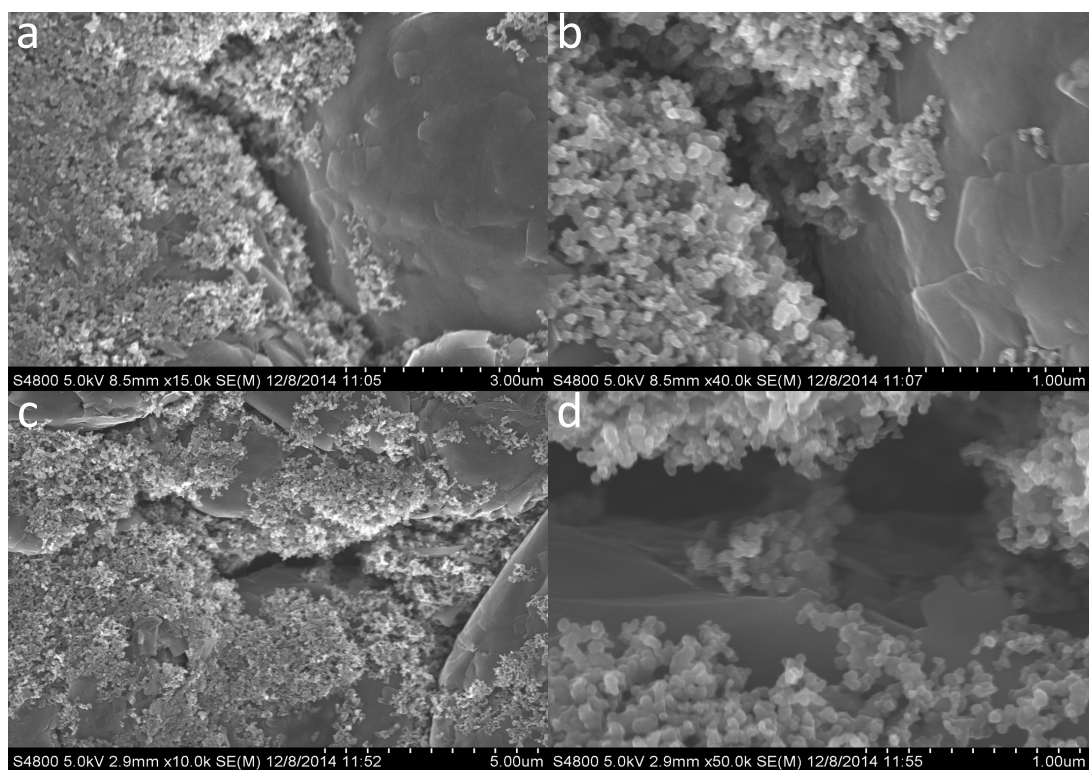


Figure 4-7 Some other examples of microcracks in 5%CB.

To clear the formation process of the second pores in the graphite void, a lot different spots of voids were investigated. One spot of void, which is still in the origin state of second pore formation,

is shown in Figure 4-8 with magnifications from 30k to 80k and to 250K. In Figure 4-8a, a small triangle shaped pore is found in the carbon black domain. It has not been fully developed yet. The upper side of the pore is widely separated, but the bottom side only has some slight cracks, where the small pores and particles are still connected. In the Figure 4-8c, the remained strings left from binder shrinkage are present between carbon black particles. Therefore, it is clear that the formation of the second pore in the void is also nucleated by the binder shrinkage. A small pore is generated first due to the binder shrinkage, then it connects with the its nearby small pores to generate a large second pore. It is possible that the second pore will be bigger when there are more small pores in the vicinity of initial small pores. When the carbon black amount is increased from 5% to 7%, the small pore in the carbon domain is also increased. Meanwhile, the binder distribution becomes more heterogeneous across the electrode since its total amount is kept the same. Therefore, the nucleation of small pore by binder shrinkage is surrender by more small pores in 7%CB electrodes. As a result, the second pore formed in 7%CB electrode and micro-crack formed in 5%CB electrode. The micro-crack is not through the whole CB domain, and it is only contributing to the total pore cavity increase. However, the second pores in 7%CB is bigger and through the void. Compared with 5%CB, therefore, the pores are more connected, as reflected in the MIP data where the sub-network is increased from 4.5% to 11.2%.

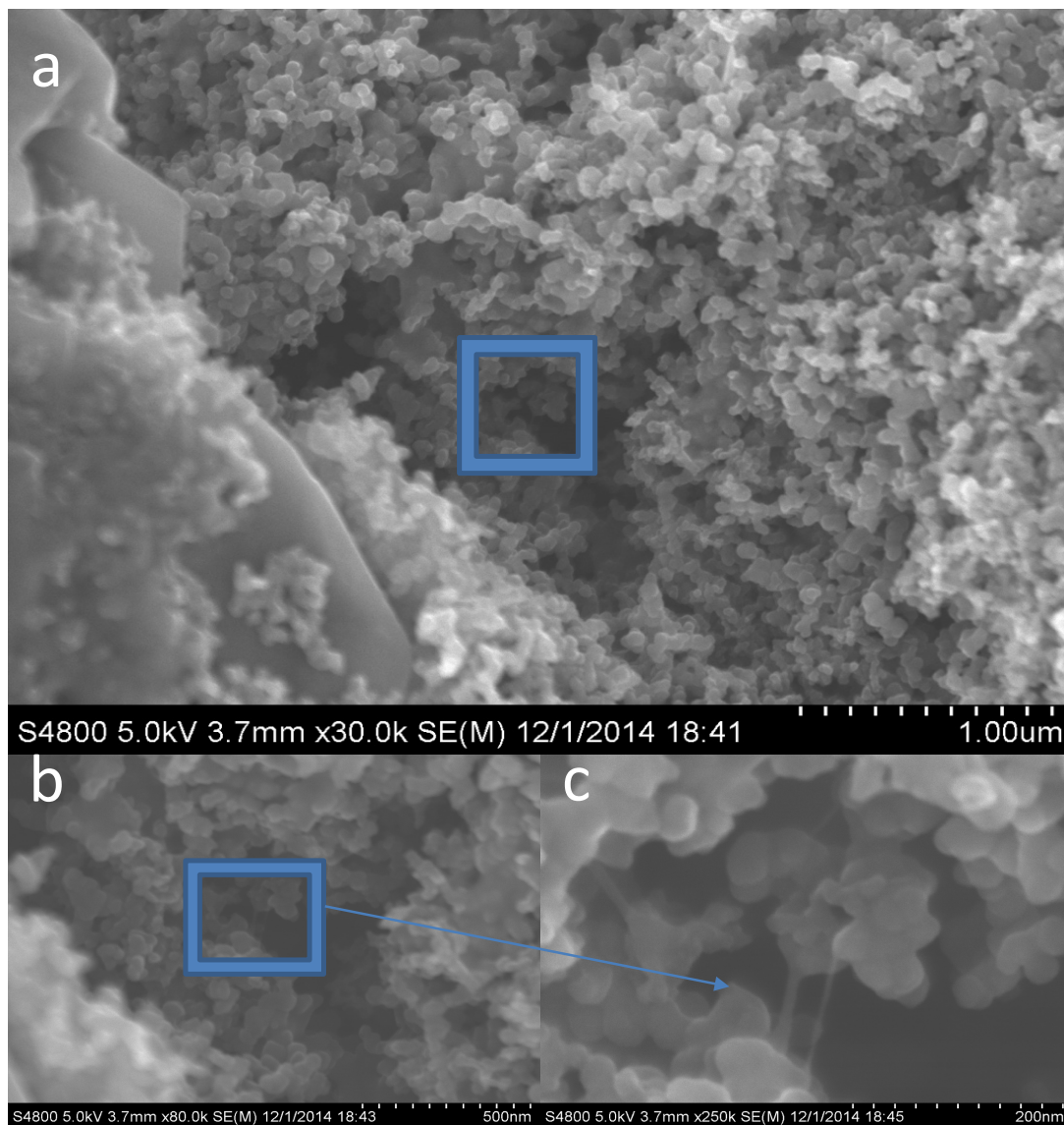


Figure 4-8 Evolution of second pore in the void in 7%CB electrode.

4.5 Conclusion

In this research, wetting rate change with pore structure evolution in the electrode film production stage is demonstrated with varying the amount of conductive additive (the carbon black). The effect of different amount of carbon black on electrolyte wetting of graphite anode electrode is found decreasing from 3%CB ($0.109 \text{ mm/s}^{0.5}$) to 5%CB ($0.075 \text{ mm/s}^{0.5}$), and bouncing back at

7%CB ($0.127 \text{ mm/s}^{0.5}$). The mechanism of combined capillary and converging-diverging flow is applied to analysis the trends of wetting rate. Based on the MIP and SEM analysis, the pore structure is highly affected by increasing the loading of carbon black. The pore cavity and pore sub-network are increasing with the higher loading of carbon black, as revealed by MIP curve. Based on the SEM image, the void is becoming more filled with carbon black domain, which is agglomerate of small carbon black aggregates. The pore structure of different electrodes with increasing filling of carbon black in the void is evolved from micro crack (5%CB) in the interface and second pore (7%CB) in the carbon black domains. The micro-crack is mainly contributing to the pore cavity increase in 5%CB, while the second pore in 7%CB help the increase of pore sub-network to 11.2%. The pore cavity increase in 5%CB results in higher converging of electrolyte, which decrease the wetting rate. Although the pore cavity amount is also increased in 7%CB, the diverging effect of the increased pore sub-network helps further increase the wetting rate.

The mechanism of combined flow of electrolyte wetting, which discovered in the research of calendering effect, is verified in this research. Understanding the cause of electrolyte wetting is fundamental to many other phenomena in the lithium ion battery. The effect of carbon black on the pore structure would be helpful for understanding some non-uniformity in the electrode film.

References

1. García, R.E., et al., Microstructural Modeling and Design of Rechargeable Lithium-Ion Batteries. *Journal of The Electrochemical Society*, 2005. 152(1): p. A255.
2. Newman, J. and K.E. Thomas-Alyea, *Electrochemical systems*. 2012: John Wiley & Sons.
3. Bazant, M.Z., *Theory of Chemical Kinetics and Charge Transfer based on Nonequilibrium Thermodynamics*. *Accounts of chemical research*, 2013. 56(5): p. 1144-1160.
4. Li, J., C. Daniel, and D. Wood, *Materials processing for lithium-ion batteries*. *Journal of Power Sources*, 2011. 196(5): p. 2452-2460.
5. Yoshio, M., R.J. Brodd, and A. Kozawa, *Lithium-Ion Batteries*. Vol. 1. 2009: Springer.
6. Wood, D.L., J. Li, and C. Daniel, *Prospects for reducing the processing cost of lithium ion batteries*. *Journal of Power Sources*, 2015. 275: p. 234-242.
7. Sheng, Y., et al., *Effect of Calendering on Electrode Wettability in Lithium-Ion Batteries*. *Frontiers in Energy Research*, 2014. 2: p. 56.
8. Liu, G., et al., *Particles and polymer binder interaction: a controlling factor in lithium-ion electrode performance*. *Journal of The Electrochemical Society*, 2012. 159(3): p. A214-A221.
9. Li, J., et al., *Optimization of LiFePO₄ nanoparticle suspensions with polyethyleneimine for aqueous processing*. *Langmuir*, 2012. 28(8): p. 3783-3790.
10. Li, J., et al., *Lithium Ion Cell Performance Enhancement Using Aqueous LiFePO₄ Cathode Dispersions and Polyethyleneimine Dispersant*. *Journal of The Electrochemical Society*, 2013. 160(2): p. A201-A206.
11. Bauer, W. and D. Nötzel, *Rheological properties and stability of NMP based cathode slurries for lithium ion batteries*. *Ceramics International*, 2014. 40(3): p. 4591-4598.
12. Li, C.-C. and Y.-W. Wang, *Importance of binder compositions to the dispersion and electrochemical properties of water-based LiCoO₂ cathodes*. *Journal of Power Sources*, 2013. 227: p. 204-210.
13. Wenzel, V., H. Nirschl, and D. Nötzel, *Challenges in Lithium-Ion-Battery Slurry Preparation and Potential of Modifying Electrode Structures by Different Mixing Processes*. *Energy Technology*, 2015. 3(7): p. 692-698.
14. Dominko, R., et al., *Influence of carbon black distribution on performance of oxide cathodes for Li ion batteries*. *Electrochimica Acta*, 2003. 48(24): p. 3709-3716.

15. Qi, W., et al., *Synergetic effect of conductive additives on the performance of high power lithium ion batteries*. New Carbon Materials, 2012. **27**(6): p. 427-432.
16. Marinho, B., et al., *Electrical conductivity of compacts of graphene, multi-wall carbon nanotubes, carbon black, and graphite powder*. Powder Technology, 2012. **221**: p. 351-358.
17. Lee, J.-H., et al., *Strategic dispersion of carbon black and its application to ink-jet-printed lithium cobalt oxide electrodes for lithium ion batteries*. Journal of Power Sources, 2011. **196**(15): p. 6449-6455.
18. Özcan-Taşkin, N.G., G. Padron, and A. Voelkel, *Effect of particle type on the mechanisms of break up of nanoscale particle clusters*. Chemical Engineering Research and Design, 2009. **87**(4): p. 468-473.
19. Vijayaraghavan, B., et al., *An Analytical Method to Determine Tortuosity in Rechargeable Battery Electrodes*. Journal of The Electrochemical Society, 2012. **159**(5): p. A548.
20. Ebner, M., et al., *X-Ray Tomography of Porous, Transition Metal Oxide Based Lithium Ion Battery Electrodes*. Advanced Energy Materials, 2013. **3**(7): p. 845-850.
21. Buqa, H., et al., *Study of styrene butadiene rubber and sodium methyl cellulose as binder for negative electrodes in lithium-ion batteries*. Journal of Power Sources, 2006. **161**(1): p. 617-622.
22. Lee, J.-H., et al., *Effect of carboxymethyl cellulose on aqueous processing of natural graphite negative electrodes and their electrochemical performance for lithium batteries*. Journal of The Electrochemical Society, 2005. **152**(9): p. A1763-A1769.
23. Pensini, E., et al., *Carboxymethyl cellulose binding to mineral substrates: Characterization by atomic force microscopy-based Force spectroscopy and quartz-crystal microbalance with dissipation monitoring*. Journal of colloid and interface science, 2013. **402**: p. 58-67.
24. Diftis, N. and V. Kiosseoglou, *Improvement of emulsifying properties of soybean protein isolate by conjugation with carboxymethyl cellulose*. Food Chemistry, 2003. **81**(1): p. 1-6.
25. Mazouzi, D., et al., *Critical roles of binders and formulation at multiscales of silicon-based composite electrodes*. Journal of Power Sources, 2015. **280**: p. 533-549.
26. Lim, S., et al., *The effect of binders on the rheological properties and the microstructure formation of lithium-ion battery anode slurries*. Journal of Power Sources, 2015. **299**: p. 221-230.
27. Kim, S., et al., *Drying of the silica/PVA suspension: effect of suspension microstructure*. Langmuir, 2009. **25**(11): p. 6155-6161.
28. Cerbelaud, M., et al., *Brownian Dynamics Simulations of Colloidal Suspensions Containing Polymers as Precursors of Composite Electrodes for Lithium Batteries*. Langmuir, 2012. **28**(29): p. 10713-10724.
29. Zang, Y.-H., et al., *The migration of styrene butadiene latex during the drying of coating*

- suspensions: when and how does migration of colloidal particles occur?* Langmuir, 2010. **26**(23): p. 18331-18339.
30. Aligizaki, K.K., *Pore structure of cement-based materials: testing, interpretation and requirements*. 2005: CRC Press.
 31. Kaufmann, J., R. Loser, and A. Leemann, *Analysis of cement-bonded materials by multi-cycle mercury intrusion and nitrogen sorption*. Journal of colloid and interface science, 2009. **336**(2): p. 730-737.
 32. Lestriez, B., et al., *On the binding mechanism of CMC in Si negative electrodes for Li-ion batteries*. Electrochemistry Communications, 2007. **9**(12): p. 2801-2806.

CHAPTER 5 Effect of electrolyte solution on the electrolyte wetting

5.1 Introduction

The importance of electrolyte wetting on the battery performance has been widely recognized. [1, 2] The complexity itself [3] [4] [5], however, is not well addressed [6]. After the electrolyte injection, the wetting process happens with the extension of solution front, until the equilibrium status is achieved. The capillary force is the underlying driving force. On the way of electrolyte filling all the pores, the porous electrodes/separator media are in an unsaturated condition [7]. This process is described as the capillary flow[7, 8], where the pressure deficit is directly connected with the surface tension and curvature existing on solution front (or the liquid-gas interfaces) within the electrodes medium[9]. Compared with flow with a saturation condition in porous media which can be resolved with Darcy's law[10] or Navier-Stokes equation[11] in macroscopic, the flow in the unsaturated situation still has more complexity to deal with.

In general, the properties of both electrolyte and electrode microstructure will determine the electrolyte wetting in the electrode film. The effects of electrode microstructure have been explored in the previous chapters. [12] Given the effects of electrolyte, the performance of wetting is usually considered to be determined by its surface tension and viscosity[13]. In order to improve battery performance, especially, functional designed for electrolyte composition is required, which will further affect its surface tension and viscosity[14]. Wetting agent is added when the electrolyte cannot sufficiently wet the non-polar polymer separator sheet[15]. Higher reversible capacity (354 mAh g⁻¹ versus 347 mAh g⁻¹) and coulombic efficiency (91% versus 84%) in the first cycle is achieved by adding 2–5% cyclohexane wetting agent into the electrolyte system with 1M LiPF₆ and EC/DEC (1:2).[16] The improvement in performance is attributed to the improved wettability

of electrolyte to the separator and electrodes.

There is very little research about the effect the electrolyte. Based on capillary flow model, Wu et al. investigated the wetting behavior of lithium cobalt oxide (LiCoO_2) and mesocarbon microbead (MCMB) electrodes in different liquid electrolytes [9]. Stefan et al. [10] investigated the wetting of separator sheets (Celgard, Separion) and electrodes (LiCoO_2 , $\text{Li}_4\text{Ti}_5\text{O}_{12}$, graphite) by ionic liquids, and Dahbi et al. [11] reported on interfacial properties of graphite electrodes and Celgard separators by liquid electrolytes. Kuhnel et al. [12] studied wetting properties of porous electrodes in electrolytes based on organic solvents and ionic liquids. Their research proved that, according to Lucas-Washburn equation, viscosity and surface tension are two important parameters of electrolyte solutions used to characterize wetting rate of electrolyte in the electrode films. The change of salt concentration and electrolyte additives will result in the change of surface tension and viscosity, which will impact the electrolyte wetting rate.

Beside good wetting performance with battery component like: porous electrodes and separator sheet, the electrolyte solutions still have some critical roles, such as ion transport pathways, ion-pair dissociation and good Li^+ ion conductivity. Due to the excellent ion conductivity, in current electrolyte systems, EC (ethylene carbonate) coupled with a linear carbonate co-solvent DMC (dimethyl carbonate), EMC (ethylmethyl carbonate), or PC (propylene carbonate) is the most common choices [17]. In our previous research, the wetting rate of baseline electrolyte (3:7 (volumetric ratio) EC/ EMC-1.2M LiPF_6) has been measured by wetting balance test. The graphite anode and NMC333 cathode were used as baseline anode and cathode. Therefore, beside the tests for each solution: DMC, EMC, and PC, blends of 3:7 (vol%) EC/EMC will also be tested. To

explore the effect of these solutions on wetting rate will be explored. The surface tension will be measured using the Wilhelm plate method [18], and the viscosity will be measured by tuning-fork viscometer. Moreover, EA (Ethyl Acetate), an electrolyte additive for application in higher usage voltage [19], will also be used to explore the application of wetting balance method in developing novel electrolyte.

5.2 Experiment

The materials used in the research are provided by courtesy of Johnson Controls, Inc. PC, EMC, DMC, EA and LiPF_6 (all these chemicals come from BASF) are used as received. EC was melted at 80°C for 1 hour at glove box chamber with heating capability before mixing. The resulted EC solution was added into the EMC solution at room temperature in the same glove box. The 3:7 (volumetric ratio) solution of EC: EMC with 1.2M LiPF_6 was also mixed accordingly in similar procedure. The wetting rate is measured by wetting balance test under flowing high purity argon. More detail about the test can be found in previous chapters. The surface tension was measured using same wetting balance according to the Wilhelmy plate method (A roughened platinum iridium alloy was used). And the viscosity will be measured by tuning-fork viscometer (A&D SV-10A).

5.3 Measurement of surface tension

According to the Wilhelmy plate method, the plate was hung under the microbalance, the solution in the beaker was lift to touch the plate. Then, the force vertically acting on the plate by the liquid meniscus is measured by the microbalance. The maximum force was achieved after meniscus

stable formed on the plate surface. The weight of the liquid meniscus uplifted over the horizontal surface is equal to the force applied to the plate. By measuring maximum increased weight, the surface tension can be calculated by using Eq. 5-1. Contact angle of the roughened platinum iridium alloy with solution was considered zero. A typical curve from wilhelmy plate is shown in the Figure 5-1. To achieve the accuracy of test, the maximum weight is stabilized for a certain time in the test.

$$\gamma_{lv} = \frac{Force}{Perimeter \cdot \cos \theta} = \frac{(Maximum\ weight) \cdot 9.8 \cdot 1000}{(0.17 + 23.9) \cdot 2} \quad (5-1)$$

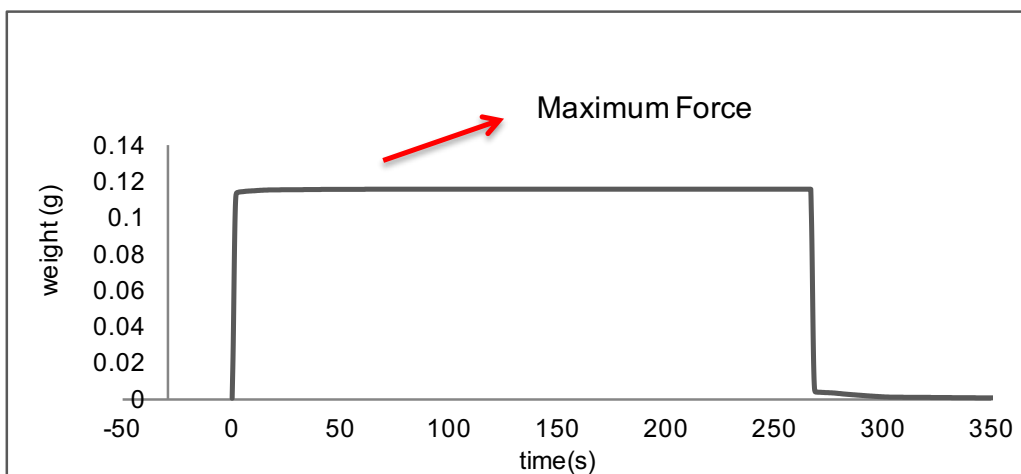


Figure 5-1 A typical curve for surface tension test.

5.4 Results and discussion

Each solution was tested 15 times on the graphite anode and NMC cathode to account for experimental and electrode film variations. The wetting rates for all the tests are summarized in Table 5-1. Error% in the table is defined as standard deviation divided by average wetting rate, which is also similar to coefficient of variation, was used to describe measurement stability. The Error% in this test is in the range of 3.4% to 7%, which indicate good stability. The results of viscosity and surface tension are also summarized in Table 5-1. The wetting rate equation in 2-1b (in chapter 2) can be simplified (seen as equation 5-2) when the electrode films were kept same for all tests.

Table 5-1 Summary of wetting rate, viscosity and surface tension data for all the solutions.

	Average wetting rate	Stdev	Error (%)	Samples	viscosity	surface tension	$(\gamma/2\eta)^{0.5}$
Anode	mm/S ^{0.5}				(mPa S)	(mN/m)	
PC	0.462	0.0156	3.4	15	2.53	41.1	2.85
EMC	0.640	0.0317	5.0	15	0.65	27.2	4.57
DMC	0.682	0.0302	4.4	15	0.59	29.1	4.97
3-7 EC-EMC	0.324	0.0137	4.2	15	1.52	31.2	3.21
3-7 EC-EMC 1.2MLiPF6	0.244	0.0171	7.0	15	4.62	32.2	1.87
Cathode							
PC	0.285	0.0303	10.6	15	2.53	41.1	2.85
EMC	0.472	0.1100	23.3	15	0.65	27.2	4.57
DMC	0.469	0.0552	11.8	15	0.59	29.1	4.97
3-7 EC-EMC	0.241	0.0122	5.1	15	1.52	31.2	3.21
3-7 EC-EMC 1.2MLiPF6	0.175	0.0136	7.8	15	4.62	32.2	1.87

$$K = P \sqrt{\frac{\bar{r}_{eff} \gamma_{lv} \cos \theta}{2\eta}} \quad (2-1b)$$

$$K = C \sqrt{\cos \theta} \sqrt{\frac{\gamma_{lv}}{2\eta}} \quad (5-2)$$

K : wetting rate of electrolyte in porous electrode, P : electrode porosity, \bar{r}_{eff} : effective pore radius of electrode, γ_{lv} : surface tension of electrolyte solution, $\cos \theta$: contact angle of electrolyte with electrode, η : viscosity of electrolyte solution, C : constant for same electrode.

The contact angle is affected by both the surface tension of liquid and surface energy of the solid according to the Young's equation. The variation will depend on the surface tension if same solids are used. Generally, the electrolyte solution is wettable with electrode films between which the contact angle is considered to be less than 30 degrees. Moreover, the contact angle measurement for porous electrode film is still challenging. Due to the dependable change with surface tension and not practical available of the contact angle, in Equation 5-2, only the effect of $\sqrt{\frac{\gamma_{lv}}{2\eta}}$ will be taken into account. The value of $\sqrt{\frac{\gamma_{lv}}{2\eta}}$ for each solution is also summarized in Table 5-1.

Considering the combined effect of surface tension and viscosity, the change of wetting rate of these solutions are indicated in the Figure 5-2. For both electrodes, the wetting rate increase linearly with the increase of $\sqrt{\frac{\gamma_{lv}}{2\eta}}$ of the solution. The curve fitting parameter R^2 is 0.875 for anode and 0.929 for cathode, which confirm the reliable linear relation in these solutions. DMC has the fastest wetting rate and the electrolyte with lithium salt has lowest wetting rate. The total trend for

the wetting rate of these solutions is: DMC > EMC > PC > 3:7 EC/EMC > 3:7 EC/EMC, 1.2M LiPF₆. Compared with the drastically increase in viscosity from 0.65 to 4.62 mPa.S, from EMC to EC/EMC blends and to relative electrolyte with salt, the surface tension did not increase a lot, which is only slight increased from 27.2 to 32.2 mN/m. The lithium salt could form a structural complex with the solvent, which results in the larger amount increase in the viscosity. Since EC is highly polarity, adding EC to EMC has more influence on increasing surface tension (+4mN/m) than adding lithium salt to EC/EMC blends (+1mN/m). The increase in surface tension should increase the wetting rate. However, the viscosity EC is also improved by adding EC, which will decrease the wetting rate. As a result, the finally wetting rate is reduced from 0.640 mm/s^{0.5} of EMC to 0.324 mm/s^{0.5} of EC/EMC 3:7 blends. Therefore, the effects of solution on the wetting rate can be analyzed through combined influence of surface tension and viscosity ($\sqrt{\frac{\gamma_{lv}}{2\eta}}$). The linear increase trend of the wetting rate can also be observed by adding to PC to an ionic liquid solution (PYR₁₄TFSI) in LiFePO₄ cathode [21]. As shown in the Figure 5-3, where the data is from literature; the wetting rate is increasing linearly with $\sqrt{\frac{\gamma_{lv}}{2\eta}}$ for different PC content, where the curve fitting parameter R^2 is 0.911.

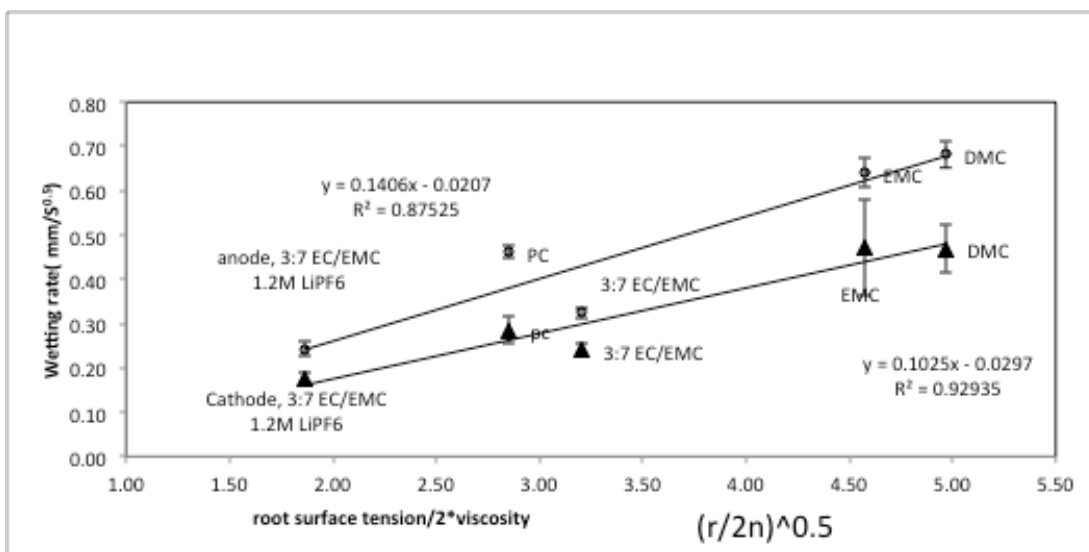


Figure 5-2 Wetting rate change with root surface tension divided by viscosity for different solutions.

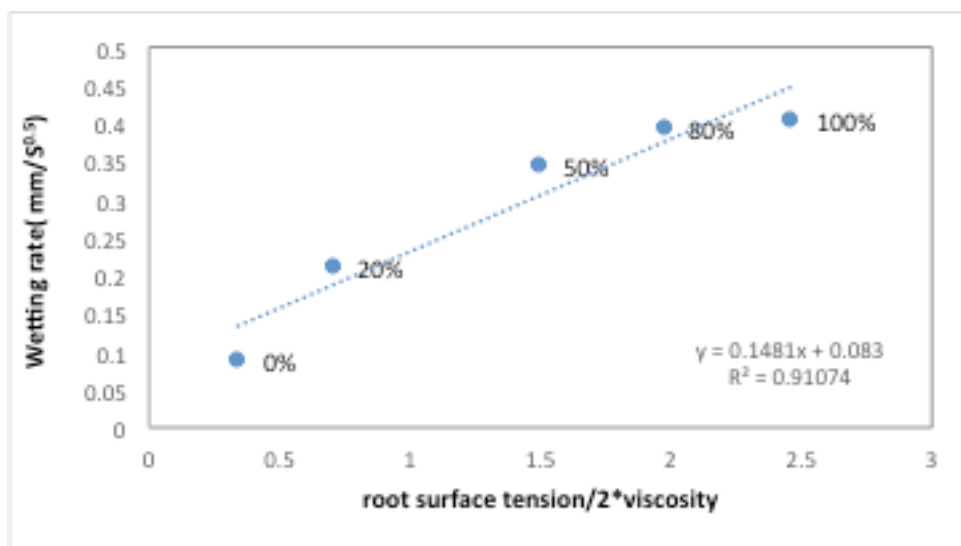


Figure 5-3 wetting rate changes with increasing PC contents in ionic liquid electrolyte in LiFePO₄ cathode, data from literature [21]

5.5 Effect of EA additive on the wetting rate

Table 5-2 Summary of wetting rate, viscosity and surface tension data for different EA addition.

	Average wetting rate	Stdev	Error (%)	Samples	viscosity	surface tension	$(\gamma/2\eta)^{0.5}$
Anode	mm/s ^{0.5}				(mPa S)	(mN/m)	
No additive	0.244	0.0171	7.0	8	4.62	32.16	1.87
0.1%	0.226	0.0119	5.3	8	4.67	32.21	1.89
0.5%	0.190	0.0161	8.5	8	4.52	32.67	1.90
1.0%	0.239	0.0112	4.7	8	4.43	32.82	1.92
2.0%	0.232	0.0139	6.0	8	4.28	33.14	1.97
Cathode							
No additive	0.175	0.0136	7.8	8	4.62	32.16	1.87
0.1%	0.175	0.0178	10.2	8	4.67	33.22	1.89
0.5%	0.143	0.0111	7.7	8	4.52	32.67	1.90
1.0%	0.171	0.0207	12.1	8	4.43	32.82	1.92
2.0%	0.206	0.0376	18.2	8	4.28	33.14	1.97

EA is a linear carboxylates with high permittivity and low viscosity, 0.426 *mPa.S* at 25°C [20]. To investigate the effect of EA addition, amount of 0.1%, 0.5%, 1% and 2% are added to the baseline electrolyte (3:7 EC/EMC, 1.2 M LiPF₆). The wetting rates, viscosity and surface tension for electrolytes with different EA addition were summarized in Table 5-2. The trends of wetting rate change are also depicted in the Figure 5-4. Although it only different slightly, the averaged wetting rate of these electrolytes are still distinctive. In both anode and cathode, the wetting rate is slightly decreased by adding 0.1%EA, and further decreased to lowest at 0.190 *mm/s*^{0.5} for anode and 0.143 *mm/s*^{0.5} for cathode at 0.5%EA. The wetting rate will rebound back to around 0.23 *mm/s*^{0.5} for anode and 0.17 *mm/s*^{0.5} for cathode for 1% and 2% EA. However, as shown in the Figure 5-5, from

0.1%EA to 0.5%EA, the surface tension is slightly increased from 32.21 to 32.67 mN/m , which do not indicate a decrease in wetting rate, and the viscosity is decreased from 4.67 to 4.52 $mPa.S$, which also do not indicate a decrease in wetting rate. Therefore, it is abnormal for the decrease of wetting rate at 0.5%EA. Since the values of surface tension are very close for all the solution, it may be beyond the accuracy of Wilhelm plate method used in this research, which was operated manually. To uncover the underlying reason, it is necessary to measure the surface tension with more accuracy.

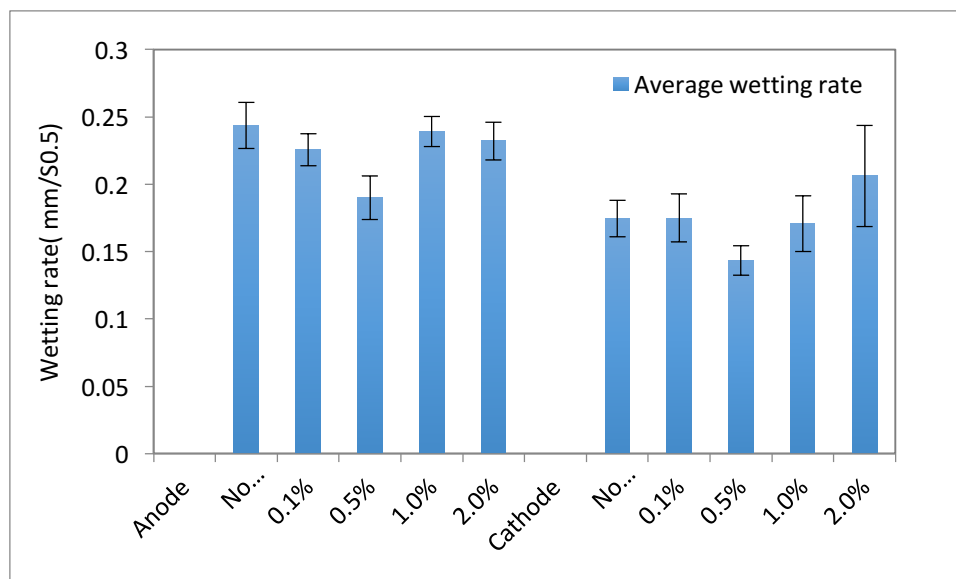


Figure 5-4 Wetting rate for different EA addition at anode and cathode.

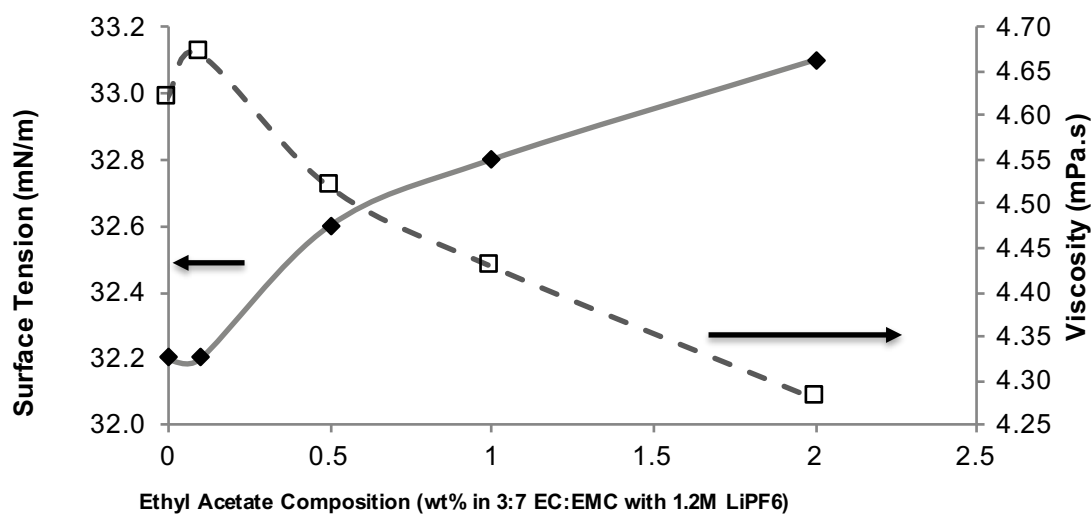


Figure 5-5 Surface tension and viscosity change with different amount of Ethyl Acetate

A further analysis of the relation between $\sqrt{\frac{\gamma_{lv}}{2\eta}}$ and wetting rate is given in the Figure 5-6, no linear

trends can be found. This is very different to the trend of linear increase of wetting rate $\sqrt{\frac{\gamma_{lv}}{2\eta}}$, which are revealed in the Figure 5-2, and 5-3. Beside the abnormal decrease of wetting rate at 0.5%EA, the wetting rates for other electrolyte is in a very narrow range. More over, the value of $\sqrt{\frac{\gamma_{lv}}{2\eta}}$ is also only different from 1.87 to 1.97. As indicated in the Figure 5-2, and 5-3, the value of $\sqrt{\frac{\gamma_{lv}}{2\eta}}$ is in the range from 1.97 to 4.97 for Figure 5-2 and from 0.34 to 2.46 for Figure 5-3. Therefore, it is possible that the linear increase of the wetting rate only hold for some solutions with wide range of $\sqrt{\frac{\gamma_{lv}}{2\eta}}$.

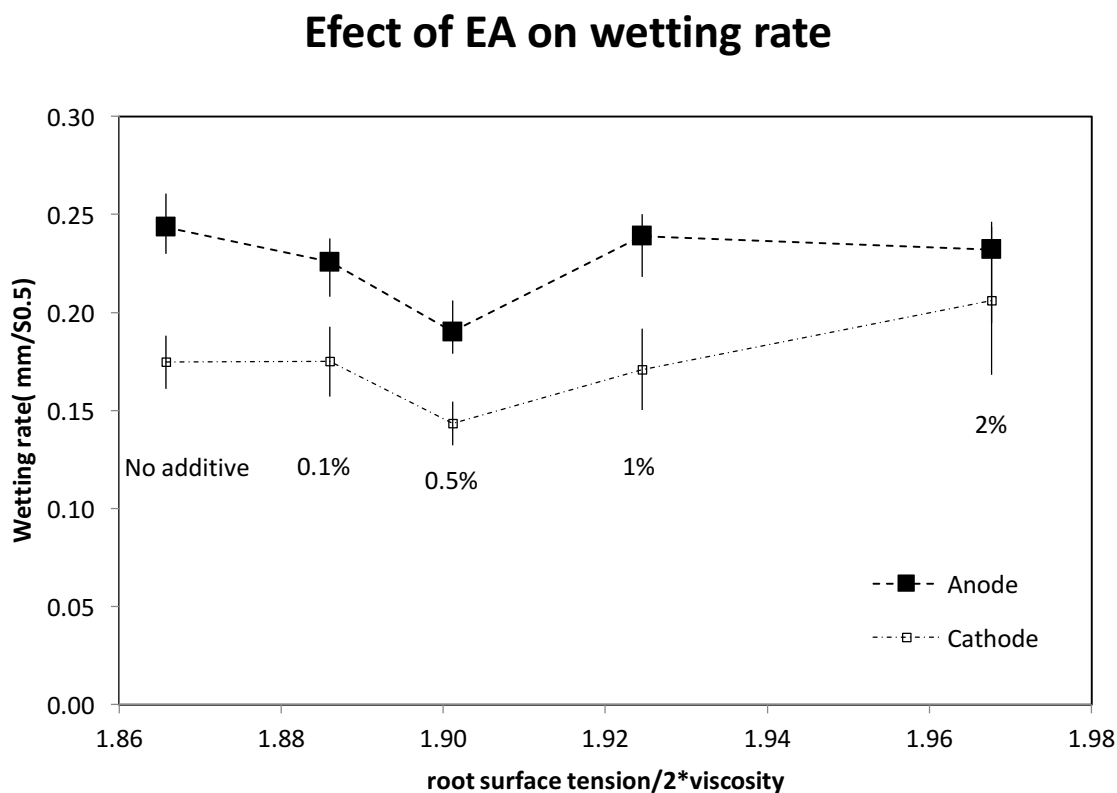


Figure 5-6 Wetting rate change with root surface tension divided by viscosity for different EA addition

5.6 Conclusion

Based on standard baseline anode (graphite) and cathode (NMC333), in this research, the wetting balance method was also used to measure the wetting rates for various solutions from DMC, EMC, PC, and blends of 3:7 EC/EMC and electrolyte 3:7 EC/EMC, 1.2M LiPF₆. Although the effect of contact angle is neglected in this research, the linear increment relation of $\sqrt{\frac{\gamma_{lv}}{2\eta}}$ and wetting rate by Washburn equation is still confirmed. For solutions, which have good wettability with the porous medium, the contact angle doesn't play a critical role on the wetting rate. Moreover, the combined influence of surface tension and viscosity of the solution is more feasible for analyzing its effect on the wetting rate.

To explore the application of wetting balance method in developing novel electrolyte, the wetting rates for EA, an electrolyte additive for higher voltage application, were also measured and investigated. The EA is added to the electrolyte (3:7 EC/EMC, 1.2M LiPF₆) with weight amount from 0.1%, 0.5%, 1% and 2%. The averaged wetting rates for these electrolytes are distinctive, although their value only different slightly. The usage of wetting balance method in developing novel electrolyte with EA additive is applicable. However, the linear increment trend of wetting rate with $\sqrt{\frac{\gamma_{lv}}{2\eta}}$ doesn't hold. It is possible due to the narrower range (1.87 to 1.97) of $\sqrt{\frac{\gamma_{lv}}{2\eta}}$ by adding EA, compared with the wide range (1.97 to 4.97) of $\sqrt{\frac{\gamma_{lv}}{2\eta}}$ for various solutions.

References

1. Pfleging, W. and J. Pröll, *A new approach for rapid electrolyte wetting in tape cast electrodes for lithium-ion batteries*. Journal of Materials Chemistry A, 2014. **2**(36): p. 14918.
2. Wood, D.L., J. Li, and C. Daniel, *Prospects for reducing the processing cost of lithium ion batteries*. Journal of Power Sources, 2015. **275**: p. 234-242.
3. Ibagon, I., M. Bier, and S. Dietrich, *Order of wetting transitions in electrolyte solutions*. J Chem Phys, 2014. **140**(17): p. 174713.
4. De Gennes, P.-G., Françoise Brochard-Wyart, and David Quéré. , *Capillarity and wetting phenomena: drops, bubbles, pearls, waves*. 2013: Springer Science & Business Media.
5. Quéré, D., *Wetting and Roughness*. Annual Review of Materials Research, 2008. **38**(1): p. 71-99.
6. Jannesari, H., M.D. Emami, and C. Ziegler, *Effect of electrolyte transport properties and variations in the morphological parameters on the variation of side reaction rate across the anode electrode and the aging of lithium ion batteries*. Journal of Power Sources, 2011. **196**(22): p. 9654-9664.
7. Miller, E. and R. Miller, *Physical theory for capillary flow phenomena*. Journal of Applied Physics, 1956. **27**(4): p. 324-332.
8. Waghmare, P.R. and S.K. Mitra, *Modeling of combined electroosmotic and capillary flow in microchannels*. Anal Chim Acta, 2010. **663**(2): p. 117-26.
9. Xiong, Y., *Flow of water in porous media with saturation overshoot: A review*. Journal of Hydrology, 2014. **510**: p. 353-362.
10. Bear, J., *Dynamics of fluids in porous media*. 2013: Courier Corporation.
11. Allaire, G., et al., *Ion transport in porous media: derivation of the macroscopic equations using upscaling and properties of the effective coefficients*. Computational Geosciences, 2013. **17**(3): p. 479-495.
12. Sheng, Y., et al., *Effect of Calendering on Electrode Wettability in Lithium-Ion Batteries*. Frontiers in Energy Research, 2014. **2**: p. 56.
13. Wu, M.-S., et al., *Assessment of the wettability of porous electrodes for lithium-ion batteries*. Journal of applied electrochemistry, 2004. **34**(8): p. 797-805.
14. Zhang, S.S., *A review on electrolyte additives for lithium-ion batteries*. Journal of Power Sources, 2006. **162**(2): p. 1379-1394.
15. Zhang, S.S., *A review on the separators of liquid electrolyte Li-ion batteries*. Journal of Power Sources, 2007. **164**(1): p. 351-364.
16. Wang, X., et al., *New Additives to Improve the First-Cycle Charge–Discharge Performance of a Graphite Anode for Lithium-Ion Cells*. Journal of The Electrochemical Society, 2005. **152**(10): p. A1996-A2001.

17. Xu, K., *Nonaqueous liquid electrolytes for lithium-based rechargeable batteries*. Chemical reviews, 2004. **104**(10): p. 4303-4418.
18. Yuan, Y. and T.R. Lee, *Contact angle and wetting properties*, in *Surface science techniques*. 2013, Springer. p. 3-34.
19. Hallac, P.B., J. Jiang, and C.R. Fell, *Electrolyte Formulation for High Voltage and Wide Temperature Lithium-Ion Cells*. 2013, US Patent App. 13/910,686.
20. Riddick, J.A., W.B. Bunger, and T.K. Sakano, *Organic solvents: physical properties and methods of purification*. 1986.
21. Kühnel, Ruben-Simon, et al. (2013). Evaluation of the wetting time of porous electrodes in electrolytic solutions containing ionic liquid. *Journal of Applied Electrochemistry*, 43(7), 697-704.

CHAPTER 6 Summary

In lithium ion batteries, investigation about manufacturing process is as important as the development of material. The manufacturing process will construct the complicated porous microstructure of electrode, which is one of the challenges to understand the operation mechanism of lithium ion batteries, especially when the size is scaled up from coin cell in lab, to pouch cell in industry. After inserting the assembly of anode/separator/cathode into the can/case, electrolyte is injected. After injection, the battery can/case is sealed for later formation and charging process which will produce an activated battery cell. Electrolyte filled in the pores plays the role of ionic conductive path for lithium ions between anode and cathode. However, the process of electrolyte transporting to fill the pores in the electrode after injection is less noticed in academic. In coin cell, only 2-3 drops of electrolyte are needed. In industry, the importance of electrolyte transport is well known and it is considered as part of electrolyte wetting (or initial wetting in some situations). In consideration of practical usage term, electrolyte wetting is adopted to use for electrolyte transporting process. The goal of this dissertation is to build in-depth understanding of electrolyte wetting in electrode films by investigating the effects of electrolyte solution and pore structure, based on quantitative measurement.

The wetting balance method is introduced to quantitative analysis electrolyte wetting. A reliable characterization of electrolyte wetting is developed based on the wetting rate, the speed of electrolyte transport inside the porous electrode films. To account for the unavoidable variables of electrode film, statistic measurement of a batch of samples is necessary for clarifying the underlying mechanism of the electrolyte wetting.

6.1 Establish electrolyte wetting test for anode and cathode electrode films

The electrolyte wetting process in lithium-ion battery anode and cathode electrode films were characterized using the wetting balance method. Based on 15 tests each, the baseline electrolyte (30wt%EC/70wt% EMC-1.2M LiPF₆) was found to transport faster in graphite anodes than NMC333 cathodes, with average wetting rates of 0.244 mm/s^{0.5} (+/- 6.79%) and 0.175 mm/s^{0.5} (+/- 8.00%) respectively. All the electrode films are prepared in the pilot production line in which material loading variations is within 3%. Therefore, the established electrolyte wetting test method is feasible to find out small wetting rate difference between samples.

The baseline electrolyte has been widely used in lithium ion battery. The effects of the electrolyte are neglected since it is considered wetting well with both graphite anode and NMC cathodes. Therefore, only different microstructures of electrode films are needed to uncover the differences in electrolyte wetting rate. MIP (Mercury intrusion porosimetry) tests is used to investigate electrode micro pore structure. The result showed the anode films had higher overall porosity and larger pore sizes relative to the cathode films. The MIP tests also showed that both films had a major connected pore network of a similar size range of roughly 0.8 to 1.3 μm although this network was slightly larger and accounted for a much higher percentage of total porosity for the anode film relative to the cathode film. SEM and MIP results showed that the cathode had both inter- and intra-particle porosity with the intra-particle pores accounting for a significant fraction (24.8%) of the total porosity while the anode film did not have this small-scale intra-particle pore structure. The higher overall porosity, larger pore size, and higher volume percentage of large connected pores likely account for the faster wetting of the anode films relative to the cathode films.

A simplified expression of the effective pore radius (\bar{r}_{eff}) in the Lucas-Washburn equation does not have a practical basis when the porous structure is complicated as is the case with electrode films. Based on the combined results from MIP and SEM characterization, the electrode microstructure is composed of connected pore networks in which pore cavities are connected by pore throats of restricted size relative to the larger pore cavities. This pore-network model is different from other electrode microstructure models based on properties like pore size distribution and morphology. MIP testing was shown to provide additional information related to wetting performance beyond the parameters of porosity and average pore size that have been used by other researchers. These findings are helpful for clarifying electrolyte wetting in the porous electrode films and show the additional insight that can be gained from relating wetting balance tests to MIP and SEM characterization methods.

6.2 Electrolyte wetting of graphite anode with pore structure modified by calendaring

The wettability of graphite anode films as a function of the calendaring process was investigated and related to the development of the pore structure in the electrode films. Modest calendaring was shown to improve the wetting rate of anode films due to the alignment of particles and the increase in divergence within the pore networks. Calendaring beyond an ideal level decreased wetting rates due to reductions in porosity and average pore diameter. A combination of convergence-divergence flow and capillary flow mechanisms determine the wetting rate of the film. Convergence-divergence dominates in the as-coated and lightly calendared conditions while capillary flow dominates at higher levels of calendaring. Wetting rates generally follow the Washburn predictions as a function of pore size and porosity levels though deviations from ideal

behavior were observed that indicate that the effective pore diameter used in that equation may be inadequate in describing the pore network of the electrode film.

6.3 Electrolyte wetting of anode electrode with different pore structures controlled by changing binder/carbon black ratio

Effects of post-production method, calendering, on the electrolyte wetting has been demonstrated. The evolution of pore structure during the calendering process could be used to modify the electrolyte wetting rate. In fact, the pore structure of electrode film is initially determined by the composition of its components, like active material, binder, conductive additive, and slurry solvent.

In this research, wetting rate change with pore structure evolution in the electrode film production stage is demonstrated with varying the amount of conductive additive (the carbon black). The effect of different amount of carbon black on electrolyte wetting of graphite anode electrode is found decreasing from 3%CB ($0.109 \text{ mm/s}^{0.5}$) to 5%CB ($0.075 \text{ mm/s}^{0.5}$), and bouncing back at 7%CB ($0.127 \text{ mm/s}^{0.5}$). The mechanism of combined capillary and converging-diverging flow is applied to analysis the trends of wetting rate. Based on the MIP and SEM analysis, the pore structure is highly affected by increasing the loading of carbon black. The pore cavity and pore sub-network are increasing with the higher loading of carbon black, as revealed by MIP curve. Based on the SEM image, the void is becoming more filled with carbon black domain, which is agglomerate of small carbon black aggregates. The pore structure of different electrodes with increasing filling of carbon black in the void is evolved from micro crack (5%CB) in the interface and second pore (7%CB) in the carbon black domains. The micro-crack is mainly contributing to the pore cavity increase in 5%CB, while the second pore in 7%CB help the increase of pore sub-

network to 11.2%. The pore cavity increase in 5%CB results in higher converging of electrolyte, which decrease the wetting rate. Although the pore cavity amount is also increased in 7%CB, the diverging effect of the increased pore sub-network helps further increase the wetting rate.

The mechanism of combined flow of electrolyte wetting, which discovered in the research of calendering effect, is verified in this research. Understanding the cause of electrolyte wetting is fundamental to many other phenomena in the lithium ion battery. The effect of carbon black on the pore structure would be helpful for understanding some non-uniformity in the electrode film.

6.4 Effect of electrolyte solutions on the electrolyte wetting

Based on standard baseline anode (graphite) and cathode (NMC333), in this research, the wetting balance method was also used to measure the wetting rates for various solutions from DMC, EMC, PC, and blends of 3:7 EC/EMC and electrolyte 3:7 EC/EMC, 1.2M LiPF₆. Although the effect of contact angle is neglected in this research, the linear increment relation of $\sqrt{\frac{\gamma_{lv}}{2\eta}}$ and wetting rate by Washburn equation is still confirmed. For solutions, which have good wettability with the porous medium, the contact angle doesn't play a critical role on the wetting rate. Moreover, the combined influence of surface tension and viscosity of the solution is more feasible for analyzing its effect on the wetting rate.

To explore the application of wetting balance method in developing novel electrolyte, the wetting rates for EA, an electrolyte additive for higher voltage application, were also measured and investigated. The EA is added to the electrolyte (3:7 EC/EMC, 1.2M LiPF₆) with weight amount from 0.1%, 0.5%, 1% and 2%. The averaged wetting rates for these electrolytes are distinctive, although their value only different slightly. The usage of wetting balance method in developing

novel electrolyte with EA additive is applicable. However, the linear increment trend of wetting rate with $\sqrt{\frac{\gamma_{lv}}{2\eta}}$ doesn't hold. It is possible due to the narrower range (1.87 to 1.97) of $\sqrt{\frac{\gamma_{lv}}{2\eta}}$ by adding EA, compared with the wide range (1.97 to 4.97) of $\sqrt{\frac{\gamma_{lv}}{2\eta}}$ for various solutions.

6.5 Novelty of the research

1. Investigation of electrolyte wetting is feasible with applied wetting balance method. The wetting rate with statistic distribution can be used to compare the wetting performances for different electrolyte and electrode films.
2. Pore structures of graphite anode and NMC333 cathode are analyzed with MIP and cross section BSE-SEM. Based on these results, the pore network model, composed by cavity and pore throat is adopted to investigate the mechanism of electrolyte wetting. A mechanism of flow with combined capillary and converging-diverging effect is revealed in the electrolyte wetting of electrodes.
3. According to the test results, the wetting rate of the graphite anode is increased with slightly calendering, and then it is sharply decreased with further pressing. The underlying mechanism of wetting rate change is investigated and revealed by pore structure evolution with calendering process, based on the theory of pore networks.
4. The wetting rate change with pore structure evolution in the electrode film production stage is demonstrated with varying the amount of conductive additive (the carbon black). It is confirmed from SEM image that the pore structure of different electrodes with increasing filling of carbon black in the void is evolved from micro crack (5%CB) in the interface and second pore (7%CB) in the carbon black domains.

6.6 Future works

The characterization of wetting rate of electrolyte in the porous electrodes has been established by using wetting balance test method. Based on the quantitative wetting rate data, in the future investigation, both in-depth understanding of wetting mechanism for different electrode films and application of wetting balance measurement in manufacturing for lithium ion batteries are feasible. Besides the opportunities, there are still some challenges to overcome to achieve those goals. Foundation on these, in the following passages, the two directions will be covered to discuss the opportunities and challenges for future works.

Further in-depth research about understanding the mechanism of electrolyte wetting.

The research about the mechanism of electrolyte wetting has been only demonstrated with anode electrode, which is consisted by a major pore network. In contrast, most cathode materials, for example NMC serious cathodes, are an assemble of agglomerate particles which are composed by nanoscale primary particle. As a result, there are two major pore networks in the cathode electrode. The converging-diverging effect will become more complicated due to the interaction between two pore networks. Changing the pore network ratio by calendaring the electrode film to different porosity, the effect of two major pore networks in the cathode could be investigated. As a result, the effect of the agglomerate particle size on the electrolyte wetting could be discussed.

To further in-depth investigation of electrolyte wetting behavior, a detailed understanding of the pore structure, especially in 3 dimensional for represent real structure, in the electrode film is necessary. Although MIP can be applied to reveal the pore network as a convenient method, detailed and localized information about pore shape and how pores are connected are not available. As a result, an accurate view of how the electrolyte transport inside porous electrode, especially

from pore cavities into the pore throats, is hard to achieve. To overcome these obstacles, the 3D imaging techniques, such as FIB (focus ion beam)-SEM, NMR and MRI, can be used to reveal the real pore structure. It can also be supplemental to the drawback of MIP analysis, which gives only analogical pore data. In other words, the limits of these 3D imaging techniques, which are time consuming and very limited sample area, can be compensated by MIP analysis in couple centimeter length sample size. With the help of facile and real pore structure analysis, it is possible to predict electrolyte wetting rate performance and electrolyte distribution across the whole battery. And a lot of other properties of lithium ion batteries, including ion transport, thermal performance etc. can also benefit from the in-depth research of pore structure.

The application of wetting rate data in the manufacturing for lithium ion battery.

Due to the lack of quantitative measurement method for electrolyte wetting, the effects of electrolyte wetting haven't been widely investigated. However, it has direct impact on the electrochemical performance of lithium ion batteries, for example, cycle and rate performance, calendar life, active material utilization etc. It is very beneficial to explore the correlation of wetting rate to these electrochemical data. Moreover, the wetting rate is affected by both production process and post production process. The relation of electrolyte wetting with batteries' performance could be used to find better manufacturing parameters. By comparing wetting rate with electrochemical performance, as a result, there are a lot of opportunities to better producing lithium ion batteries.

Another important application for wetting rate measurement is its impact on improvement to formation and aging processes, which are the current bottleneck for production efficient. As discussed chapter 1, the split formation process is necessary for achieving higher energy density

and calendar and cycle life with reduced battery producing time. In this process, to ensure good electrolyte wetting, a wait period of about 24 hours is conducted after the initial electrolyte injection. Then, the cell is initially charged to low state of charge (SOC) range, at rate of $C/100$ - $C/2$. After the charge is applied, the cell is stored at predetermined temperature for about one day. During or after storage, a degassing procedure may be carried out to provide a uniform distance between the electrodes. After completing the storage period, the cell is charged to high or full SOC. The cell is stabilized for another predetermined period of time, about one to seven days at room temperature. When the wetting rate is introduced to the characterize the electrolyte wetting process, it will be more accurate to determine the sufficient wetting period and the time for storage. Therefore, it is easier to optimize the formation processes for different materials and various battery designs.

CURRICULUM VITAE

Yangping Sheng

Place of birth: Dongyang, Zhejiang Province, China

Education:

B.E., Hefei University of Technology, July 2006

Major: Inorganic and Nonmetal Material Science and Engineering

M.S., Hefei University of Technology, September 2009

Major: Material Science and Engineering

Thesis Title: Growth and mechanism of ZnO nanowire arrays on flexible substrates via solution methods

Ph.D., University of Wisconsin-Milwaukee, December 2015

Major: Material Science and Engineering

Dissertation Title: Investigation of Electrolyte Wetting in Lithium Ion Batteries: Effects of Electrode Pore Structures and Solution

Research Experience:

Research Assistant - UWM Jan. 2010-present

Project: Partner with Johnson Controls, supported by DOE to research, develop and demonstrate advanced Li ion cell manufacturing processes and techniques to reduce the existing Li-ion manufacturing costs by 50%.

- Develop a wetting balance test method to quantify electrolyte injection process for various electrolyte, electrode and separate sheet to quality control manufacturing process.
- Discover inter-connected pore network in electrode films and its effects on wetting process and battery performance by applying Mercury Intrusion Porosimetry (MIP) method.
- Characterize wetting behavior for various pouch cells with wetting balance test to help refining formation and aging process, and compare wetting rate for different industry level electrolytes.
- Collaborate with industry to analysis the effects of different manufacturing processes on electrode film microstructure and determine proper parameters for best battery performance, such as various materials (anode, cathode, and separator), slurry processing (binder, carbon black), electrode film composition, and different calendering force etc.
- Synthesize nano a-SiO₂@carbon composite for advanced anode material by sol-gel deposition of SiO₂ nanoparticle on carbon particles.

Research Assistant - HFUT Sep. 2006-Oct. 2009

Project: Supported by NSF, National 863 Program (High-Tech Development Plan) of China to synthesis and characterize nanostructured materials and applications in hybrid photovoltaic and optoelectronic devices.

- Developed a facile and economic $\text{Zn}(\text{NO}_3)_2/\text{NH}_3\cdot\text{H}_2\text{O}$ solution system based synthesis method to synthesis ZnO nanostructure arrays, such as nanowire array, nanoplate array and nanoflower, on Zinc-plated flexible substrates (copper foil, polymer films etc.).
- Proved various growth mechanisms for each nanostructure in the same synthesis system. Analyzed SEM pictures and XRD patterns from different nucleation and growth stages, proposed a growth process based on controlling crystal growth unit($\text{Zn}(\text{OH})_4^{2+}$) through release of Zn^{2+} from controllable decomposing of complex ions($\text{Zn}(\text{NH}_3)_4^{2+}$).
- Discover optical properties (green emission) of various ZnO nano-arrays based on photoluminescence (PL) spectra analysis, generated by varied concentration of Zinc vacancy through controllable growth process.
- Built ZnO/P3HT hybrid solar cell preparation station and developed preparation procedures like dissolving and filtrating P3HT solution, spin coating of P3HT on ZnO nanowire arrays, coating silver grid electrode.

Skills:

- Lithium ion battery R&D: manufacturing optimization, systematic battery design, quality control, performance test, geometric structure analysis about electrode/seperator.
- Material synthesis: sophisticated understanding about crystal growth and structure design, including chemical method, solution based deposition, hydrothermal, sol-gel etc. physical method CVD, PVD, thermal evaporation.
- Material Characterization: microstructure analysis: XRD, SEM, TEM, optical properties: FTIR, PL, pore analysis: BET, MIP, thermal analysis: DSC/TGA.

Publications

- Yangping Sheng, Christopher R. Fell, Yong Kyu Son, Bernhard M. Metz, Junwei Jiang, Benjamin C. Church, “Effect of Calendaring on Electrode Wettability in Lithium Ion Batteries”. *Frontiers in Energy Research*, 2014, 2, 56.
- Yangping Sheng, Yang Jiang, “Growth and mechanism of controllable ZnO nanostructure arrays from Zn plating layer on the flexible substrates” *Journey of Nanomaterials*, 2011 (2011): 14.
- Yi Wang, Yang Jiang, Di Wu, Yangping Sheng, Lanlan Chen, Guohua Li, Jiansheng Jie, “Field effect properties of phosphorus doped CdS single-crystal nanoribbon via co-thermal-evaporation”, *Journal of Nanoscience and Nanotechnology*, 2010, 10(1), 433-439.
- Guohua Li, Yang Jiang, Yi Wang, Chun Wang, Yangping Sheng, Jiansheng Jie, Juan A. Zapien,

Wenjun Zhang; Shuit-Tong Lee, “Synthesis $\text{CdS}_x\text{Se}_{1-x}$ Nanoribbons with Uniform and Controllable Composition via Sulfurization: Optical and Electronic Properties Studies”, *The Journal of Physical Chemistry*, 2009, 113 (39), 17183–17188.

- Jiping Zhu, Wensheng Duan, Yangping Sheng “Uniform PbS hopper (skeletal) crystals grown by a solution approach”, *Journal of Crystal Growth*, 2009, 311(2), 355-357.

Presentation

- Yangping Sheng, Christopher R. Fell, Benjamin C. Church, Investigation on electrolyte transport properties in anode and cathode electrode film in lithium ion battery by wetting balance test, MS&T 2014, Oct.12-16, Pittsburgh.